

Fluorine dynamics in BaF_2 superionic conductors investigated by NMR

Vom Fachbereich Physik
der Technischen Universität Darmstadt
zur Erlangung des Grades
eines Doktors der Naturwissenschaften
(Dr. rer. nat.)
genehmigte Dissertation

von
M.Sc. Patryk Gumann
aus Skarzysko-Kamienna, Polen

Referent: Prof. Dr. Franz Fujara
Korreferent: Prof. Dr. Bernd Stühn

Tag der Einreichung: 16.10.2007
Tag der Prüfung: 17.12.2007

Darmstadt 2008
D 17

Contents

Contents	2
1 Introduction	3
2 Fast Ionic Conductors	5
2.1 Application	8
2.2 Lattice Defects in Ionic Crystals	9
2.2.1 The Formation of Lattice Defects	10
2.3 Crystal Growth	13
2.3.1 Phase Diagram	17
2.4 Solid Electrolytes with Fluorite Structure	19
2.4.1 Fluorite Structure	19
2.4.2 Transport Mechanisms	23
2.4.3 State of the Art	24
3 Essential Aspects of Solid State NMR Theory	29
3.1 The Phenomenon of Nuclear Magnetic Resonance	29
3.2 Classical Treatment of the Relaxation	30
3.3 Quantum Mechanical Treatment	32
3.3.1 The Density Matrix Representation	32
3.3.2 Coherences and Population	33
3.3.3 Essential Aspects of the Perturbation Theory	34
3.4 Nuclear Spin Hamiltonian	35
3.4.1 Zeeman Interaction	35
3.4.2 Dipole-Dipole Coupling	35
3.4.3 The Chemical Shift	37
3.4.4 Quadrupolar Coupling	38
3.5 Correlation Functions and Spectral Densities	39
3.6 Examples of Relaxation Processes	40
3.6.1 Relaxation via Dipole-Dipole Coupling	40
3.6.2 Dipole-Dipole Coupling to Quadrupolar Spin System	40

CONTENTS

4	Experimental Techniques	47
4.1	NMR-Lineshape	47
4.1.1	Signal Processing	49
4.1.2	Magic-Angle Spinning	52
4.1.3	Multiple-Pulse Sequences	56
4.2	Field-Cycling Spectroscopy	62
4.2.1	High Temperature Probe Head	64
4.3	Static Field Gradient NMR	65
4.3.1	Hahn Echo	66
4.3.2	Solid Echo	67
4.3.3	Stimulated Echo	67
5	Measurements and Analysis	71
5.1	Diffusion Measurements	71
5.1.1	Aging Effect	72
5.1.2	Influence of Trivalent Impurities	73
5.1.3	Discussion	75
5.2	Lineshape Analysis	77
5.2.1	Influence of Doping	83
5.2.2	MAS Measurements	84
5.2.3	Theoretical Analysis	85
5.2.4	Discussion	89
5.3	Relaxation Measurements	91
5.3.1	BPP Model	95
5.3.2	Non-Exponential Correlation Function	99
5.3.3	Model of Two Different Sublattices	100
5.3.4	Discussion	104
5.4	Results and Discussion	106
6	Summary	111
7	Zusammenfassung	113
	Bibliography	117
	List of Figures	125
	Acknowledgements	131

Chapter 1

Introduction

The first observations of high ionic conductivity within the solid state had already been performed in 1833 by M. Faraday [1–4] yet, to date, no universal "explanation" of the nature of the superionic conductors exists.

The fundamental understanding of this phenomenon has provided one of the major challenges in the field of condensed matter science. The experimental and theoretical approaches to the study of conduction processes are often very complicated [6]. Nevertheless, a clearer picture of the behavior of superionic materials has emerged within the past few decades. The solid state materials exhibit a high ionic conductivity, either of cations or anions, which is comparable to molten salts (in the order of $10^{-3}\Omega^{-1}\text{cm}^{-1}$) [7]. However, because of the huge variety in materials, neither the critical temperature of the transition into the superionic phase, nor the critical value of the ionic conductivity can be defined. The materials described in this work, for example, show no sharp transition into the superionic phase but undergo a gradual change of ionic conductivity. Numerous applications of these materials can be found ranging from gas sensors, electrodes, fuel cells, to scintillators etc. [5].

The goal of this work was to utilize the potential that the different NMR techniques offered for investigating BaF_2 -type superionic conductors and in this way learn more about the structure and fluorine dynamics at different time and length scales.

Magic-angle spinning and temperature-dependent lineshape measurements, especially on highly doped $\text{Ba}_{1-x}\text{La}_x\text{F}_{2+x}$ samples designed to clarify the debate of the structure, were of imperative interest. Field cycling (FC) data supported by theoretical analysis shed light on the movement of the interstitial and original ions on the micro-scale. In contrast to FC NMR, Static Field Gradient (SFG) measurements were intended to explore the macro-scale and to give some information about the temperature de-

pendent diffusion coefficients.

This work consists of five main chapters: chapter 2 to chapter 6. A short introduction to fast ionic conductors and to the structure of $\text{Ba}_{1-x}\text{La}_x\text{F}_{2+x}$ with its deviations is given in chapter 2. The background of NMR and theories for understanding and analyzing the experimental data are described in chapter 3. Experimental techniques and a description of spectrometers used, as well as the pulse sequences used for different experimental purposes are presented in chapter 4. In chapter 5 the experimental results are discussed in detail in order of the complexity of experiments and data analysis. Chapter 6 summarizes the whole work.

Chapter 2

Fast Ionic Conductors

In the past 60 years huge efforts, both experimental and theoretical, have been made in order to explain and describe the nature of fluorine dynamics in rare earth fluorides [7, 12–14]. Many materials having superionic properties were discovered. Some of them and their ionic conductivity, are illustrated in figure 2.1. It can readily be seen that not only crystalline ma-

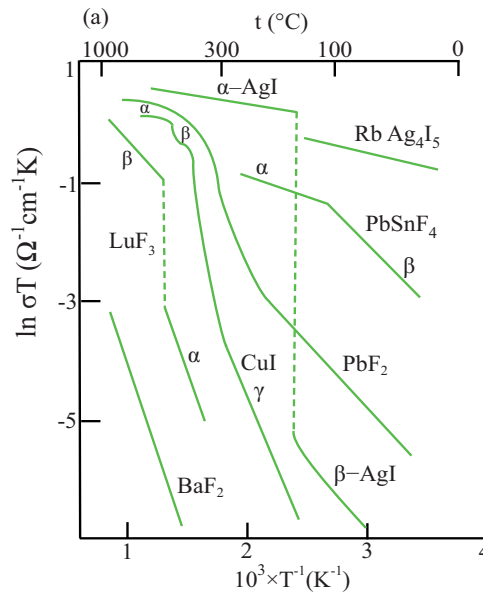


Figure 2.1: Arrhenius diagram of conductivity for a variety of fast ionic conductors [15]. In the left bottom corner data for BaF_2 are shown. The LaF_3 data are not presented on this diagram but in the temperature range of from 1.8×10^3 to $3.0 \times 10^3 \text{ K}^{-1}$ the conductivity of LaF_3 is between -5 and -3 $\ln \sigma T$ ($\Omega^{-1} \text{cm}^{-1} \text{K}$) [116].

terials are exhibiting fast ionic conduction, but also polycrystalline ones, ceramics, glasses, and polymers [7]. In fact, since the first observation of superionicity [2], the types of materials found to act as solid electrolytes are so numerous that various schemes for their classification into categories have been suggested. Categorization based on the form of their Arrhenius plots of conductivity [10], the nature of the charge carrier [7], as well as on structural aspects [16] have all been proposed.

Despite the diversity of the types of compounds which display fast ionic conduction, there are several characteristics that most, if not all, such substances possess. Since ionic transport and the dynamic properties of solid electrolytes are determined by the interaction between the crystal lattice ions, the common traits of this class of substances are most easily understood when one considers the binding energy E_i of a i^{th} mobile ion in a crystal lattice.

$$E_i = \sum_j A_{ij} \exp\left[\frac{r_i + r_j - r_{ij}}{\rho}\right] + e^2 \sum_j \frac{q_i q_j}{r_{ij}} - \frac{e^2}{2} \sum_j \frac{\alpha_j q_i}{r_{ij}^4} \quad (2.1)$$

where:

r_i and r_j are the ionic radii of mobile ions i and stationary ions j

r_{ij} is the inter-atomic distance

A_{ij} is the multiplicative factor dependent upon ion types

ρ is a constant, and q_i, q_j are the fractional charge of the mobile and fixed ion species, respectively

α_j is the polarizability of the j^{th} stationary atom

Various interaction potentials having appeared in literature serve as the basis for theoretical calculations [19] and are more or less similar to the energy of a lattice ion in an early work of Flygare and Huggins [17].

Considering equation 2.1, generalizations concerning factors which tend to minimize E_i and *a priori* enhance the conductivity of the mobile ions, can be made. It is well documented that those compounds in which the mobile species possess a small coordination number are generally better ionic conductors than those with mobile ions having a large number of nearest neighbors. For example, at moderate temperature LaF_3 , whose fluorine ions have a three-fold cation coordination, has a much higher specific conductivity than BaF_2 , where each F^- is tetrahedrally coordinated by cations. This is due to the fact that equation 2.1 is summed over all j lattice ions. Such considerations are in essence equivalent to the observation made by Kapustinskii that the Madelung constant increases with increasing coordination number [18].

A second criterion enhancing conductivity is a large polarizability for those atoms making up the immobile lattice. This increases the negative term in equation 2.1, thereby decreasing E_i . One can easily picture that a soft, highly polarizable atom is more apt to make room for an ion moving through the lattice. This fact is partially responsible for β -PbF₂ being the best conductor among conducting fluorides. Related to this preference for having soft ions in the rigid sublattice is the fact that superionic materials exhibit structural phase transitions at relatively low pressures and temperatures [31]. For example, the best fast fluorine conductor known to date is α -PbSnF₄ [32–34]. It also turned out that the dynamics of fluorine ions in a specially prepared two-dimensional α -PbSnF₄-sample are anisotropic. Static field gradient measurements of the diffusion coefficient D showed a higher value of D when the sample was oriented parallel to the B_0 magnetic field, figure 2.2.

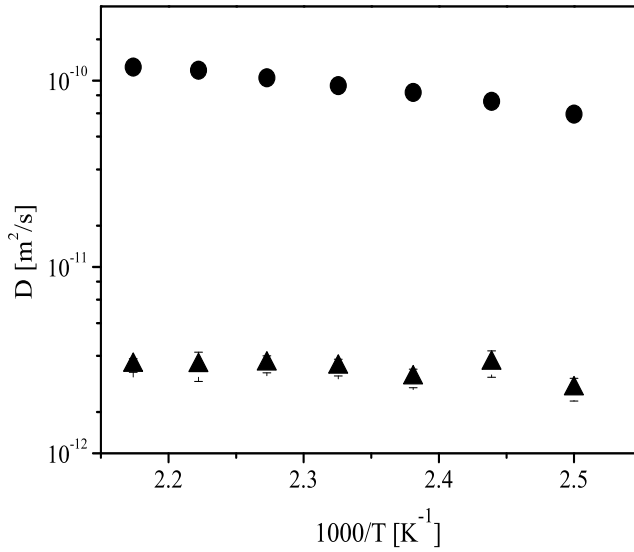


Figure 2.2: Diffusion coefficients depend on the orientation for PbSnF₄ superionic conductor. Circles: c-axis parallel to the B_0 magnetic field; triangles: c-axis perpendicular to the B_0 magnetic field.

An optimal, intermediate size exists for the moving ions in a given lattice. For example, the activation energy for the transport of Ag⁺ cations of hypothetical sizes was found to vary sharply with size in α -AgI [35].

This is caused by ions of extreme sizes having to overcome large energy barriers, due to the dominance of different terms in equation 2.1. The third criterion to be mentioned here is that compounds having monovalent ions tend to exhibit higher conductivities due to the smaller Coulomb force acting on the mobile species.

Another important point in increasing the ionic conductivity is the structure of the immobile sublattice and concentration of mobile ions. The presence of numerous unoccupied sites within the immobile sublattice will promote superionic behavior, but also requires the presence of low energy pathways between these sites to enhance the mobility μ . Also, the bonding character plays an important role. The preferred coordination of a mobile ion is a manifestation of the bonding character of the material. It has been suggested that mixed bonding character is an essential characteristic of good superionic conductivity by allowing the mobile ion to be stable in several different coordinations during the diffusion process. One more factor is also quite essential for the dynamics of ions: ionic charge. Lower charges result in lower Coulomb energies during diffusion.

In this work, an example is studied in which the conductivity, in this case that of the fluorine conductor BaF_2 , is increased through the introduction of a higher valent compound, LaF_3 .

2.1 Application

Solid ionic conductors can be divided into four classes [5]:

- **ion exchangers** are solids capable of exchanging some of the ions that participate in their structure. This means a high mobility of the two exchanging species at ambient temperature. Of particular interest is the identity of the exchanging species and the capacity of the solid for ion exchange.
- **solid electrolytes** are, ideally, electronic insulators but excellent conductors of a single ionic species selected for an application. Four criteria are used to judge the quality of a solid electrolyte:
 1. the working-ion conductivity σ_i : must be high enough to make the Ohmic losses tolerable under load conditions;
 2. the transport number t_i : should approach unity, $t_i \equiv \sigma_i/\sigma \approx 1$, where $\sigma = \sigma_e + \sum_i \sigma_i$ is the total electronic and ionic conductivity;

3. the reaction window: the electrolyte must be chemically inert under load conditions;
 4. ease of fabrication into thin, homogeneous membranes of high mechanical strength and density: use as a low-loss separator of liquid or gaseous reactants.
- **electrodes** are mixed electronic ionic conductors into which an ion may reversibly be electrochemically inserted as a mobile species, charge compensated by electrons in a host-matrix conduction band. In addition, a satisfactory electrode material must be able to sustain repeated insertion-extraction cycles under working conditions; for low Ohmic loss, the ionic conductivity must be high, especially in power cells.
 - **chemical stores** are similar to electrodes used for electrochemical storage; however, in use, the mobile ions are inserted into or extracted from molecular species, and both temperature and activity of the molecular species replace cell voltage as the variable controlling the insertion-extraction reaction.

Each of them has important applications with different fabrication requirements. Fast ionic transport is required in electric-power applications, and various strategies are discussed for batteries. The design of new materials begins with a theoretical model for ionic transport; the situation in stoichiometric compounds is compared with that in doped compounds, and electrolytes are contrasted with mixed ionic-electronic conductors. The most significant parameters for the synthesis are the factors that govern the activation enthalpy ΔH_m for diffusion, the concentration c of mobile carriers, and the temperature T_t for any phase transition from a normal to a fast ionic conductor. Strategies for decreasing ΔH_m and increasing c prove to be ion-specific, and the most successful strategies for each mobile ion can be found in literature [5,35].

2.2 Lattice Defects in Ionic Crystals

The transport of matter depends upon the existence of structural imperfections, and many electrical and optical properties of ionic crystals are likewise to be attributed directly to the occurrence of defects. One important group of imperfections is lattice defects. Their properties, in particular their ability to move through the lattice, are fundamental to the

understanding of many processes in the solid state. Three kinds of lattice defects may be distinguished:

- atoms or ions of the crystal may be found at metastable positions in the interstices of the lattice, between the regular sites of minimum potential energy. Such sites are termed interstitial positions,
- lattice sites may be unoccupied vacancies,
- lattice positions may be occupied by foreign atoms or ions, which may be taken up substitutionally at regular lattice sites, or if the impurities are small enough, they may occupy interstitial positions in the lattice.

The next section will present detailed information about the formation of lattice defects.

2.2.1 The Formation of Lattice Defects

Two possibilities for the formation of lattice defects were postulated by Frenkel and Schottky, respectively. Firstly, a cation or an anion may be displaced from its normal lattice site to a distant interstitial position. This is the Frenkel defect, which consists of an interstitial ion, combined with a vacancy. On the other hand, the Schottky defect consists of anion and cation vacancies present in equal number. These defects are formed from an ideal crystal if an equal number of anions and cations are removed from their normal lattice points to external or internal surfaces. Figure 2.3 illustrates these two cases. To calculate the activation energy and thus the formation of both types of defects, one has to consider a perfect stoichiometric crystal in thermal equilibrium, where the production of defects leads to an increase in entropy. The respective number of each type of defect present can easily be seen if the process of formation is looked upon as the analogue of a chemical reaction. Applying the Law of Mass-Action to the system in equilibrium results in:

$$K = \frac{n_i n_v}{(N - n_v)(N_i - n_i)} \quad (2.2)$$

where:

K concentration of defects

n_i number of ions in interstitial positions (at equilibrium)

n_v number of vacancies

N the total number of ions

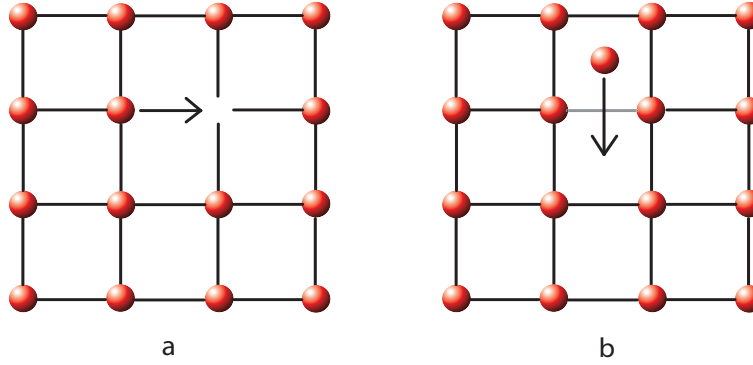


Figure 2.3: A schematic representation of different dynamical processes: a-left vacancy diffusion (Schottky defect), b-interstitial diffusion (Frenkel defect).

N_i total number of possible interstitial positions

and for the formation of the Frenkel defects: $n_i = n_v$ if now the degree of this order is $n_i \ll N$, then:

$$K = \frac{n_i n_i}{N N_i} \Rightarrow n_i^2 = N N_i K \quad (2.3)$$

If E_i is the energy required to form a Frenkel defect and if the process is assumed to occur at constant value, the following can be written:

$$n_i = \sqrt{N N_i K} \quad (2.4)$$

$$K = \exp\left(-\frac{E_i}{kT}\right) \quad (2.5)$$

$$n_i = \sqrt{N N_i} \exp\left(-\frac{1}{2} \frac{E_i}{kT}\right) \quad (2.6)$$

n_i number of Frenkel defects at thermal equilibrium

The number of Schottky defects may be derived similarly by proposing that a cation and an ion of the lattice interact with hypothetical sites beyond surface. The number of possible sites for reaction at the surface is simply the number of ion pairs per unit area of surface. Bearing in mind that the reverse process can occur if a surface ion drops into the vacancy, the Law of Mass-Action gives:

$$K = \frac{n_v N_s}{(N - n_v) N_s} \quad (2.7)$$

$$K = \exp\left(-\frac{E_v}{kT}\right) \quad (2.8)$$

where:

N_s number of ions pairs per unit area of surface

E_v is the energy required to form both a cation and an anion vacancy
for a small degree of disorder $n_v \ll N$:

$$K = \frac{n_v N_s}{N N_s} \Rightarrow n_v N_s = N N_s K \quad (2.9)$$

$$\Rightarrow n_v = N \exp\left(-\frac{E_v}{kT}\right) \quad (2.10)$$

The fact that ions adjacent to vacancies and interstitial ions have vibrational frequencies different from the normal ions may be described by a pre-exponential factor $\gamma = \left(\frac{\nu}{\nu'}\right)^x$, where ν' is the frequency of an ion adjacent to the vacancy; x is the number of ions which surround the vacancy; and ν is the normal frequency. These new factors lead to the modified equation 2.6 and 2.10

$$n_i = \gamma \sqrt{N N_i} \exp\left(-\frac{1}{2} \frac{E_i}{kT}\right) \quad (2.11)$$

$$n_v = C N \exp\left(-\frac{E_v}{kT}\right) \quad (2.12)$$

$$(2.13)$$

where:

C is a volume-dependent constant

Although in general both types of defects will occur, the respective energies necessary for their formation will usually be sufficiently different in any given crystal to make one type of disorder predominant over the other. Thus, if reliable estimates of the energies E_i and E_v can be made, it becomes possible to predict whether Schottky disorder or Frenkel disorder will predominate.

The first attempts at such calculations were made by Jost [36], who emphasized the importance of the polarization arising when a vacancy or an interstitial ion is formed. If polarization does not occur, the energy required to form Frenkel or Schottky defects in a crystal such as NaCl would amount to some 10eV. However, due to the polarization of the regions of the dielectric surroundings, the newly formed vacancies or interstitial ions, the overall energy requirement is reduced to about 3eV. The energy of the polarization in the case of the lattice defects is given approximately by the equation:

$$E_{pol} = -\frac{e^2}{a} \left(1 - \frac{1}{\epsilon}\right) \quad (2.14)$$

where:

e = electronic charge

a = radius of the ion

ϵ = dielectric constant

When the sizes of the cation and anion in a crystal are sufficiently different, as in BaF_2 , there is relatively more space for the smaller, F^- -ions in an interstitial position, with the result that the repulsive forces are not so strongly lowered. Furthermore, the introduction of a particularly small ion into an interstitial position will be accompanied by correspondingly large gains in polarization energy. These factors cooperate to render Frenkel disorder (Frenkel defects) of the smaller ion more favorable [52]. In addition to the relative size of the ions, other factors require consideration in assessing the relative magnitudes of E_i and E_v . For example, Frenkel disorder is favored by a large dielectric constant. As equation 2.14 shows, this leads to an increased contribution by the polarization energy, thereby offsetting the high repulsion energy. The Van der Waals energy arising from dispersion forces may also acquire importance. An ion in an interstitial position has a much higher Van der Waals energy than a normal lattice ion due to the close proximity of its neighbors. When an ion moves into an interstitial position, the magnitude of the gain in Van der Waals energy will clearly be greater than the Van der Waals energy of the ideal crystal. Thus, for crystals with high Van der Waals energy, this effect, which in combination with polarization operates against the repulsive energy, may be sufficient to render Frenkel disorder more likely than Schottky disorder. This is the case for fluorides [52] .

2.3 Crystal Growth

One of the methods for growing crystals is the Bridgman technique [37]. This method offers the possibility to grow crystals from aqueous solutions in cases where the solubility of the solute is very high. In such cases large quantities of solute are required to obtain a saturated solution, even in a small crucible, where not necessarily all of the material discharged in the cooling range goes to the growth of one crystal. Smaller volumes of solution and hence smaller amounts of solute can be used in the Bridgman variation, and operation can be performed at higher temperatures to increase the amount of solute if required. However, temperature gradients, stability at room temperature, imprecise control of the rotation of the crystal and other factors, combined with complicated phase diagrams can produce problems in obtaining high-quality single crystals.

The crystals made for analysis ($\text{Ba}_{1-x}\text{La}_x\text{F}_{2+x}$, $0.0005 \leq x \leq 0.45$) were grown under vacuum (0.13 Pa) at $\approx 1750\text{K}$ by Dr. Reiterov, by the Bridgman technique, using a radio-frequency (RF) heater. Out-gassed graphite crucibles containing intimately mixed powders of BaF_2 , LaF_3 , and PbF_2 as a scavenger for remaining oxygen and water vapor were loaded in a quartz tube which served as growth chamber. At this point it should be

fluoride	atmosphere	$a(\text{H}_2\text{O})$	$a(\text{HF})$	$a(\text{F})$	$a(\text{main hydrolysis product})$
LiF	100% Ar	9.6×10^{-7}	4.3×10^{-8}	2.3×10^{-17}	0.2l (LiO_{sol})
	100% HF	1×10^{-6}	1.0	3.7×10^{-10}	3.5×10^{-11} (LiOH_{liq})
	95% Ar + 5% CF_4	1.6×10^{-25}	2.0×10^{-6}	3.7×10^{-9}	1.6×10^{-23} (LiO_{sol})
CaF_2	100% Ar	9.1×10^{-7}	1.8×10^{-7}	9.7×10^{-17}	1.0 (CaO_{sol})
	100% HF	1×10^{-6}	1.0	3.7×10^{-10}	3.5×10^{-14} (CaO_{sol})
	95% Ar + 5% CF_4	1.6×10^{-25}	2.0×10^{-6}	3.7×10^{-9}	1.4×10^{-21} (CaO_{sol})
AlF_3	100% Ar	3.8×10^{-12}	1.4×10^{-6}	1.3×10^{-17}	1.0 ($\alpha\text{-Al}_2\text{O}_3$)
	100% HF	7.4×10^{-7}	1.0	1.4×10^{-11}	2.7×10^{-7} ($\text{AlOF}_{2,\text{g}}$)
	95% Ar + 5% CF_4	1.6×10^{-25}	2.0×10^{-6}	3.7×10^{-9}	3.4×10^{-12} ($\text{AlOF}_{2,\text{g}}$)

Figure 2.4: Equilibrium activities a of LiF, BaF_2 , and AlF_3 at 800°C in different atmospheres (1 bar total pressure). All atmospheres are assumed to contain 1 ppm H_2O (1×10^{-6} =initial humidity) [53].

mentioned that an atmosphere containing water can cause chemical reactions ($\text{F}^- + \text{H}_2\text{O} \leftrightarrow \text{OH}^- + \text{HF}$) and influence the equilibrium point of the crystal growth (subsection 2.3.1, figure 2.9). Table 2.4 compares the behavior of CaF_2 , LiF and AlF_3 in different atmospheres containing 1 ppm residual water [53]. Figure 2.5 demonstrates the influence on the surface of the crystal when the atmosphere contains too much water. Diffraction methods, Laue and powder X-ray diffraction did not reveal the presence of segregated solute for small values of x ($x = 0.0005, 0.01, 0.1, 0.3$).

Figure 2.6 presents laue reflection pattern of $\text{Ba}_{0.45}\text{La}_{0.55}\text{F}_{2.45}$ in which doubled reflections represent a typical pattern formed when the crystal is twinned. This may be related to the shape of the liquidus and solidus lines in the BaF_2 - LaF_3 phase diagram [9].

The solid solutions with $x = 0.3$ and 0.45 were not single crystals over the whole length and in the case of $\text{Ba}_{0.7}\text{La}_{0.3}\text{F}_{2.3}$ remaining CaF_2 material from the graphite crucibles was found additionally. It is very common to use the same crucibles for fluorides and if the cleaning is not done properly the new "mixture" can contain residual material. Figure 2.7 shows magic angle spinning data for a powder sample of $\text{Ba}_{0.7}\text{La}_{0.3}\text{F}_{2.3}$, bottom, and

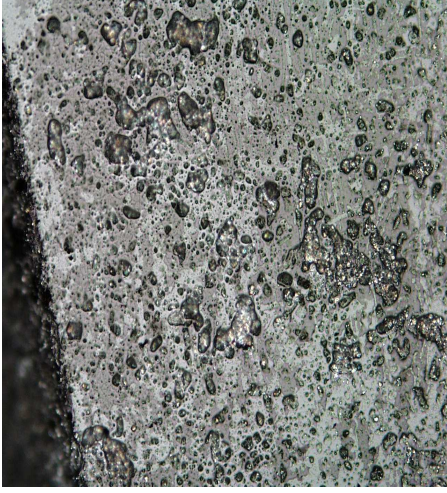


Figure 2.5: Picture of the surface of the $\text{Ba}_{0.55}\text{La}_{0.45}\text{F}_{2.45}$ sample under the influence of H_2O impurities. Made using optical microscopy.

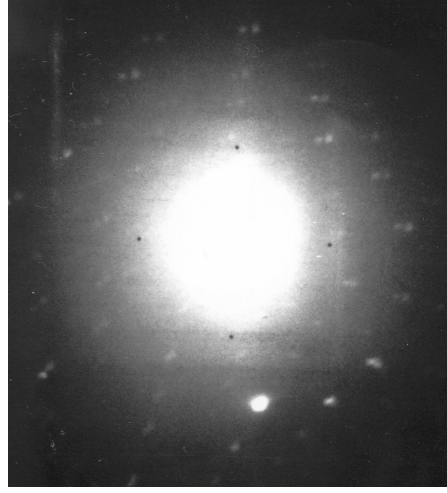


Figure 2.6: Laue reflection pattern of $\text{Ba}_{0.45}\text{La}_{0.55}\text{F}_{2.45}$. Doubled reflections represent a typical pattern formed when the crystal is twinned.

for pure CaF_2 used as a reference sample, top. On the left side of the big $\text{Ba}_{0.7}\text{La}_{0.3}\text{F}_{2.3}$ peak small CaF_2 is visible.

Not only X-ray diffraction but also other methods can give information about the quality of the crystal. Another very appropriate technique is Neutron Tomography, which measures neutron beam attenuation caused by an object, sample, placed in the beam, between the n-source and detector.

$$I(\rho, \theta) = I_0 \exp\left(-\int_{-\infty}^{\infty} \sum(x, y) ds\right) \quad (2.15)$$

The difference in attenuation coefficients should be large enough to facilitate the distinction on the cross-sectional images of the sample.

The analysis of the object by neutron radiography is mostly done taking one or more 2D parallel projections. In some cases, however, the transmission properties of the object seen from any angle are desired. This can be achieved by rotating the object in angular increments over 180° and calculating tomographic slices using the inverse Radon transform. As an example, figure 2.8 shows four different slices of $\text{Ba}_{0.7}\text{La}_{0.3}\text{F}_{2.3}$, where small parts of the sample have different colors, which equate to different attenuation coefficients and in this way show different concentrations of elements in the sample. Combining this method with X-ray diffraction

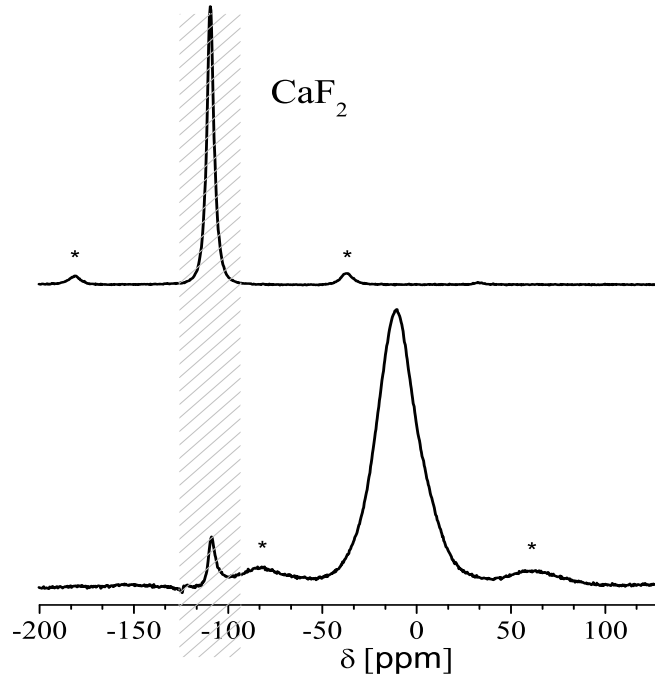


Figure 2.7: Magic angle spinning data for the $\text{Ba}_{0.7}\text{La}_{0.3}\text{F}_{2.3}$ -powder sample, bottom, and for pure CaF_2 used as a reference sample, top. On the left side of the bottom spectrum, one additional CaF_2 -peak appeared. Stars denote spinning side bands.

tion, identification of polycrystalline regions, which should be excluded in further investigations, can be made. As already mentioned above, the problems can be explained with the aid of the phase diagram, so a deeper understanding of the phase diagram of the BaF_2 - LaF_3 systems is required.

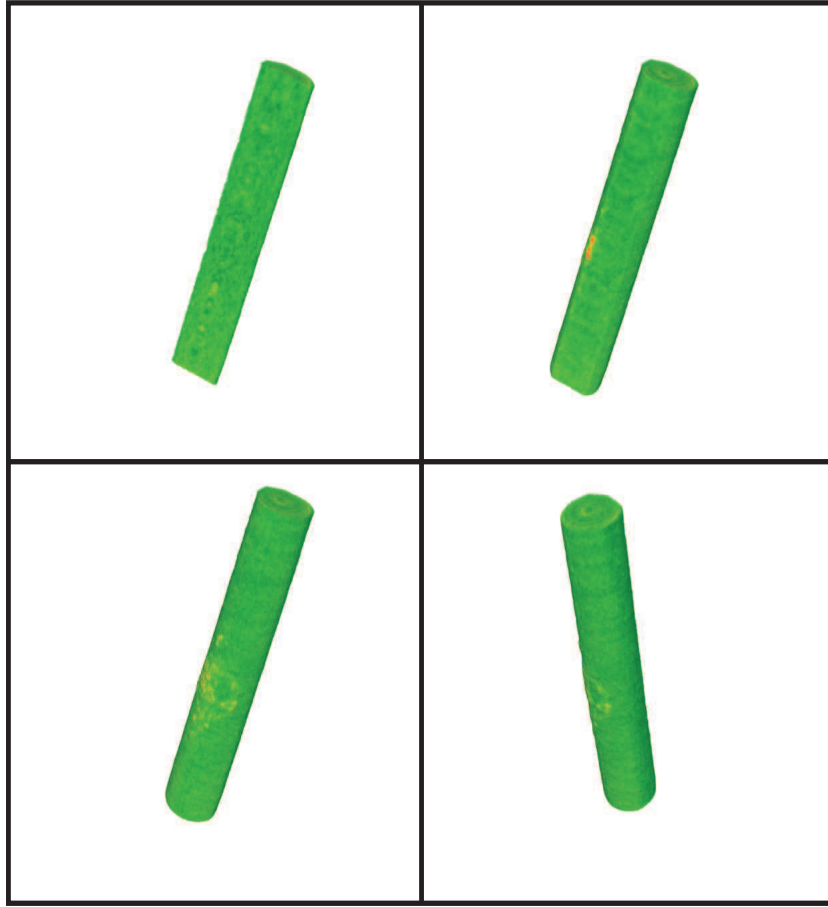


Figure 2.8: Neutron Tomography of the $\text{Ba}_{0.7}\text{La}_{0.3}\text{F}_{2.3}$. Four different orientations and cross-sections. Different colors defined the different concentration of Ba or La elements; green Ba, red La.

2.3.1 Phase Diagram

The history of experimental investigations of the BaF_2 system doped with LnF_3 (Ln-lanthanum and lanthanides) began in 1914 [38], when the fusion of YF_3 solid solutions and fluorite was found to have a maximum at about 12 mol.% of yttrium fluoride. Interest in these systems (or, more precisely, in $\text{Ba}_{1-x}\text{Ln}_x\text{F}_{2+x}$ solid solutions with the fluorite structure type) grew after the production of the first lasers based on fluorides ($\text{CaF}_2:\text{U}^{3+}$ [39]). Of the important fields of use for materials based on the BaF_2 - LaF_3 system, materials for the optical processing of information [41–43] and the conversion of IR quanta into visible light [44] must be mentioned; the components

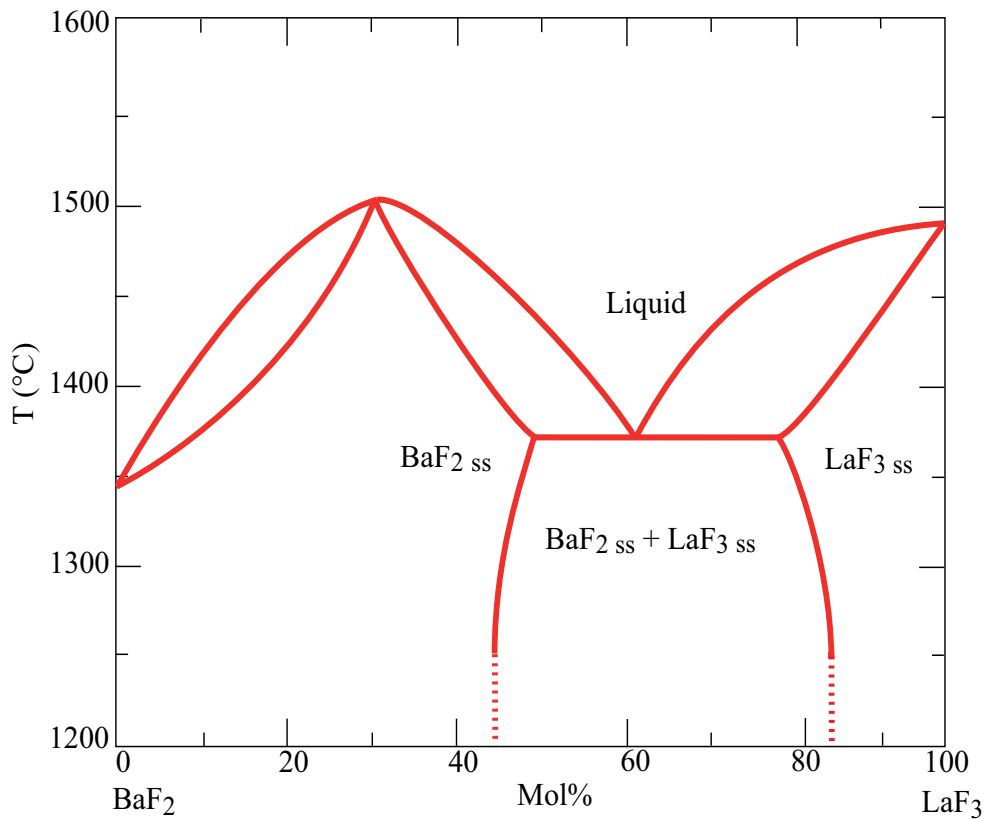


Figure 2.9: Phase Diagram of the BaF₂+LaF₃-system. Only the high temperature part is shown [38].

and certain compositions of these systems are used as solid electrolytes with high ionic conductivity [45, 46], thin film condensers [40] etc. A pronounced effect of La³⁺ impurities on the mechanical characteristics of fluorite [47] was noted. The fusibility within these systems is of interest for an understanding of the electroslag melting of certain metals [48] and the physicochemical basis of the process of thermal reduction of lanthanide fluorides with calcium [49].

Despite the fact that numerous investigations of BaF₂-LaF₃ system (and its components) have been made, a large number of problems still remain unsolved. The BaF₂-LaF₃ system encompasses both pure BaF₂ and LaF₃, but also mixed components, called solid solutions. For the construction of a correct phase diagram of these solid solutions, it is necessary to know the temperatures of all phase transitions of the components within the investigated composition range. Earlier studies of systems containing LaF₃

have been invalidated because measurements of the oxygen concentration of the specimens after thermal treatment were neglected [50,51].

The phase diagram of the BaF_2 - LaF_3 system for temperatures ranging from 1250°C to the melting point (1500°C) is given in figure 2.9, where the phase designations are as follows: BaF_{2SS} , solid solution with fluorite structure; $\text{BaF}_{2SS}+\text{LaF}_{3SS}$, region where a mixture of the BaF_2 structure, cubic and tysonite structure exists; LaF_{3SS} phase with tysonite structure.

The phase with fluorite structure is on the left hand side of figure 2.9 and the maximum concentration of LaF_3 possible within this structure (BaF_{2SS}) is 50 mol.%. Attempts to grow single crystals with such high concentration may be accompanied by many problems connected with the shape of the liquidus and solidus curves presented on the right side of the phase diagram. Detailed analysis of this process can be found in literature [38].

2.4 Solid Electrolytes with Fluorite Structure

There are several fast-ionic conductors having fluorite (CaF_2) structure. These not only include fluorine conductors, but oxygen conductors, and lithium ones as well [5]. In the next section, precise descriptions of the fluorite structure, formation of lattice defects and influence of these on fluorine dynamics are given.

2.4.1 Fluorite Structure

The cubic fluorite crystal structure (space group $\text{Fm}\bar{3}\text{m}$ [38]) can be described as a face-centered cubic (fcc) array of cations in which all the tetrahedrally coordinated interstices are filled with fluoride anions and the octahedrally coordinated ones are empty (see figure 2.10). However, to describe the nature of the anionic disorder it is often more convenient to illustrate the anionic arrangement as a simple cubic array of ions with cations occupying alternating cube centers (see figure 2.11). Here each metal atom is surrounded by eight anions and each anion is tetrahedrally coordinated by four metal atoms.

Lattice distortions Much investigative work on the structure and disorder in BaF_2 -systems has been done by A. K. Cheetham, N. H. Andersen, J. Schoonman and many others [54–60]. They proved that in the fluorite structure, the doping by trivalent rare-earth elements R^{3+} substantially enhances the disorder and ionic conductivity [62].

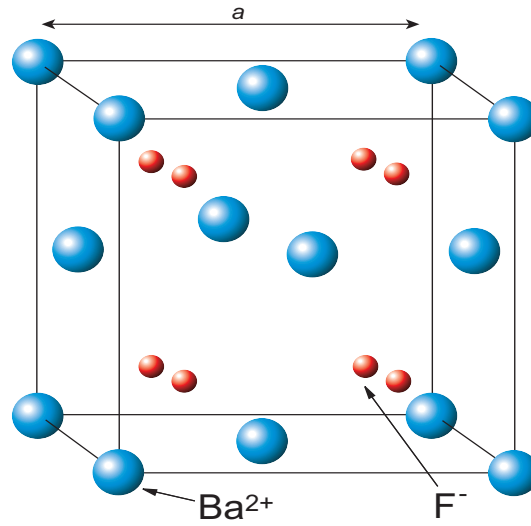


Figure 2.10: Fluorite Structure, unit cell (space group $\text{Fm}\bar{3}\text{m}$ [38]).

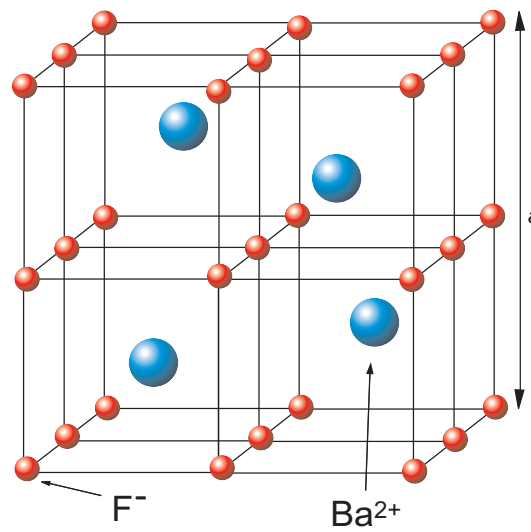


Figure 2.11: The cubic fluorite crystal structure, illustrated as a simple cubic array of anions (F^-) with cations (Ba^{2+}) occupying alternate cube centers.

2.4 Solid Electrolytes with Fluorite Structure

As already mentioned in section 2.3.1, the overall cubic, crystal symmetry in case of $\text{Ba}_{1-x}\text{La}_x\text{F}_{2+x}$ is conserved within $0 \leq x \leq x_{\max}$ where $x_{\max} \approx 0.5$. The lanthanum ions substitute for the barium atoms and near each lanthanum atom there is one charge-compensating F^- anion at an interstitial site. At heavy doping (approximately $x \gtrsim 0.01$) the crystal defects

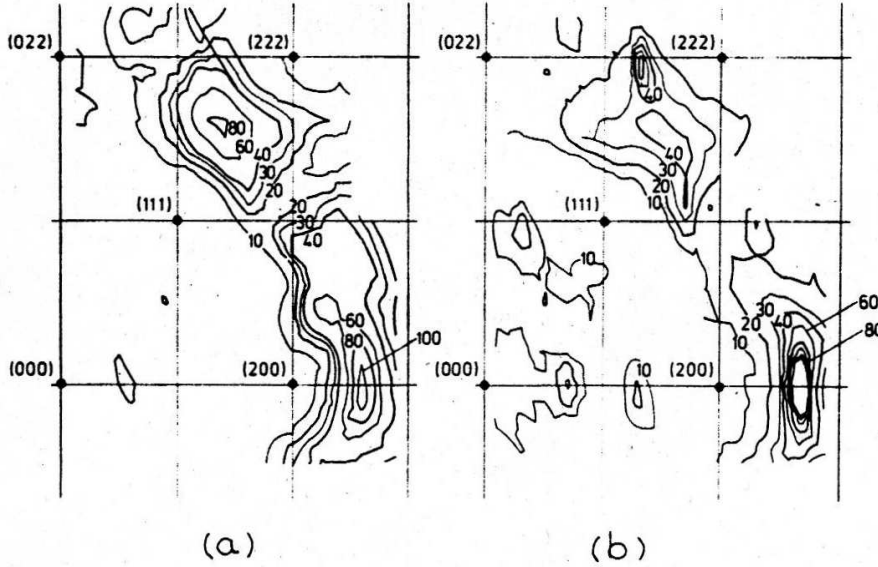


Figure 2.12: Contour map of the diffuse elastic scattering for $\text{Ba}_{1-x}\text{La}_x\text{F}_{2+x}$ at room temperature, (a) $x=0.209$ (b) $x=0.492$. The labels on the contour denote the arbitrary units of the intensity.

gather into clusters [54]. The lattice in the vicinity of the clusters is deformed, which leads to so-called defect regions [55,62] in the undeformed fluorite lattice. Based on calculations, such deformations in BaF_2 have been estimated earlier to be of the order of several percent of the lattice constant and to be limited to the atoms in the close vicinity of the defects [54].

Important evidence about the cluster structure and configuration in the $\text{Ba}_{1-x}\text{La}_x\text{F}_{2+x}$ single crystals was obtained by diffuse neutron scattering experiments [54, 55, 62] performed by A. K. Cheetham, N. H. Andersen, J. Schoonman. They have been measuring a room-temperature contour map of elastic scattering in the $(0\bar{1}1)$ plane for $x=0.209$ and $x=0.492$, which is shown in figure 2.12. These patterns bear a strong resemblance to the high-temperature results of integrated quasi-elastic scattering intensities in CaF_2 , [62] which could be reproduced very well by model calculations

based on clusters similar to the 222 cluster defects. The 222 cluster configuration is shown in figure 2.13. With the distances given in units of

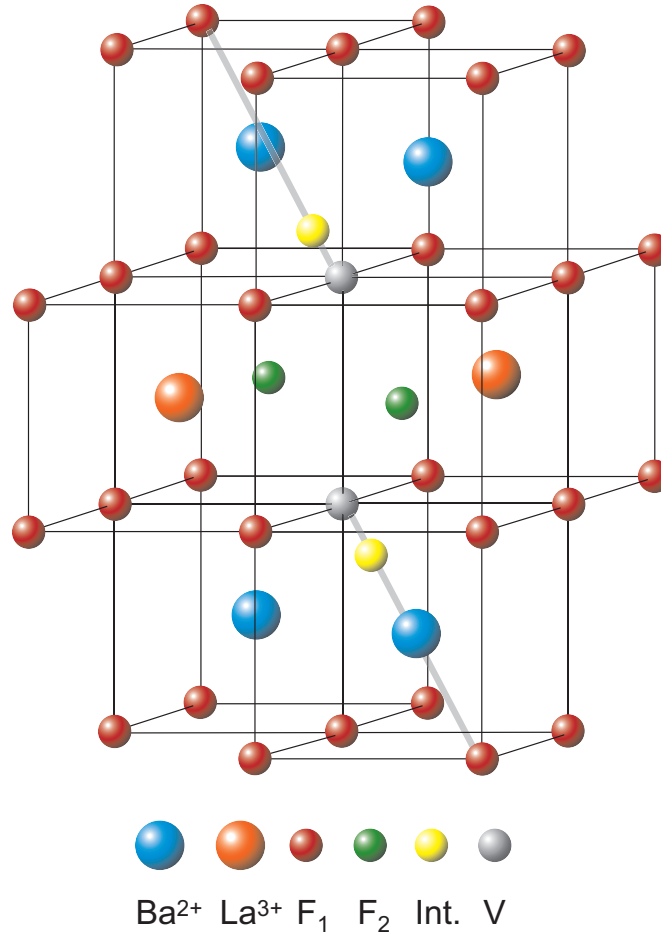


Figure 2.13: Extrinsic defect clusters proposed to accommodate additional F⁻ within the Ba_{1-x}La_xF_{2+x}-system [54].

the lattice constant a , the 222 cluster can be characterized by the following three defect features:

- randomly substituted pairs of lanthanum ions on barium sites,
- pairs of excess fluorine ions situated on interstitial sites but displaced $(\delta - \frac{1}{4})x\sqrt{2}$ along a (110) direction from the body center of the simple fluorine interstitial cube,
- two relaxed fluorine ions displaced $3^{1/2}\varepsilon$ along the (111) plane from a regular fluorine site.

The model calculation used by N.H. Andersen et al. [62] bases on the outline given by Hutchings et al. (1984) [17]. It took into account the various ways in which the cluster can be formed according to the lattice symmetry.

2.4.2 Transport Mechanisms

In this section a general presentation of the transport mechanisms supported by experimental examples will be given. More detailed theoretical treatment can be found in a number of texts (see, for example, the reviews by Lidiard (1974) [113], Maier [112] and book Corish and Jacobs (1973) [114]).

Diffusion In a crystal, the occurrence of diffusion is contingent upon the availability of point vacancies throughout the crystal lattice. Diffusing particles migrate from point vacancy to point vacancy. Since the prevalence of point vacancies increases in accordance with the Arrhenius equation, the rate of diffusion increases with temperature. This can be described by the First Law of Diffusion:

$$J = -D \frac{\delta C(r, t)}{\delta r} \quad (2.16)$$

where J is the particle flux, C is the concentration of the solute, D is the diffusion coefficient, r is the distance into the substrate, and t is the diffusion time. The negative prefix indicates that the diffusing mass flows in the direction of decreasing concentration. Combined with the Conservation of Mass, the First Law of Diffusion, the Second Law of Diffusion (known as Fick's Law) can be derived, which states:

$$\frac{\delta C}{\delta t} = D \frac{\delta^2 C}{\delta r^2} \quad (2.17)$$

In order to solve Fick's Law, an initial condition and boundary conditions are required. One solution, in which the diffusion is caused by thermal energy, is called free diffusion. In this case, the path of motion will be followed, and the initial condition is defined by the particle being located at its original position r_0 at time $t=0$. Taking that into account, the second Law of Diffusion can be rewritten, introducing the probability density $P(r, t)$ of finding an individual particle at r at some later time t :

$$\frac{\delta P(\vec{r}, t)}{\delta t} = D \frac{\delta^2 P(\vec{r}, t)}{\delta r^2} \quad (2.18)$$

The solution then is the Gaussian propagator:

$$P(r, t) = (4\pi Dt)^{-\frac{3}{2}} \exp\left(-\frac{r^2}{4Dt}\right) \quad (2.19)$$

From this equation the mean square displacement or diffusion length, can be derived, where t is the time since start of the diffusion.

$$\langle r^2 \rangle = 6Dt \quad (2.20)$$

This was derived by Einstein in 1905. Further information about different solutions of the Law of Diffusion can be found in literature [115].

2.4.3 State of the Art

Taking a broader view of on the field of superionic conductors, some progress has been made by both, experimental [63, 64] and computational [65] methods to reconcile the different superionic transition mechanisms within fluorite-structured compounds. This section will provide a brief review on this progress. It is now widely accepted that the fluorite-structured halides SrF_2 , CaF_2 , and BaF_2 undergo a gradual increase of ionic conductivity towards the superionic state, characterized by the transition temperature, T_c (see table below, T_m the melting temperature). At this temperature, a peak in the specific heat C_p , occurs and the ionic conductivity, σ , begins to saturate [13]. The high value for ionic conductivity observed in superionic BaF_2 -type materials is almost entirely due to anion diffusion, owing to the comparatively large energy required for cation defect formation and the large electronic band gap. The studies done by Figueroa, Chadwick, and Strange have focused attention on ionic diffusion in BaF_2 [66].

COMPOUND	T_c ($^\circ\text{C}$)	T_m ($^\circ\text{C}$)
CaF_2	1150	1418
BaF_2	960	1320
SrF_2	1180	1320
PbF_2	430	820

They attempt to resolve the discrepancies and provide quantitative and reliable determinations of self-diffusion coefficients in this system. In the first step, the ionic conductivity was investigated throughout the temperature range 450K-1125K [66]. In figure 2.4.3, the results for nominally pure BaF_2 are shown, plotting $\ln \sigma T$ as a function of reciprocal temperature. Also shown are the results for four lanthanum doped samples, one potassium doped and one oxygen doped sample. The conductivity of the pure

material spans eight decades and shows no evidence of extrinsic (charge compensating) behavior. The absolute values obtained for the intrinsic conductivity (thermally-induced) agree to within $\pm 20\%$ with the previously reported values of Fielder [67] and Barsis and Taylor [68]. However, the values obtained by Figueroa are about 40 % higher than those measured by Bollmann [52]. The intrinsic behavior of the pure material does not result in a simple straight line plot (2.4.3). Activation energy calculated from the temperature region 450K-800K is equal $\Delta E = 1.52\text{eV}$ for almost all doped samples with the exception of BaF_2 doped with an unknown concentration of O^{2-} impurities. At higher temperatures, an upward curvature is apparent, indicating the presence of more than one conduction mechanism. In this region the conductivity can be attributed to both F^- vacancy and F^- interstitial motion. Of the two, the vacancy has the lower activation energy of migration, as can be seen from the conductivity results of the doped samples. For the fluorite lattice, there are two possible diffusion mechanisms that should be considered to involve interstitial ions: the direct interstitial mechanism involving $\langle 110 \rangle$ jumps and the non-collinear interstitially mechanism. This latter mechanism requires a much smaller energy to produce the required ionic displacements [69].

The ionic conductivity results for BaF_2 containing various La^{3+} impurity concentrations become superimposed at the highest temperatures. The extrinsic regions give almost parallel plots with a gentle slope towards lower temperatures, which can be ascribed to association of the La^{3+} ions with F^- interstitial ions. Figure 2.4.3 shows the calculated self-diffusion coefficients for different $\text{Ba}_{1-x}\text{La}_x\text{F}_{2+x}$ crystals. The dashed line represents the values calculated from conductivity data, assuming a vacancy model [66]. It can be seen that the overall diffusion plot displays the same general features for both techniques. Figure 2.4.3 shows that in the high temperature region (above $\sim 800\text{K}$), the nuclear spin relaxation is due to relative motion of the ions arising from the movement of thermally generated defects, which dominates over any contribution from impurities (i.e., the intrinsic range). At temperatures well below 800K, extrinsic diffusion takes place. It should be noted that those two techniques analyze atomic motions in very different ways. The NMR relaxation time method provides a *spectrum* of ionic jump frequencies, which must then be related to ionic diffusion coefficients via a suitable theory. The method therefore detects "local motion" on an atomic scale, whereas conductivity, which is a bulk property, measures the motion of "charged" defects (e.g. vacancies and interstitials) averaged over many jumps, and again must be related to mass transport via a suitable theory.

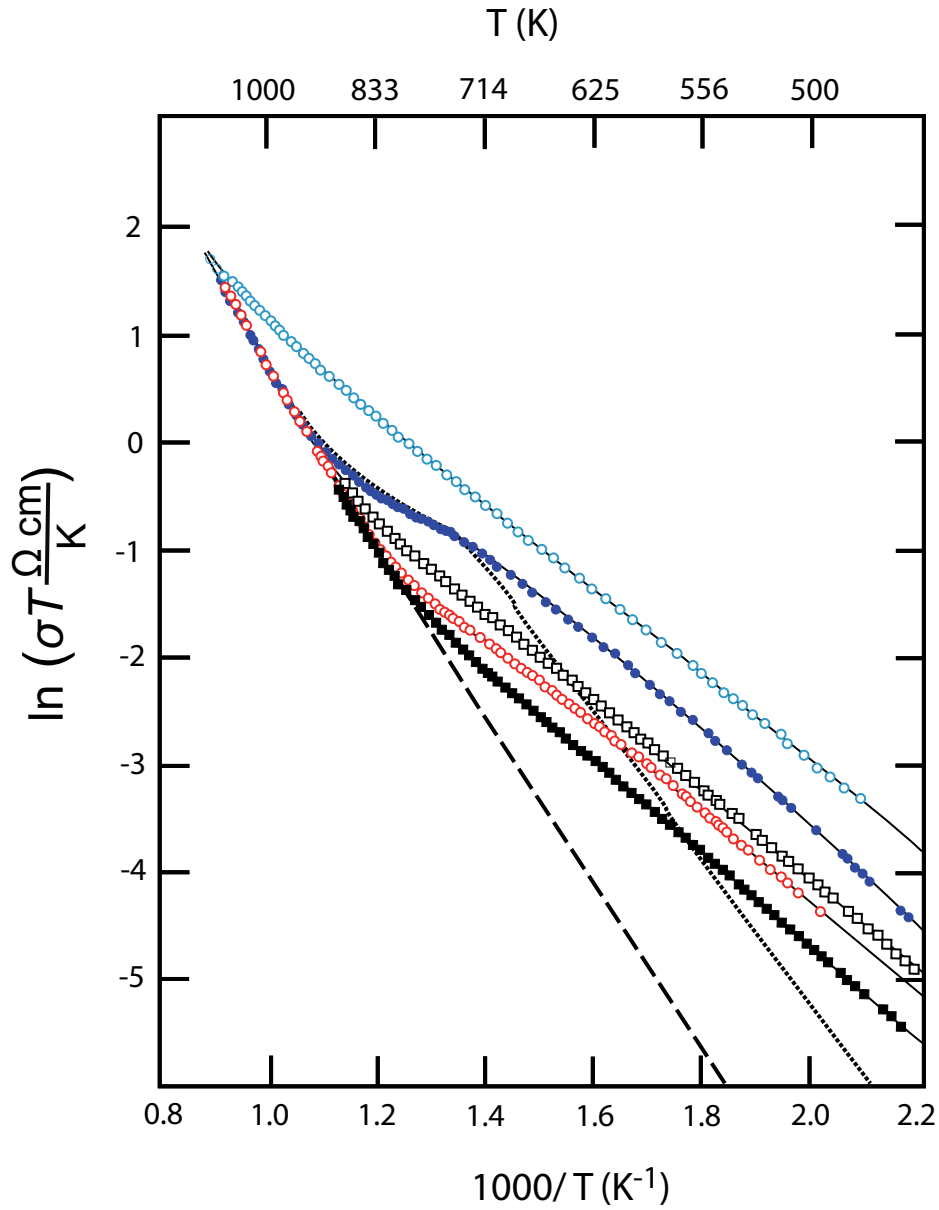


Figure 2.15. Temperature dependent conductivity data for BaF_2 , crystals containing: ■ 0.0285 mole % LaF_3 ; ○ 0.05 mole % LaF_3 ; □ 0.0920 mole % LaF_3 ; ○ 1.2 mole % LaF_3 ; ● 0.04 mole % KF ; . . . unknown concentration of O^{2-} impurities: - - - nominally pure BaF_2 . Figure adapted from [66].

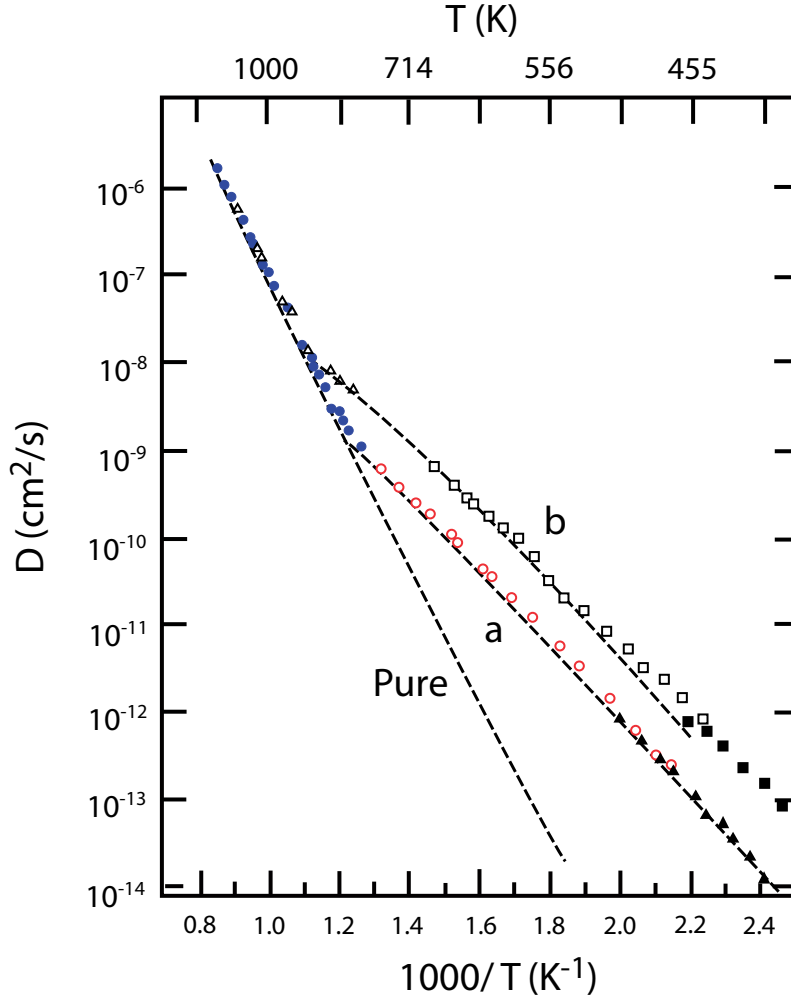


Figure 2.16. Fluorine self-diffusion coefficients of BaF_2 obtained from conductivity and spin-lattice relaxation measurements. Single crystals containing cation impurities: (a) 0.05% LaF_3 , doped BaF_2 :

$---$ D_F^σ ; \bullet $D_F^{\text{NMR}}(T_1)$; \circ $D_F^{\text{NMR}}(T_{1\rho})$;
 \blacktriangle $D_F^{\text{NMR}}(T_{1D})$. (b) 0.04% KF doped BaF_2 : $---$ D_F^σ ;
 \triangle $D_F^{\text{NMR}}(T_1)$; \square $D_F^{\text{NMR}}(T_{1\rho})$; \blacksquare $D_F^{\text{NMR}}(T_{1D})$.

Figure adapted from [66].

Chapter 3

Essential Aspects of Solid State NMR Theory

In this chapter, some of the essential features and interactions in Nuclear Magnetic Resonance will be considered. More details can be found in a large number of books and reviews that cover this subject in much greater detail [71–76].

3.1 The Phenomenon of Nuclear Magnetic Resonance

Nuclear Magnetic Resonance observes the behavior of the magnetic moments of nuclei (macroscopic magnetization, \vec{M}). This magnetic moment is proportional to the spin according to the equation:

$$\mu_I = g_I \frac{e\hbar}{2m_p} \sqrt{I(I+1)} \quad (3.1)$$

where I denotes the corresponding spin quantum number, e is the elementary charge of the electron, m_p is the proton mass, and g_I depends on the considered nucleus. The I manifold splits in an external magnetic field \vec{B}_0 into $2I+1$ allowed values of the component of the nuclear spin along the magnetic field. This component can be characterized by the magnetic spin quantum number m_I , which is in the range $\pm I$, and differs by $|\Delta m_I|=1$. Therefore, in an external magnetic field, the available states are described by $2I+1$ wave functions, which form a complete basis $\{|I, m_I\rangle\}$. Generally, in the presence of other spin interactions (such as quadrupole coupling, dipole-dipole coupling, examples are given in the next sections), the

basis functions do not correspond to eigenfunctions of the considered nuclear spin. The function $|I, m_I\rangle$ describes the eigenstates of the spin, and thus it is called the eigenfunction. The interaction energies, eigenvalues of the eigenstates can be written as:

$$E_I = -\gamma_I \hbar B_0 m_I = -\omega_I \hbar m_I \quad (3.2)$$

The coefficient γ_I refers to the gyromagnetic ratio, while the frequency ω_I is called Larmor frequency. This nomenclature comes from the classical picture of magnetic resonance, where ω_I is the precession frequency of the nuclear magnetic moment around the external magnetic field \vec{B}_0 . For transitions between two "neighboring" energy levels, ω_I is simply the transition frequency. An ensemble of spins in the presence of a static ex-

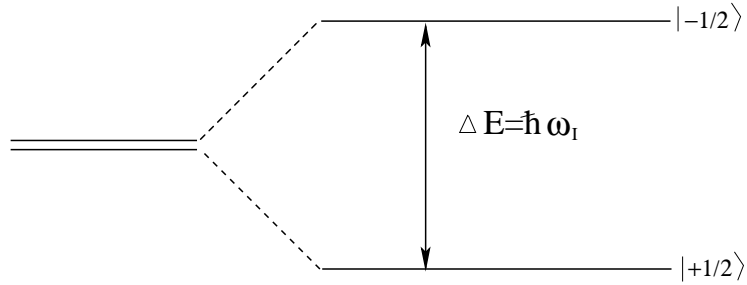


Figure 3.1: Energy levels of spin I , where $m_I = \pm \frac{1}{2}$

ternal magnetic field \vec{B}_0 leads to a macroscopic magnetization \vec{M} aligned along \vec{B}_0 . Magnetic resonance experiments are in most cases based on an external magnetic field \vec{B}_0 , in which the sample is placed, as well as an oscillating magnetic field \vec{B}_1 perpendicular to \vec{B}_0 , that induces transitions between the energy levels (Figure 3.1).

3.2 Classical Treatment of the Relaxation

Classical treatment consists of a macroscopic magnetization precessing on a cone around \vec{B}_0 . A very good description of it can be found in the text book of M. Levitt [76]. For this work more attention is put on the effects of relaxation which can be in general described as a phenomenon that brings spin systems back towards their equilibrium state. In NMR, it is a reinstatement of nuclear magnetization \vec{M} to its equilibrium configuration after it has been perturbed. The longitudinal component of the magnetization (parallel to the applied static magnetic field \vec{B}_0) recovers

to the equilibrium magnetization with a relaxation time T_1 , called spin-lattice relaxation time, while the transverse magnetization (perpendicular to magnetic field \vec{B}_0) disappears with the spin-spin relaxation time T_2 . Due to the transverse relaxation mechanism (the spin-spin relaxation), the spin system establishes thermal equilibrium within itself, while the longitudinal (spin-lattice) mechanism brings the system to thermal equilibrium with the lattice. The consideration of only two relaxation times is a simple view. Nevertheless, this simplified picture is very useful in understanding the basis of spin relaxation.

To perturb a spin system from its equilibrium configuration or to take it back to its equilibrium state transitions can be induced. The longitudinal relaxation involves energy exchange between the spins and the lattice. If the population of the high energy state of a particular spin state is larger than its equilibrium value, it will relax back towards equilibrium by spins flipping from a high energy to a low energy state. The lattice then gains the energy released from the spin population and for example transfers it to the atomic motion. However, the relaxation transitions can only occur if there is an interaction that couples the motion of the molecule to the spin states. Depending on the system, relaxation processes are caused by the various interactions to which nuclear spins are subjected. All elementary magnetic moments in a macroscopic sample sense local magnetic fields arising from various effects. One of the most common relaxation mechanisms is the one caused by dipole-dipole interactions between the magnetic moments.

Another important point should be mentioned: to cause relaxation, the interactions must fluctuate in time. The spin interactions are mediated by various motional processes, like translation diffusion, exchange motion, lattice vibrations, etc. Thus, the local magnetic fields created by these interactions fluctuate in time and should induce transitions. The time scale of the fluctuations should be appropriate to provide an efficient mechanism for spin transitions. All the mechanisms which contribute to the spin-lattice relaxation also contribute to the spin-spin relaxation, because the restitution of the equilibrium populations brings zero magnetization in the plane perpendicular to the B_0 direction. There are, however, processes which influence the transverse relaxation, but do not affect the longitudinal relaxation. These two processes are significantly different. Only energy exchange with the lattice contributes to the longitudinal process. Spin-spin flip-flop transitions do not involve energy exchange between spin and lattice, therefore they do not contribute to the spin-lattice relaxation, but they do contribute to the spin-spin relaxation. For this reason,

the transverse relaxation is called spin-spin relaxation. These two types of relaxation are sometimes linked, in the sense that one influences the other. The phenomenological description of the relaxation processes was done by Felix Bloch in 1946 [117], and can be pictured using the following set of equations:

$$\frac{dM_z}{dt} = \frac{M_0 - M_z}{T_1} \quad (3.3)$$

$$\frac{dM_x}{dt} = -M_y(\omega_0 - \omega) - \frac{M_x}{T_2} \quad (3.4)$$

$$\frac{dM_y}{dt} = M_x(\omega_0 - \omega) - \frac{M_y}{T_2} \quad (3.5)$$

where M_x, M_y, M_z are the magnetization components along the x, y, z axes ($B_0 \parallel z$), M_0 is the equilibrium magnetization, ω_0 is the Larmor frequency, and ω is the measuring frequency.

3.3 Quantum Mechanical Treatment

Although a classical treatment of NMR gives a good picture of the behavior of the macroscopic magnetization, it cannot be successfully applied to explain all effects and processes taking place in the micro-world. That is why another approach has been taken to clarify the mystery of spin-behavior. In this section, the new formalisms and a clear description of the spin systems under different conditions will be given.

3.3.1 The Density Matrix Representation

One approach to describe the spin system is the method of the density operator or density matrix. Considering a collection of identical spin systems, each of which can be in any one of N states labeled as ψ , it is possible to describe the state of each individual spin system using the probability p_ψ of it being in a particular state, ψ . This leads to the description of the state of each spin system with Ψ , where $\Psi = \sum_\psi p_\psi \psi$. The expectation value of a quantity A with corresponding operator \hat{A} over the sample is given by:

$$\langle \hat{A} \rangle = \sum_\psi p_\psi \langle \psi | \hat{A} | \psi \rangle \quad (3.6)$$

where the summation is over all the possible states for each individual spin system, and where it could be assumed that the wave function Ψ

is normalized. The state of the system in a general form as a sum over functions ϕ_i can be written:

$$\psi = \sum_i c_{\psi i} \phi_i \quad (3.7)$$

substituting this into equation 3.6 one gets:

$$\langle \hat{A} \rangle = \sum_{\psi} p_{\psi} \sum_{i,j} c_{\psi j}^* c_{\psi i} \langle \phi_i | \hat{A} | \phi_j \rangle \quad (3.8)$$

The advantage of this approach is that the matrix elements of \hat{A} in this basis ($\langle \phi_i | \hat{A} | \phi_j \rangle$), are the same whichever state Ψ one deals with. Defining the $\sum_{\psi} p_{\psi} c_{\psi j} c_{\psi i}^*$ to be ij th element of another matrix ρ , turns the equation 3.8 for the expectation value of \hat{A} into:

$$\langle \hat{A} \rangle = \text{Tr}(A\rho) = \sum_i (A\rho)_{ii} = \sum_i \sum_j A_{ij} \rho_{ji} \quad (3.9)$$

where A is the matrix of operator \hat{A} in the $\{\phi_i\}$ basis whose ij th element is $\langle \phi_i | \hat{A} | \phi_j \rangle$. The matrix ρ , called the density matrix, has a corresponding operator which can be deduced by inspecting its matrix elements, i.e. $\rho_{ji} = \langle \phi_j | \hat{\rho} | \phi_i \rangle = \sum_{\psi} p_{\psi} c_{\psi j} c_{\psi i}^*$:

$$\hat{\rho} = \sum_{\psi} \rho_{\psi} |\psi\rangle \langle \psi| \quad (3.10)$$

Further details can be found in Goldman's text [79].

3.3.2 Coherences and Population

The diagonal elements of the matrix representation of the density operator are equal to:

$$\rho_{ii} = \sum_{\psi} p_{\psi} c_{\psi i}^* c_{\psi i} = \overline{c_{\psi i}^* c_{\psi i}} \quad (3.11)$$

The bar means "average over all the spins" or *ensemble average*, represented by ψ in equation 3.11, the weighted sum over all possible states for the spin system. Equation 3.11 shows that ρ_{ii} is simply the average population of the ϕ_i basis function over the sample, as $c_i^* c_i$ is the population of the i th basis function. The off-diagonal elements of the density matrix are then defined:

$$\rho_{ij} = \sum_{\psi} p_{\psi} c_{\psi i} c_{\psi j}^* = \overline{c_{\psi i} c_{\psi j}^*} \quad (3.12)$$

They represent the population of the basis functions in the state Ψ' . If a distribution of spin systems among all possible states exists in a sample, then the averaging over states from the equation 3.12 causes the off-diagonal elements to vanish. One condition has to be fulfilled: the off-diagonal elements vanish if there is no correlation between the basis functions from which the spin system states are derived over time. If the correlation between the basis functions exists, the average in equation 3.12 no longer vanishes, and off-diagonal elements of the density matrix will be non-zero. This case is represented by a coherence between the ϕ_i and ϕ_j functions in the state Ψ , which describes the spin system.

3.3.3 Essential Aspects of the Perturbation Theory

The relaxation theory takes into account the random, time-dependent effects on the spin system caused by the environment. The theoretical framework evaluates spin relaxation in terms of the time evolution of the density operator under the influence of a Hamiltonian as expressed by the Liouville-von Neumann equation [80].

$$\frac{d\rho(t)}{dt} = \frac{-i}{\hbar} [\hat{\mathcal{H}}, \rho(t)] \quad (3.13)$$

A solution to this equation is to be obtained by a perturbation treatment. As for every theory, the perturbation theory is also based on a series of assumptions which seem to play an important role in this work (chapter 5). The first one concerns the total Hamiltonian $\hat{\mathcal{H}}$ which can be divided into three parts $\hat{\mathcal{H}} = \hat{\mathcal{H}}_I + \hat{\mathcal{H}}_L + \hat{\mathcal{H}}_{IL}$. The first two terms represent the pure spin system and pure lattice contributions, respectively, while the last one describes the coupling between them and contains parameters of both, the spin system and the lattice. In other words, the first two terms determine the energy level structure and the last one causes transitions between them. By removing the $\hat{\mathcal{H}}_I, \hat{\mathcal{H}}_L$ contributions and leaving out the perturbation spin-lattice coupling $\hat{\mathcal{H}}_{IL}$, the transformation of the density operator $\rho(t)$ and the perturbing Hamiltonian $\hat{\mathcal{H}}_{IL}$ into the interaction representation can be made:

$$\rho'(t) = e^{i\hbar\hat{\mathcal{H}}t} \rho(t) e^{-i\hbar\hat{\mathcal{H}}t} \quad (3.14)$$

$$\hat{\mathcal{H}}'_I(t) = e^{i\hbar\hat{\mathcal{H}}t} \hat{\mathcal{H}}_{IL}(t) e^{-i\hbar\hat{\mathcal{H}}t} \quad (3.15)$$

The transformation leads to the new time dependent quantities $\rho'(t)$ and $\hat{\mathcal{H}}'_{IL}(t)$, referred to as interaction representations of the operators $\rho(t)$ and

$\hat{\mathcal{H}}(t)_{IL}$, respectively. This transformation simplifies the Liouville-von Neumann equation to the form:

$$\frac{d\rho'(t)}{dt} = \frac{-i}{\hbar} [\hat{\mathcal{H}}', \rho'(t)] \quad (3.16)$$

explicitly involving the spin-lattice interaction $\hat{\mathcal{H}}'_{IL}(t)$ only.

Another assumption says that the second order perturbation theory describes the system well, called "the Redfield limit" [81, 82]. If the spin-lattice interaction fluctuates on the same timescale as the spin dynamics, the perturbation approach breaks down and it is not possible to explicitly define spin relaxation rates.

More information can be found in the following books: Purcell and Pound [78], Solomon, Bloembergen and Morgan [83], Wangsness and Bloch [84, 85], Abragam [71], Redfield [81, 82] and Kubo [86].

3.4 Nuclear Spin Hamiltonian

In this section, the Hamiltonian operators which describe some nuclear interactions like dipole coupling, chemical shielding, and quadrupole coupling will be considered.

3.4.1 Zeeman Interaction

In an NMR experiment, the applied static field \vec{B}_0 is, in general, orders of magnitude larger than any local fields arising within the sample. As a result \vec{B}_0 remains the quantization axis for the nuclear spins in the sample, and many of these local fields have negligible effects on the spin states. The spin Hamiltonian for the interaction of each spin with the static longitudinal field B_0 is given by:

$$\hat{\mathcal{H}}_j^{static} = -\gamma_j \hbar B_0 \hat{I}_{jz} \quad (3.17)$$

This is called the nuclear Zeeman interaction. The term $-\gamma_j B_0$ was already defined as the Larmor frequency at the beginning of this chapter.

3.4.2 Dipole-Dipole Coupling

As was already mentioned, each nuclear spin possesses a magnetic moment and these interact through space (called dipole-dipole or dipolar coupling). In solids, this interaction is a major cause of line broadening.

The interaction Hamiltonian for dipolar coupling between two spins I and S can be written as follows:

$$\hat{\mathcal{H}}_{DD} = - \left(\frac{\mu_0}{4\pi} \right) \gamma_I \gamma_S \hbar^2 \left(\frac{\vec{I} \vec{S}}{r^3} - 3 \frac{(\vec{I} \vec{r})(\vec{S} \vec{r})}{r^5} \right) \quad (3.18)$$

The equation is expressed in spherical polar coordinates; after expanding the scalar products, can be written:

$$\hat{\mathcal{H}}_{DD} = - \left(\frac{\mu_0}{4\pi} \right) \frac{\gamma_I \gamma_S \hbar^2}{r^3} [A + B + C + D + E + F] \quad (3.19)$$

where:

$$A = \hat{I}_z \hat{S}_z (3 \cos^2 \theta - 1) \quad (3.20)$$

$$B = -\frac{1}{4} [\hat{I}_+ \hat{S}_- + \hat{I}_- \hat{S}_+] (3 \cos^2 \theta - 1) \quad (3.21)$$

$$C = \frac{3}{2} [\hat{I}_z \hat{S}_+ + \hat{I}_+ \hat{S}_z] \sin \theta \cos \theta e^{-i\phi} \quad (3.22)$$

$$D = \frac{3}{2} [\hat{I}_z \hat{S}_- + \hat{I}_- \hat{S}_z] \sin \theta \cos \theta e^{+i\phi} \quad (3.23)$$

$$E = \frac{3}{4} [\hat{I}_+ \hat{S}_+] \sin^2 \theta e^{-2i\phi} \quad (3.24)$$

$$F = \frac{3}{4} [\hat{I}_- \hat{S}_-] \sin^2 \theta e^{+2i\phi} \quad (3.25)$$

\hat{I}_+ , \hat{S}_+ and \hat{I}_- , \hat{S}_- are the raising and lowering operators, respectively, acting on spins I and S , θ is the angle between the vector joining the two nuclei and the vector of the main magnetic field, and r is the internuclear distance.

In the dipolar Hamiltonian, the term A contains no spin-flip operators and therefore is clearly exclusively diagonal: It connects state $|1\rangle$ with state $\langle 1|$ and so on (figure 3.2). On the other hand, term B contains flip-flop operators, which flip one spin up and simultaneously flip the other one down: B connects $|3\rangle$ with $\langle 2|$ in figure 3.2. Term B has no diagonal matrix elements for the $|\alpha\beta\rangle$ representation, but it has off-diagonal elements between two states which are degenerate. The terms C and D contain spin operators, which can flip a single nuclear spin. The terms E and F contain spin operators, which can flip two nuclear spins.

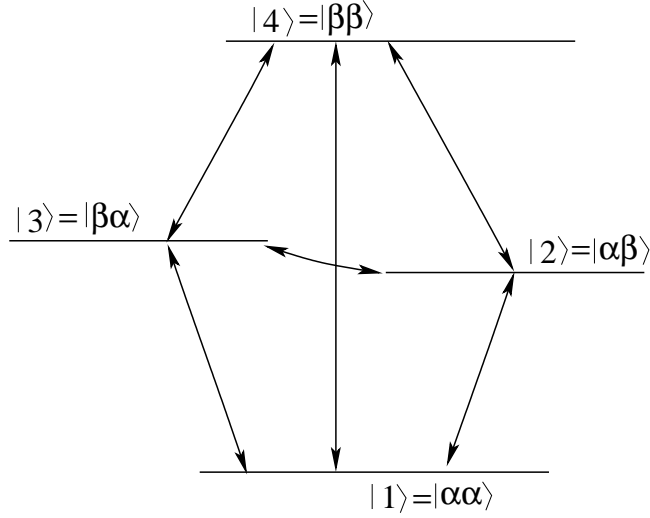


Figure 3.2: Energy levels and spin flipping in the dipolar interaction system.

3.4.3 The Chemical Shift

Electrons in the vicinity of a nucleus can produce a secondary field, which contributes, together with the main magnetic field, to the total field at the nucleus, and therefore changes the resonance frequency of the nucleus. This secondary field is a shielding field. The frequency shift caused by this field in an NMR spectrum is the chemical shift. The chemical shielding Hamiltonian acting on a spin I is

$$\hat{\mathcal{H}}_{CS} = -\gamma \hbar \hat{I} \sigma B_0 \quad (3.26)$$

B_0 is the ultimate source of the shielding magnetic field, as it is \vec{B}_0 that generates the electron current, which in turn generates the shielding magnetic field. The term σ is a second-rank tensor, called the chemical shielding tensor. The electron distribution around a nucleus in a molecule is not spherically symmetric. Therefore, the size of electron current, and hence the size of the shielding, depends on the orientation of the molecule within the applied field \vec{B}_0 . The shielding tensor describes how the size of shielding varies with molecular orientation, and it can be represented by a 3×3 matrix:

$$\sigma = \begin{pmatrix} \sigma_{xx} & \sigma_{xy} & \sigma_{xz} \\ \sigma_{yx} & \sigma_{yy} & \sigma_{yz} \\ \sigma_{zx} & \sigma_{zy} & \sigma_{zz} \end{pmatrix}$$

where x, y, z is the axis frame.

3.4.4 Quadrupolar Coupling

A distribution of charge, such as protons in a nucleus, cannot be adequately described by simply specifying the total charge. A proper characterization is required, and it can be provided by a description of the charge distribution as a series of multiples. The total charge is the zeroth-order multiple; the electric dipole moment is the first-order multiple in the expansion. The next highest term is the electric quadrupole moment, which is presented in figure 3.3. All nuclei with a spin greater than $\frac{1}{2}$ necessarily

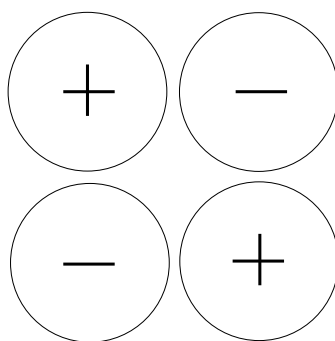


Figure 3.3: Example of the distribution of charge which gives rise to an electric quadrupole moment.

possess an electric quadrupole moment in addition to the magnetic dipole moment. Electric quadrupoles interact with electric field gradients. This interaction affects the nuclear spin energy levels in addition to the magnetic interactions already described above. The intensity of the interaction depends upon the magnitude of the nuclear quadrupole moment and the strength of the electric field gradient. The electric quadrupole moment of a nucleus is generally given as eQ (constant for a given nuclear species).

The quadrupolar Hamiltonian for a spin I (in case the interaction with the applied field B_0 outweighs the quadrupolar term) can be written:

$$\hat{\mathcal{H}}_Q = \frac{eQ}{2I(2I-1)\hbar} \mathbf{I} e \mathbf{q} \mathbf{I} \quad (3.27)$$

The tensor $e\mathbf{q}$ describes the electronic field gradient; a component $eq_{\alpha\beta}$; $\alpha\beta = x, y, z$ is the gradient of the α component of an electric field (E_x, E_y, E_z) in direction β . Two parameters, the quadrupole coupling constant χ , and the asymmetry parameter η_Q , are defined (in the electric field gradient tensor principal axis frame) in the following way:

$$\chi = \frac{eq_{zz}Q}{\hbar} \quad (3.28)$$

3.5 Correlation Functions and Spectral Densities

$$\eta_Q = \frac{q_{xx} - q_{yy}}{q_{zz}} \quad (3.29)$$

In the case where the electric field gradient tensor has axial symmetry, $q_{xx} = q_{yy} \neq q_{zz}$, the quadrupolar Hamiltonian in equation 3.27 may be expressed to first order in the applied field \vec{B}_0 as

$$\hat{\mathcal{H}}_Q = \frac{\chi}{8I(2I-1)} (3\cos^2\theta - 1) (3\hat{I}_z^2 - \hat{I}^2) \quad (3.30)$$

where θ is the angle between the principal z axis of the electric-field gradient tensor and the quantization axis of the nuclear spin, the applied field \vec{B}_0 . In the absence of axial symmetry, the equivalent expression is:

$$\hat{\mathcal{H}}_Q = \frac{\chi}{8I(2I-1)} (3\cos^2\theta - 1 - \eta_Q \sin^2\theta \cos 2\phi) (3\hat{I}_z^2 - \hat{I}^2) \quad (3.31)$$

where θ and ϕ are the polar angles defining the orientation of the applied field B_0 . The equations are suitable when the quadrupole coupling constant is much less than the Larmor frequency. In cases where the quadrupole coupling constant is approximately one tenth of the Larmor frequency or more, equations 3.30 and 3.31 are inadequate, and second-order or even higher-order terms must be included.

3.5 Correlation Functions and Spectral Densities

A fundamental quantity characterizing stochastic processes is the time correlation function. For two states $\alpha(x)$ and $\beta(x)$ of a system, which are time-dependent, a correlation function can be defined as follows:

$$\langle \alpha(\tau)\beta(\tau_0) \rangle = \int \int \alpha(x)\beta(x_0)W(x, \tau|x_0, \tau_0)W_{eq}(x_0)dx_0dx \quad (3.32)$$

The function $W(x, \tau|x_0, \tau_0)$ describes the probability that the system is in the state x at time τ if it has been in the state x_0 at time τ_0 , while W_{eq} is the equilibrium distribution of states.

The Fourier transform of the correlation function gives a spectrum of frequencies characterizing the considered motional process, and can be described by the spectral density function:

$$J(\omega) = \int_0^\infty \langle \alpha^*(\tau)\alpha(0) \rangle e^{-i\omega\tau} d\tau \quad (3.33)$$

The spectral densities determine probabilities of transitions between spin states, and as a consequence the efficiency of relaxation processes.

3.6 Examples of Relaxation Processes

In this section, some of the applications of the relaxation theory will be presented with special attention to the example of two $\frac{1}{2}$ spins.

3.6.1 Relaxation of Two Identical Spins via Dipole-Dipole Coupling

Firstly, two equivalent spins I_1 and I_2 of the spin quantum number $\frac{1}{2}$ coupled by a dipole-dipole interaction will be considered. Secondly, one assumption is made: the inter-spin vector \vec{r}_{12} , determining the principal axis of the dipole-dipole interaction, changes its orientation with respect to the direction of the external magnetic field due to rotational motion. The Hamiltonian $\hat{\mathcal{H}}$ for the entire system consists of the pure spin part $\hat{\mathcal{H}}_I$ containing Zeeman couplings of the participating spins: $\hat{\mathcal{H}}_I = \hat{\mathcal{H}}_Z(I_1) + \hat{\mathcal{H}}_Z(I_2)$, the perturbing part $\hat{\mathcal{H}}_{IL}(t) = \hat{\mathcal{H}}_{DD}(I_1, I_2)(t)$ provided by the dipole-dipole interactions fluctuating in time due to the molecular tumbling and the pure lattice part $\hat{\mathcal{H}}_L$ describing the classical continuum of rotational states of the lattice. For the sake of simplicity a different notation is used i.e., the unperturbed Hamiltonian of the spin system looks then like $\hat{\mathcal{H}}_0 = \hat{\mathcal{H}}_I = \omega_0(I_{1z} + I_{2z})$, and the perturbing, spin-lattice coupling like $\hat{\mathcal{H}}_1(t) = \hat{\mathcal{H}}_{IL}(t)$. The basis is the Eigenbasis of the main Hamiltonian $\hat{\mathcal{H}}_0$, and the dipole-dipole Hamiltonian can be represented by its matrix elements in this basis. The relaxation matrix is then obtained straightforwardly utilizing the matrix elements of the perturbing interaction $\hat{\mathcal{H}}_{DD}$ in the eigenbasis of the main Hamiltonian.

3.6.2 Relaxation of the Spin System Containing $\frac{1}{2}$ Spins due to Dipole-Dipole Coupling to Quadrupolar Spin System

The current section presents the spin-lattice relaxation of fluorine spins ($\frac{1}{2}$) caused by dipole-dipole coupling to quadrupolar spins (as an example Lu^{3+} was used).

Polarization transfer processes. Considering the system which evolves in time under the Hamiltonian $\hat{\mathcal{H}}$ composed of the Zeeman interactions and internal spin interactions, i.e. the quadrupolar coupling of the spins

S , $\hat{\mathcal{H}}_Q(S)$, and the mutual $I - S$ dipole-dipole coupling, $\hat{\mathcal{H}}_{DD}(I, S)$, the total Hamiltonian can be written as:

$$\hat{\mathcal{H}} = \hat{\mathcal{H}}_Z(I) + \hat{\mathcal{H}}_Z(S) + \hat{\mathcal{H}}_Q^0(S) + \hat{\mathcal{H}}_{DD}^0(I, S) \quad (3.34)$$

The index 'zero' in the symbols $\hat{\mathcal{H}}_Q^0(S)$ and $\hat{\mathcal{H}}_{DD}^0(I, S)$ denotes explicitly that the quadrupole and dipole couplings are fixed (do not fluctuate) with respect to the laboratory frame. The dipole-dipole interaction provides the coupling between the spins I and S (the Zeeman as well as the quadrupolar Hamiltonian represent a single spin interactions). If the coupling is weak there is no communication between the two spins and they evolve in time independently of each other. In a general case of several interactions, all contributions to the total Hamiltonian have to be considered in the same reference frame. The time evolution of an arbitrary system is dependent on its initial state reflected by the initial density operator $\rho(0)$. The initial state is established by an initial Hamiltonian $\hat{\mathcal{H}}_0^{initial}$ describing the conditions at the time $t=0$. $\hat{\mathcal{H}}_0^{initial}$ does not have to be equal to the Hamiltonian $\hat{\mathcal{H}}$, being responsible for the further time evolution of the system. If the system reaches the required initial state the conditions can be changed and then the system evolves in time under $\hat{\mathcal{H}}$, reflecting the new situation. If the applied magnetic field is high enough, the Zeeman part of the Hamiltonian determines the initial state of the spin system. In the limit of high temperature approximation, which is easily fulfilled at room temperature, the initial density operator is proportional to the linear term in the Taylor series expansion of the Boltzmann factor: $e^{-\frac{\hat{\mathcal{H}}_0^{initial}}{k_B T}} \cong 1 - \frac{\hat{\mathcal{H}}_0^{initial}}{k_B T}$ [87]. The initial density operator has in this case the following form:

$$\rho(0) = \frac{1}{(2I+1)(2S+1)} \exp\left(-\frac{\hat{\mathcal{H}}_Z^0(I) + \hat{\mathcal{H}}_Z^0(S)}{k_B T}\right) \propto I_Z + \frac{\gamma_S}{\gamma_I} S_Z \quad (3.35)$$

When the system reaches the required initial state (full polarization) the conditions can be changed by changing the magnetic field (field cycling NMR) [87]. This means that the system evolves in time under the Hamiltonian $\hat{\mathcal{H}}$ describing the new conditions.

Calculation of the evolution of the density matrix is done by obtaining the eigenstates and the corresponding eigenvalues (energy levels) for the entire system. In high magnetic field applied at the initial stage, the initial density operator does not contain any two-spin $I-S$ terms or in other words the high magnetic field makes all other couplings negligible compare to the Zeeman coupling. However this does not mean that the spins

S do not influence the evolution of the spins I . The coupling between the two spins is provided by the $I - S$ dipole-dipole interactions, influencing the eigenvectors of the entire system. The dipole-dipole part of the total Hamiltonian provides a coupling between the two sub-sets of the basis functions corresponding to the different values of the quantum number m_I , so it connects the states with $|\Delta m_I|=1$. This coupling becomes especially efficient under certain conditions. If the magnetic field is set to a value which leads to the Zeeman splitting of the dipolar spin matching the energy splitting of the quadrupolar spin, the dipole-dipole coupling causes polarization transfer processes. The mutual dipole-

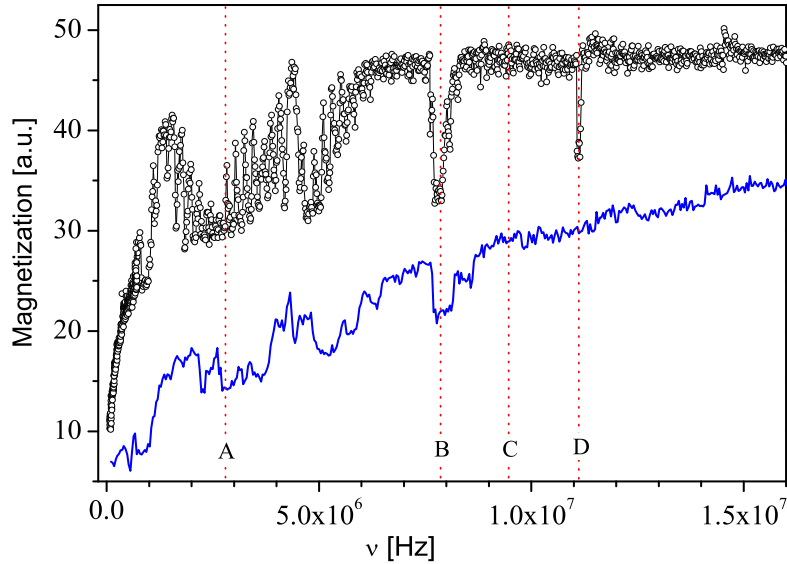


Figure 3.4: Magnetization profile of a LuF_3 -powder sample in the frequency range of from 40 kHz to 16 MHz. Typical "dips" due to polarization transfer are observable. The fluorine spins have been initially polarized in a magnetic field of 35 MHz and an evolution time of 15 ms was applied for the upper curve, open points. The lower blue curve was measured with 20 ms evolution time. Red, dashed lines demonstrate a few exemplary frequencies (A, B, C, D) for which relaxation profiles are shown in figures 3.5, 3.6, 3.7, 3.8.

dipole coupling links transitions of the dipolar spin to some transitions of the quadrupolar spin, so they cannot occur independently. However

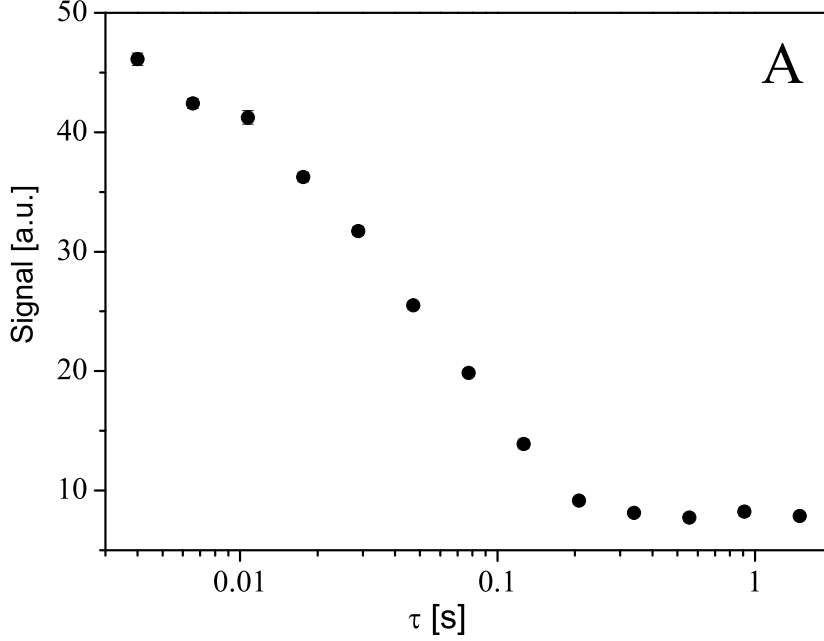


Figure 3.5: T_1 relaxation profile obtained by the field cycling technique. The sample was polarized in a magnetic field of 35 MHz. Afterwards the magnetic field was changed to the evolution field of $\nu = 2733046$ Hz (position "A" in figure 3.4). The duration, τ , of the evolution field was varied in the time range of from 4 ms to 1.5 s. The detection field following the evolution field was set to 40 MHz (cp. fig. 4.10).

the entire system conserves the total energy. The polarization of the dipolar spins is transferred to the quadrupolar subsystem with the efficiency directly related to the probability of the joint transitions. The probability is determined by the square of the corresponding matrix element of the dipole-dipole Hamiltonian $|\langle r | \hat{\mathcal{H}}_{DD}(I, S) | s \rangle|^2$.

Experimental illustration of the polarization transfer processes occurring in LuF_3 with the lutetium quadrupole spin $S = 7/2$. Figure 3.4 presents fluorine spin magnetization detected versus the magnetic field. The fluorine spins have been initially polarized in a magnetic field of 35 MHz. Afterwards the field has been switched to a much lower value. The entire spin system has been evolving over a certain time period (called the evolution time) under the Hamiltonian containing the quadrupole coupling of the lutetium spins and the Zeeman couplings of the fluorine as

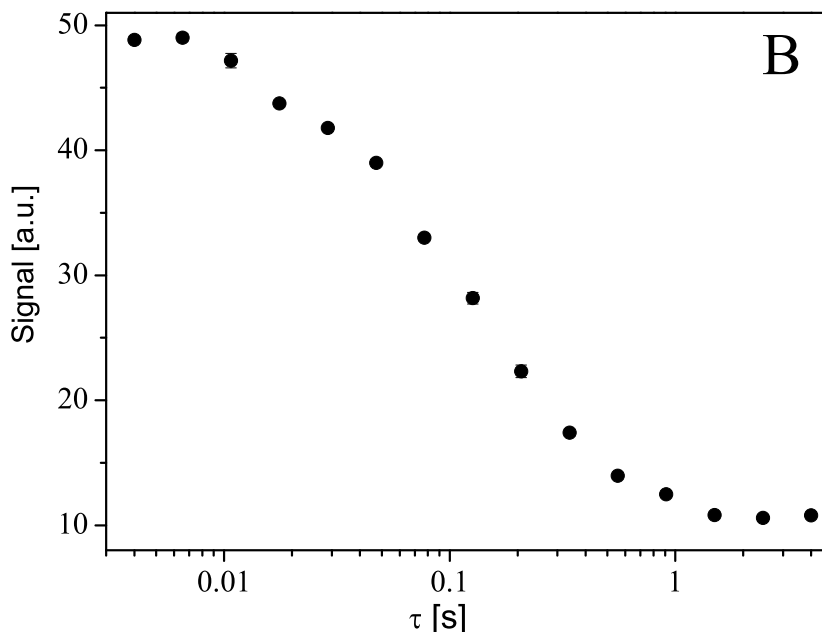


Figure 3.6: T_1 relaxation profile obtained by the field cycling technique. The sample was polarized in a magnetic field of 35 MHz. Afterwards the magnetic field was changed to the evolution field of $\nu = 7795013$ Hz (position "B" in figure 3.4). The duration, τ , of the evolution field was varied in the time range of from 4 ms to 4 s. The detection field following the evolution field was set to 40 MHz (cp. fig. 4.10).

well as the lutetium spins corresponding to the adjusted lower value of the magnetic field. The fluorine magnetization has been then monitored at a magnetic field corresponding to a resonance frequency of 40 MHz by measuring the amplitude of the FID signal. The data presented in figure 3.4 have been obtained for two evolution times, 15 ms (open circles) and 20 ms (blue curve). It can be seen that most of the polarization transfer dips exist at the same frequencies, except for the one around 11 MHz which is visible only for the upper curve (evolution time 15 ms). The control measurement performed later for the evolution time 20 ms did not show any indication around this frequency. The reason for this discrepancy is not clear, it could be caused by technical problems of the spectrometer. Also the T_1 relaxation profile for the frequency 11620757 Hz presented in figure 3.8 shows no indication of the polarisation transfer process. If the

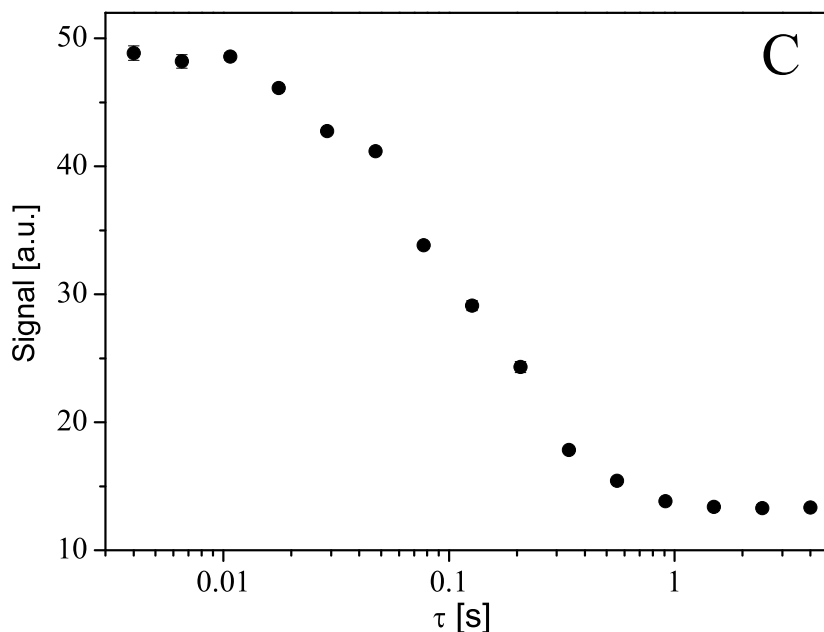


Figure 3.7: T_1 relaxation profile obtained by the field cycling technique. The sample was polarized in a magnetic field of 35 MHz. Afterwards the magnetic field was changed to the evolution field of $\nu = 9495646$ Hz (position "C" in figure 3.4). The duration, τ , of the evolution field was varied in the time range of from 4 ms to 4 s. The detection field following the evolution field was set to 40 MHz (cp. fig. 4.10).

experimental conditions are appropriate, it should be observable as an additional decay on the top of the T_1 relaxation profiles. An indication for this extra decay at the beginning of the profiles can be observed inside the "dips" (figures 3.5, 3.6; marks "A" and "B" in figure 3.4). To clarify this hint more detailed study should be performed. However, because of the technical limitations it was not possible to measure signals at times shorter than 4 ms.

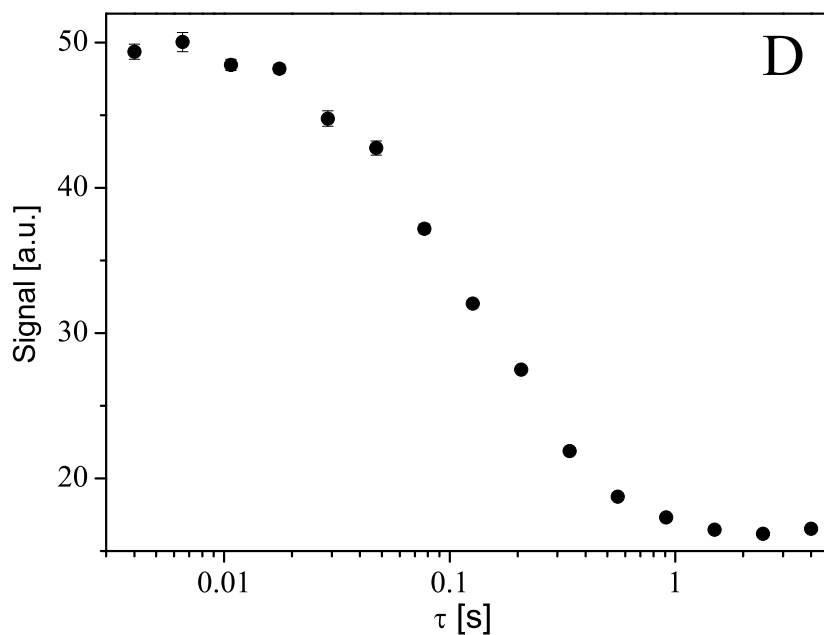


Figure 3.8: T_1 relaxation profile obtained by the field cycling technique. The sample was polarized in a magnetic field of 35 MHz. Afterwards the magnetic field was changed to the evolution field of $\nu = 11620757$ Hz (position "D" in figure 3.4). The duration, τ , of the evolution field was varied in the time range of from 4 ms to 4 s. The detection field following the evolution field was set to 40 MHz (cp. fig. 4.10).

Chapter 4

Experimental Techniques

This chapter presents all experimental techniques and problems faced during the measurements. More detailed discussion about used methods can be found in a large number of literature references [75, 76, 94, 95].

4.1 NMR-Lineshape

Experimental NMR fluorine spectra have been collected for a pure BaF_2 single crystal and five doped crystals, $\text{Ba}_{1-x}\text{La}_x\text{F}_{2+x}$, with $x = 0.0005, 0.001, 0.01, 0.03, 0.1$.

The experimental data for each sample consist of a series of about 20 spectra, collected from room temperature up to 1200 K. The upper temperature limit depends on the admixture concentrations and is given by the experimental line width approaching the resolution limit of the spectrometer (500 Hz). For the measurements single crystals of approximately $4 \times 4 \times 8 \text{ mm}^3$ size were used. Their crystallographic orientation with respect to the (100)-plane was checked using Laue diffraction. The samples were sealed in quartz tubes under vacuum. Since the fluorine dynamics in all samples can change irreversibly after heating [8], all crystals were heated several times until no further aging could be observed.

Experimental setup The experimental setup is shown in figure 4.1 and consists of a TecMag Apollo Console, an ATM High-Power Amplifier, a Temperature Controller and a PC.

Apollo Console The Apollo spectrometer is a digital NMR spectrometer console manufactured by TecMag. It is equipped with two RF channels

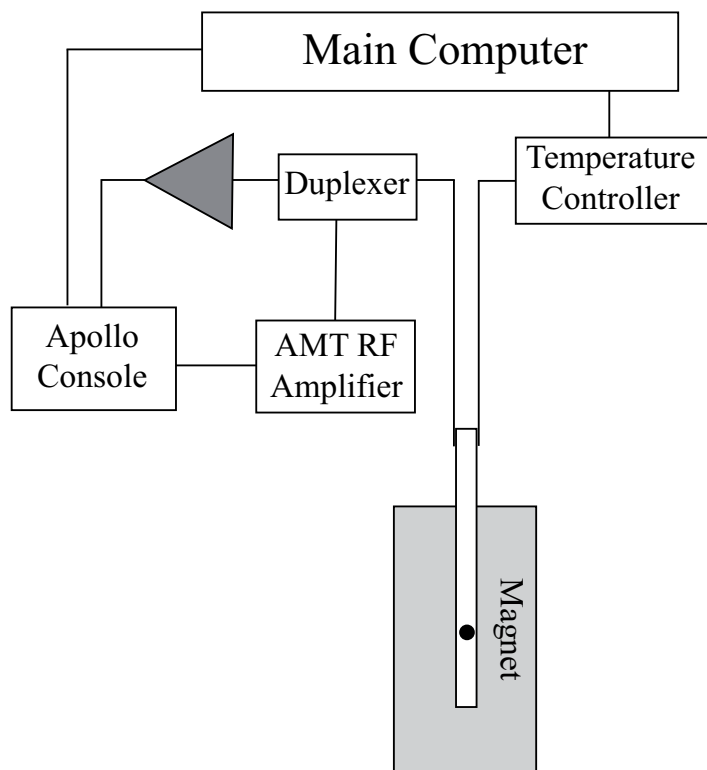


Figure 4.1: A schematic representation of the lineshape spectrometer.

and an integrated pulse programmer. The NTNMR controlling software is Windows NT based and an important feature is OLE control that enabled us to write Visual Basic control programs to provide a high level of automation and control. A schematic diagram is shown above to illustrate the operation of the RF transmitter. Here brief explanation of the function of each component marked in figure 4.2 is given. The RF synthesizer (1) produces an oscillating electrical signal with a well-defined frequency which is the spectrometer reference frequency, denoted ω_{ref} . The synthesizer output wave is given as $S_{synt} \sim \cos(\omega_{ref}t + \phi(t))$ where $\phi(t)$ is the RF phase controlled by the pulse programmer (3). The pulse gate (4) is a fast switch closed at defined moment to allow the RF reference wave to pass through. The effect is to create an RF pulse with finite duration. The duration of the RF pulse is referred to as the pulse width, determined

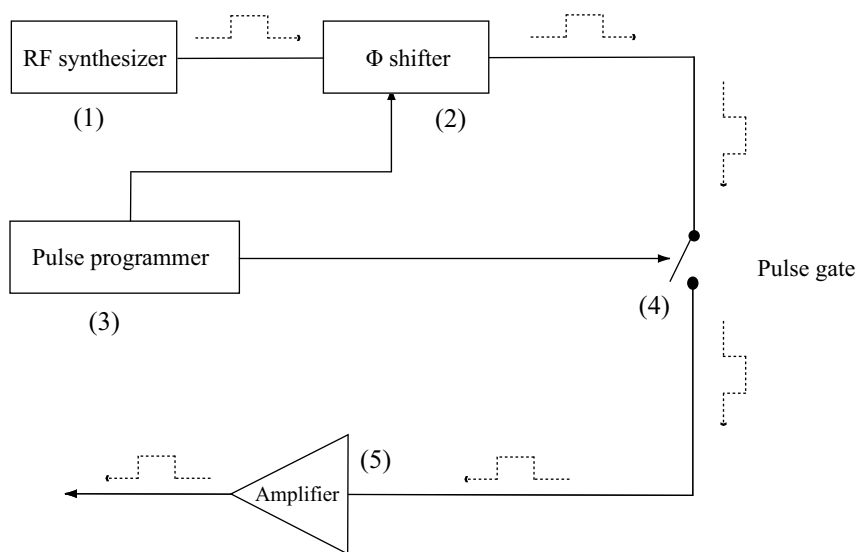


Figure 4.2: A schematic diagram of the RF transmitter.

by the pulse gate (4) and the pulse programmer (3). The RF amplifier (5) is to scale up the gated wave to produce a large-amplitude RF pulse for transmission to the probe.

The Apollo spectrometer is controlled by the NTNMR software through two PCI cards, one is used to upload data to the main computer during and after data acquisition, the other one is responsible for all other communication between the main computer and the Apollo system, such as uploading pulse program data from the main computer to the system interface board.

4.1.1 Signal Processing

A schematic of the receiver section, key to signal processing is presented in figure 4.3. Some components ((1), (8) and ADCs) are built-in the Apollo console. The NMR signal arrives at the duplexer (6) and is diverted towards the signal preamplifier (7) which is a low-noise R.F. amplifier which scales up the weak signal to a more convenient voltage level. This signal is a continuous current or voltage which must be converted into digital form for further interpretation and presentation on a computer. But the original NMR signal oscillates at very high frequency, tens or hundreds of MHz, which is too fast for the ADCs (analogue-to-digital conversion). The quadrature receiver (8) is designed to generate a new frequency signal which is oscillating at the relative Larmor frequency (much

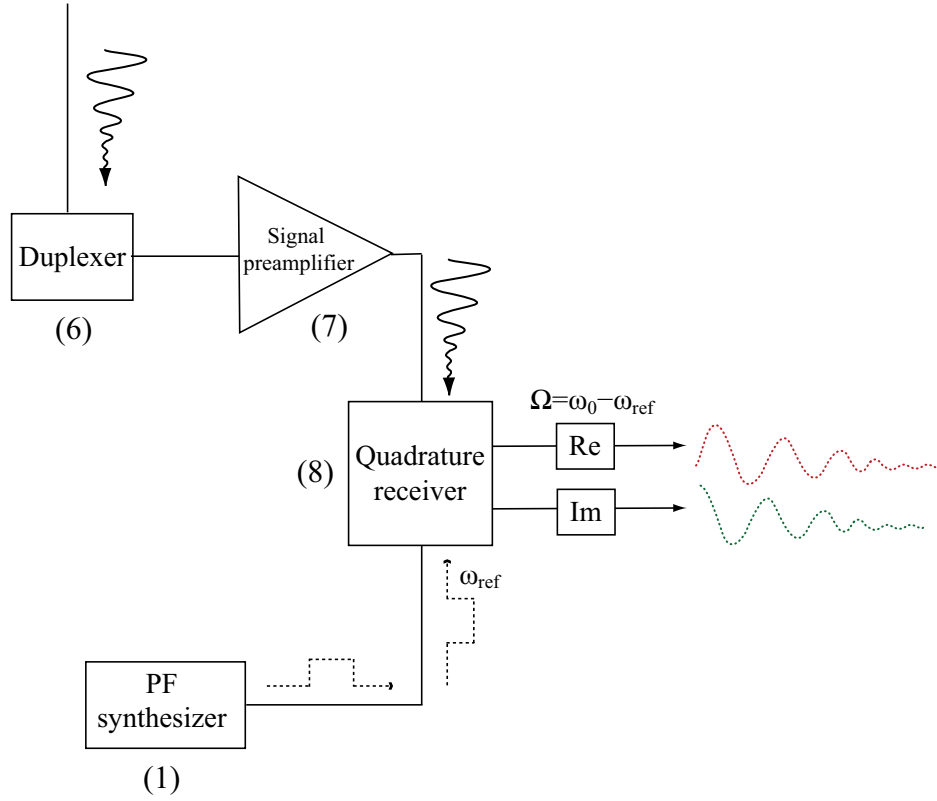


Figure 4.3: A schematic diagram of the receiver section.

slower than original signal) by mixing the NMR signal, which oscillates at the Larmor frequency ω_0 , with the reference signal, oscillating at the frequency ω_{ref} . The relative Larmor frequency is $\Delta\omega = \omega_0 - \omega_{ref}$. The offset frequency $\frac{\Delta\omega}{2\pi}$ is usually of the order of 1MHz or less, enabling the signal to be handled accurately by ADCs. Now the output of the receiver is $S(t) \sim \cos(\Delta\omega t) \exp(\frac{-t}{T_2})$ and the signal can be handled using the NTNMR software which offers numerous functions. Examples which were applied during processing are presented below.

- a baseline correction was performed to eliminate dc offset
- a left shift was applied to eliminate any remaining dead time signal
- an exponential multiplication was performed on the FID data set with a function defined by $f(t) = \exp(-t \text{ value})$, where the value parameter was set to 100Hz.

- once the signal in the time domain had been optimized, a Fourier transform was then applied to transform the signal from time domain to frequency domain, and produce the NMR spectrum
- the crucial part of the signal processing, namely phase correction and integration, was then performed. We compared the left and right wing of the dispersion spectrum and adjusted the phase until the absorption spectrum was symmetrical.

More about that can be found in the literature [98].

Missing points and linear prediction. Recording the free induction decay (FID) signal, using one $\frac{\pi}{2}$ -pulse has the disadvantage of losing a few points at the beginning of the signal because of the dead-time effect (t_d , figure 4.4), as mentioned above. This can be avoided by applying a different pulse sequence, for example, the Hahn or Solid Echo and recording echo-signals. Unfortunately, in the case of highly doped samples $\text{Ba}_{1-x}\text{La}_x\text{F}_{2+x}$, $x = 0.01, 0.03, 0.1$ it is impossible to reproduce both the chemical-shift and dipole-dipole- interactions with this kind of pulse sequence. The pulse sequence presented below, therefore, was used to recover the data. To correct

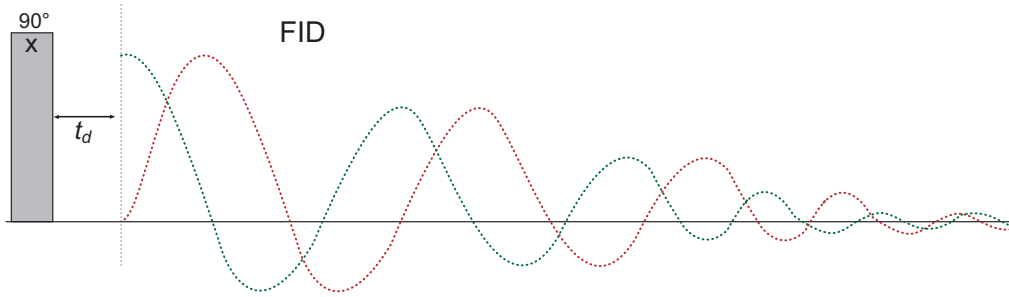


Figure 4.4: The one-pulse sequence.

corrupted data points at the beginning of the FID signal a linear prediction algorithm [99] was applied to do backward extrapolation of the recorded time signal. To give a better understanding of the linear prediction, the basic concept behind this term is presented below.

Considering a complex causal signal $S(t)$ containing a single damped exponential:

$$S(t) = Ae^{-Rt}e^{-j2\pi\omega_0 t} \quad (4.1)$$

where A is a complex amplitude, R the damping coefficient, and ω_0 the frequency of the sinusoid. Sampling $S(t)$ at constant time interval Δ yields

the time series $\{S_k\}$:

$$S_k = S(k\Delta) = Ae^{-Rt\Delta}e^{-j2\pi\omega_0k\Delta} = AZ^k \quad (4.2)$$

where Z is a constant with respect to k , and equal to: $Z = e^{-(R+j2\pi\omega_0)\Delta}$. Using basic properties of exponential functions, one can directly derive from equation 4.2 that: $S_k = ZS_{k-1}$, $\forall k > 0$ i.e. the data points in the time series are linearly related. In this simple case, knowledge of two consecutive data points S_i and S_{i+1} is enough to fully characterize the time series, by first computing $Z = \frac{S_{i+1}}{S_i}$. Detailed information are provided in the article of P. Koehl [99].

4.1.2 Magic-Angle Spinning

In the next two sections some methods to measure lineshape with the possibility of removing the "broadening parts" in the main Hamiltonian will be presented. One of them is magic-angle spinning (MAS) which is used routinely in the vast majority of solid state NMR experiments. Its primary task is to get rid of the effects of chemical shift anisotropy and to assist in the removal of heteronuclear dipolar-coupling effects. In solution NMR spectra, effects of chemical shift anisotropy and dipolar coupling are rarely observed. This is because the rapid tumbling of the molecules in a solution means that the angle θ (figure 4.5) describing the orientation of the shielding tensor with respect to the applied field \vec{B}_0 is rapidly averaged over all possible values. This averages the $(3\cos^2\theta - 1)$ dependence of the transition frequencies to zero on the NMR timescale. The aim of magic angle spinning is to achieve the same result for solids. It averages the anisotropy associated with any interaction which causes a shift in the energies of the Zeeman spin functions, such as chemical shift anisotropy, heteronuclear dipolar coupling, but no mixing between Zeeman functions (to first order). However, it also has an effect on secular interactions which mix Zeeman functions, i.e. homonuclear dipolar coupling.

Spinning sidebands In order for magic angle spinning to reduce a powder pattern to a single line at the isotropic chemical shift, the rate of the sample spinning must be fast in comparison to the anisotropy of the interaction being spun out. Fast in this context means around a factor of 3 or 4 greater than the anisotropy. Slower spinning produces a set of spinning sidebands in addition to the line at the isotropic chemical shift (figure 4.6). The spinning sidebands are sharp lines separated by the frequency of the spinning and radiate out from the line at isotropic chemical shift. It

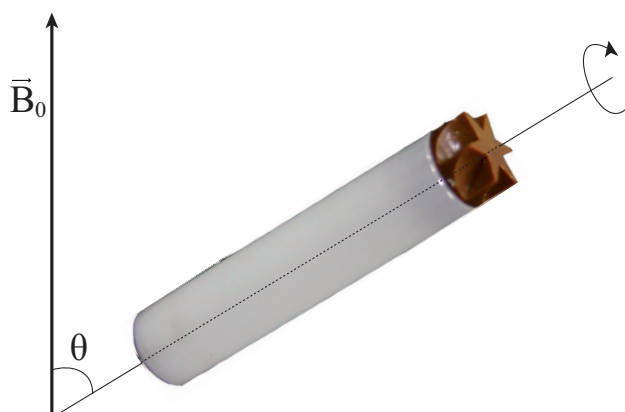


Figure 4.5: A scheme of the MAS experiment. The sample is spun rapidly in a cylindrical rotor about a spinning axis oriented at the magic angle $\theta=54.74^\circ$ with respect to the applied magnetic field \vec{B}_0 .

can happen that the line at the isotropic chemical shift is not necessarily the most intense line. The only characteristic feature of the isotropic chemical shift line is that it is the only line that does not change position with spinning speed. This is the only reliable feature to identify it. More detailed mathematical analysis of spinning sidebands can be found in the literature [77].

Spinning sidebands can be also found in the time signal, where they are called rotational echoes. These are simply explained as follows. Consider a component of magnetization in the $x - y$ plane of the rotating frame; the evolution of this magnetization is what is recorded in the FID. This magnetization has an evolution frequency determined by the applied field B_0 and chemical shielding. Suppose this component arises from a principal axis frame of orientation (α, β, γ) with respect to the rotor axis frame and that the whole sample is spun at the magic angle. As the sample spins, the evolution frequency is varied, because the crystalline orientation changes with respect to the B_0 field, and so the chemical shielding changes too. However, when the sample returns to its starting position, the evolution frequency returns to its starting value and then goes through the same cycle of values again. Thus, the FID corresponding to the magnetization component consists of a sequence of repeated sub-FIDs or rotational echoes (figure 4.7).

Magic-angle spinning for homonuclear dipolar couplings As mentioned at the beginning of this section, magic-angle spinning can be used

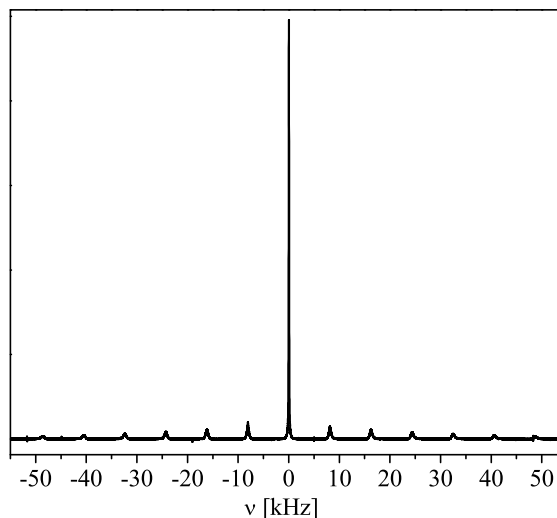


Figure 4.6: The effect of slow speed magic-angle spinning. A set of spinning sidebands appears, with a center-band at the isotropic chemical shift and further lines spaced at the spinning frequency.

for removing the effects of homonuclear dipolar-coupling providing the spinning speed is high enough. The dipolar-coupling Hamiltonian for a homonuclear-coupled spin pair, I and S can be written as:

$$\mathcal{H}_{DD}^{homo} = -C \frac{1}{2} (3\cos^2\theta - 1) [3\hat{I}_z\hat{S}_z - \hat{\mathbf{I}} \cdot \hat{\mathbf{S}}] \quad (4.3)$$

with $C = (\frac{\mu_0}{4\pi}) \frac{\gamma_I \gamma_S \hbar}{r^3}$, the dipolar-coupling constant. From equation 4.3, the homonuclear dipolar coupling quite clearly depends on the geometric factor $(3\cos^2\theta - 1)$, and so is averaged to zero by magic-angle spinning, if the rate of spinning is fast compared to the homonuclear dipolar-coupling line width. At spinning speeds much less than the dipolar line width, magic angle spinning has very little effect on the NMR spectrum (figure 5.21). At intermediate spinning rates (rates around a quarter to a half of the dipolar line width), spinning sidebands appear, but these spinning sidebands are different in character to those arising from incompletely spun-out chemical shift anisotropy or heteronuclear dipolar coupling, as it was mentioned above. The spinning sidebands associated with chemical shift anisotropy and heteronuclear dipolar coupling are all sharp lines. Those associated with homonuclear dipolar coupling are usually broad. This can be under-

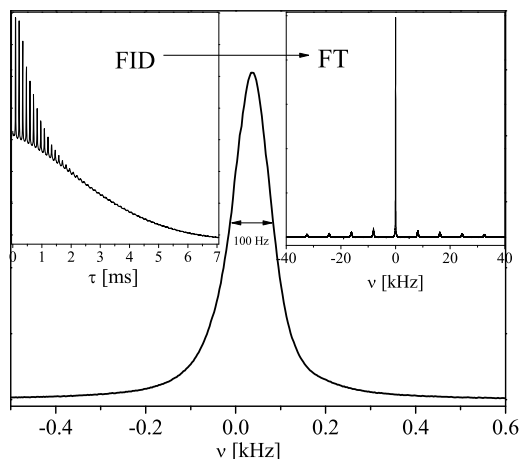


Figure 4.7: The formation of rotational echoes. Fourier transformation of the entire FID gives a line at the isotropic chemical shift flanked by spinning sidebands as described in the text.

stood as follows. The term B in the homonuclear dipolar-coupling Hamiltonian mixes the degenerate Zeeman functions associated with the collection of spins in the spin system. As shown in chapter 1, this mixing is time-dependent if there are more than two spins in the system so that the wave functions describing the spin system are time-dependent linear combinations of the Zeeman functions. To average an interaction to zero through magic-angle spinning, the state of the spin system needs to be constant over the time for one period of the sample rotation. However, in the case of homonuclear dipolar coupling, the state of the spin system is changing on the timescale of the sample rotation, for intermediate sample rotation rates. This prevents the complete averaging of the dipolar interaction in the spin system. At lower spinning rates, however, the rate at which the state of the system changes is rapid compared to the sample spinning. In this case, the spinning does not have a chance to alter the time-dependent state of the spin system, hence the NMR spectrum of the system is unaffected by the spinning. This does not happen in heteronuclear spin systems, as there are no degenerate spin levels in such a system.

4.1.3 Multiple-Pulse Sequences

The simplest multiple-pulse experiment is the two-pulse Hahn echo [104] which has been invented in the early days of NMR. Later new and more complicated multiple pulse sequences were developed. As it was mentioned in the previous subsection, MAS NMR can be used to remove the effects of dipolar coupling from spectra, providing the rate of sample spinning is fast relative to the homonuclear dipolar line width. Another alternative which also works with bulk samples is a sequence of special pulses. Most multiple pulse sequences are arranged in such a way that,

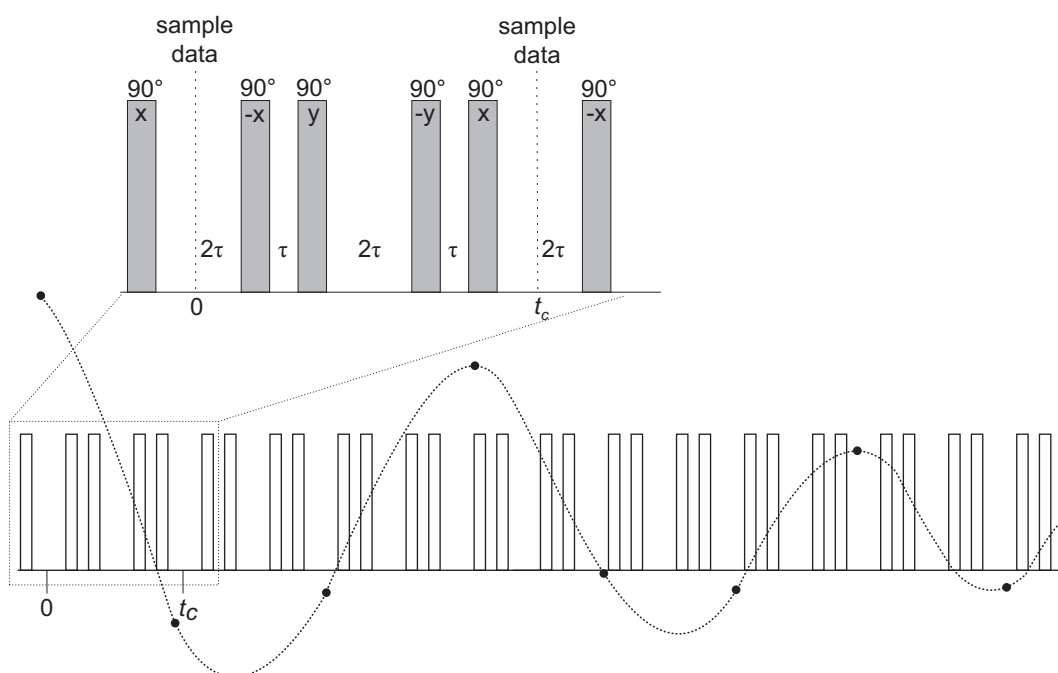


Figure 4.8: Multiple pulse sequence for removing the effects of homonuclear dipolar coupling from the NMR spectrum. All pulses are 90° pulses with the phase indicated; WHH-4 sequence.

at certain windows within the pulses sequence, the effect of the dipolar Hamiltonian on the nuclear magnetization is zero. If the nuclear magnetization is detected only at these points, the effects of dipolar coupling are removed from the spectrum. There are many useful sequences in the literature [77, 100]. The first, and one of the simplest, is the WHH-4, shown in figure 4.8 [100]. The MREV-8 sequence [77] which is twice as long as WHH-4 also has wide applicability. In both sequences, the pulsing continues in cycles throughout the period of the free induction decay, with one

detection point per cycle at the appropriate point until the magnetization has decayed completely from the x-y plane. Rather than averaging the geometrical parts of $\hat{\mathcal{H}}_{dd}^{homo}$ to zero in the way that magic-angle spinning does, these pulse sequences average the spin factors of $\hat{\mathcal{H}}_{dd}^{homo}$ to zero. To have a better understanding of these processes some important points of average Hamiltonian theory are presented here. The density operator describing a spin system at time t , $\hat{\rho}(t)$ from that at time 0 can be calculated from the equation:

$$\hat{\rho}(t) = \hat{U}(t)\hat{\rho}(0)\hat{U}(t)^{-1} \quad (4.4)$$

where the so-called propagator $\hat{U}(t)$ is given by

$$\hat{U}(t) = \exp(-i\hat{\mathcal{H}}t) \quad (4.5)$$

in which $\hat{\mathcal{H}}$ is the Hamiltonian operator which describes the spin system between 0 and t . This formulation of the propagator assumes that the Hamiltonian is constant over the time period. Frequently, however, this is not the case. For example, in the already mentioned WHH-4 sequence, the Hamiltonian changes when RF pulses are applied. In these circumstances, equation 4.5 for the propagator becomes

$$\hat{U}(t) = \exp(-i\hat{\mathcal{H}}_n t_n) \dots \exp(-i\hat{\mathcal{H}}_1 t_1) \quad (4.6)$$

where the Hamiltonian which operates in the first time period t_1 is $\hat{\mathcal{H}}_1$ and so on. If the Hamiltonians in equation 4.6 appear in strict chronological order, one can replace the series of exponential functions in this equation by the propagator with a single exponential relying on some average Hamiltonian $\bar{\mathcal{H}}$ which has the same effect as the series of Hamiltonian $\hat{\mathcal{H}}_1 \dots \hat{\mathcal{H}}_n$, i.e.

$$\hat{U}(t) = \exp(-i\hat{\mathcal{H}}_n t_n) \dots \exp(-i\hat{\mathcal{H}}_1 t_1) = \exp(-i\bar{\mathcal{H}}t) \quad (4.7)$$

Of course, this is always possible, but unfortunately not, always useful, as in general, the appropriate average Hamiltonian $\bar{\mathcal{H}}$ will depend on t . The calculation of a single average Hamiltonian which will describe the behavior of the spin system at this time can be made.

One way of doing that is to calculate the propagator $\hat{U}(t)$ by simply evaluating the series of exponents in equation 4.7 appropriate to the particular periodic Hamiltonian of interest. This then equates to $\exp(-i\bar{\mathcal{H}}t)$, so that $\bar{\mathcal{H}}$ may be found by diagonalizing the matrix Ut formed from $\hat{U}(t)$ in some appropriate basis. The eigenvalues resulting from this process are then $\exp(-i\mathcal{H}_{jj}t)$ for the j th eigenvalue, where \mathcal{H}_{jj} is the matrix element of \bar{H} in the eigenvector basis arising from the diagonalization. This

Experimental Techniques

process is rather complicated and a simple solution can be used. This alternative approach evaluates the series of exponential operators in equation 4.8 using the Magnus expansion:

$$e^{\hat{A}}e^{\hat{B}} = \exp\{\hat{A} + \hat{B} + \frac{1}{2!}[\hat{A}, \hat{B}] + \frac{1}{3!}([\hat{A}, [\hat{A}, \hat{B}]] + [[\hat{A}, \hat{B}], \hat{B}]) + \dots\} \quad (4.8)$$

If this is applied to equation 4.7 for a periodic Hamiltonian of period t_p i.e. $t_1 + t_2 \dots + t_n = t_p$ to evaluate $\hat{U}(t_p)$ one gets

$$\hat{U}(t_p) = \exp(-i\bar{\mathcal{H}}t_p) \quad (4.9)$$

$$\hat{\mathcal{H}}(t_p) = \hat{\mathcal{H}}^0 + \hat{\mathcal{H}}^1 + \hat{\mathcal{H}}^2 \dots \quad (4.10)$$

where

$$\hat{\mathcal{H}}^0 = \frac{1}{t_p} \{\hat{\mathcal{H}}_1 t_1 + \hat{\mathcal{H}}_2 t_2 \dots + \hat{\mathcal{H}}_n t_n\} \quad (4.11)$$

$$\hat{\mathcal{H}}^1 = -\frac{i}{2t_p} \{[\hat{\mathcal{H}}_2 t_2, \hat{\mathcal{H}}_1 t_1] + [\hat{\mathcal{H}}_3 t_3, \hat{\mathcal{H}}_1 t_1] + [\hat{\mathcal{H}}_2 t_2, \hat{\mathcal{H}}_3 t_3] + \dots\} \quad (4.12)$$

$$\begin{aligned} \hat{\mathcal{H}}^2 = & -\frac{1}{6t_p} \{[\hat{\mathcal{H}}_3 t_3, [\hat{\mathcal{H}}_2 t_2, \hat{\mathcal{H}}_1 t_1]] + [[\hat{\mathcal{H}}_3 t_3, \hat{\mathcal{H}}_2 t_2], \hat{\mathcal{H}}_1 t_1] \\ & + \frac{1}{2}[\hat{\mathcal{H}}_2 t_2, [\hat{\mathcal{H}}_2 t_2, \hat{\mathcal{H}}_1 t_1]] + \frac{1}{2}[[\hat{\mathcal{H}}_2 t_2, \hat{\mathcal{H}}_1 t_1], \hat{\mathcal{H}}_1 t_1] + \dots\} \end{aligned} \quad (4.13)$$

Equations 4.12 and 4.13 are not as daunting as they at first appear; the first-order term $\hat{\mathcal{H}}^0$ is simply the average of the piecewise Hamiltonians $\hat{\mathcal{H}}_1, \hat{\mathcal{H}}_2 \dots \hat{\mathcal{H}}_n$ which operates during one period. In the case where these Hamiltonians all commute with each other, or nearly so, all higher-order terms can be neglected and the first-order term is a good description of the average Hamiltonian. Clearly if this is the case, the analytic form of the approximate average Hamiltonian is easily determined and one can tell up to certain point how a pulse sequence works.

In cases where the Hamiltonians which operate over the time period do not commute with each other it is often possible to transform them into a new frame, the so-called toggling frame. In this frame the non-commuting terms disappear. To have a better understanding how the Hamiltonians look in the toggling frame, one has to assume that all the WHH-4 pulses are of negligible length compared to t , the gaps between them, and are strong compared to the dipolar coupling, so strong that there is no coupling during the pulse. Another assumption is that the pulses are all on resonance and are defined with respect to the rotating frame, so that

throughout the pulse sequence, the effect of the B_0 field apparently vanishes. This means the Zeeman term in the total Hamiltonian is zero. Then the Hamiltonian for the system during a pulse is

$$\hat{\mathcal{H}}_{pulse}^{\phi} = -\omega_1(\hat{I}_x \cos\phi + \hat{I}_y \sin\phi) \quad (4.14)$$

where ϕ is the phase of the pulse and

$$\hat{I}_x = \sum_i \hat{I}_x^i \quad \text{and} \quad \hat{I}_y = \sum_i \hat{I}_y^i \quad (4.15)$$

with \hat{I}_x^i, \hat{I}_y^i being the single spin operators. The Hamiltonian during the periods of free evolution is simply that of the homonuclear dipolar coupling, in the absence of other interactions, namely

$$\hat{\mathcal{H}}_{homo} = \sum_{i>j} B_{ij}(3\hat{I}_z^i \hat{I}_z^j - \hat{\mathbf{I}}^i \cdot \hat{\mathbf{I}}^j) \quad (4.16)$$

where

$$B_{ij} = -\left(\frac{\mu_0}{4\pi}\right) \frac{\gamma_j \gamma_i}{r_{ij}^3} \hbar \frac{1}{2} (3\cos^2\Theta - 1) \quad (4.17)$$

In all these Hamiltonians, x, y and z refer to the rotating frame axes. Now, the Hamiltonians describing the pulses and those describing the periods of free precession do not commute with each other, so the first-order term in the average Hamiltonian is not a good approximation to the full average Hamiltonian, as it was mentioned above. In particular, the pulse Hamiltonians are a problem, as they do not commute among each other, that is, \hat{I}_x in an x -pulse operator does not commute with \hat{I}_y in a y -pulse operator, and the WHH-4 sequence employs both x and y pulses. To get rid of these problems the transformation to a new frame, where the terms in the Hamiltonian due to the pulses disappear, is needed. The average Hamiltonian in this new frame is then simply the first-order term of equation (4.8).

In order to find this new frame one can consider a situation, in the rotating frame, of an on-resonance x pulse with no other interactions present and simply write the Hamiltonian

$$\hat{\mathcal{H}} = \hat{\mathcal{H}}_{pulse}^x = -\omega_1 \hat{I}_x \quad (4.18)$$

The density operator after time t is given by the usual expression:

$$\hat{\rho}(t) = \exp(-i\hat{\mathcal{H}}t)\hat{\rho}(0)\exp(i\hat{\mathcal{H}}t) = \exp(i\omega_1 \hat{I}_x t)\hat{\rho}(0)\exp(-i\omega_1 \hat{I}_x t) \quad (4.19)$$

Experimental Techniques

So the effect of the on-resonance x pulse is to rotate the density operator by $+\omega_1 t$ about x , or, equivalently, to rotate the axis frame so the density operator $\hat{\rho}$ is defined by $-\omega_1 t$ about x , where x in every case refers to the normal, rotating frame axis. Thus, when considering the effect of a pulse sequence we will rotate the axis frame in which the density operator is defined. A rotation of the axis frame by $-\omega_1 t$ about the pulse axis creates the same effect as rotating the density operator by $+\omega_1 t$ about the pulse axis. The new, transformed frame is usually called the toggling frame. The Hamiltonian $\hat{\mathcal{H}}^*(t)$ after a time t in such a toggling frame is in general

$$\hat{\mathcal{H}}^*(t) = \hat{R}_x^{-1} \hat{\mathcal{H}} \hat{R}_x + \omega_1 \hat{I}_x \quad (4.20)$$

where $\hat{R}_x = \exp(-i\omega_1 \hat{I}_x t)$ represents the rotation operator for rotation of the original axis frame by $\omega_1 t$ about the rotating frame x axis, and $\hat{\mathcal{H}}$ is the Hamiltonian in the rotating frame.

So, in the case where $\hat{\mathcal{H}} = \hat{\mathcal{H}}_{pulse}^x = -\omega_1 \hat{I}_x$, the toggling frame Hamiltonian can be written as:

$$\hat{\mathcal{H}}^*(t) = -\omega_1 \hat{R}_x^{-1} \hat{I}_x \hat{R}_x + \omega_1 \hat{I}_x; \quad \hat{R}_x = \exp(-i\omega_1 \hat{I}_x t) \quad (4.21)$$

The first term represents a rotation of the operator \hat{I}_x about x , which of course leaves the x direction, and so \hat{I}_x , unchanged. Thus $\hat{\mathcal{H}}^*(t)$ becomes

$$\hat{\mathcal{H}}^*(t) = -\omega_1 \hat{I}_x + \omega_1 \hat{I}_x = 0 \quad (4.22)$$

As expected, in this toggling frame the effect of the RF pulse is nulled. The same frame transformation on the density operator takes account of the pulse effects. Some general Hamiltonian in the rotating frame can be written as

$$\hat{\mathcal{H}} = \hat{\mathcal{H}}_{int} + \hat{\mathcal{H}}_{pulse}^x \quad (4.23)$$

where $\hat{\mathcal{H}}_{int}$ describes some spin interaction and $\hat{\mathcal{H}}_{pulse}^x$ describes an x pulse. Transforming this Hamiltonian to the toggling frame using equation (3.20):

$$\begin{aligned} \hat{\mathcal{H}}^*(t) &= \hat{R}_x^{-1} \hat{\mathcal{H}} \hat{R}_x + \omega_1 \hat{I}_x \\ &= \hat{R}_x^{-1} (\hat{\mathcal{H}}_{int} + \hat{\mathcal{H}}_{pulse}^x) \hat{R}_x + \omega_1 \hat{I}_x \\ &= \hat{R}_x^{-1} \hat{\mathcal{H}}_{int} \hat{R}_x + \hat{R}_x^{-1} \hat{\mathcal{H}}_{pulse}^x \hat{R}_x + \omega_1 \hat{I}_x \\ &= \hat{R}_x^{-1} \hat{\mathcal{H}}_{int} \hat{R}_x \end{aligned} \quad (4.24)$$

since

$$\hat{R}_x^{-1} \hat{\mathcal{H}}_{pulse}^x \hat{R}_x = -\omega_1 \exp(i\omega_1 \hat{I}_x t) \hat{I}_x \exp(-i\omega_1 \hat{I}_x t) = \omega_1 \hat{I}_x \quad (4.25)$$

as before. In other words, the toggling frame Hamiltonian depends only on the spin interaction Hamiltonian $\hat{\mathcal{H}}_{int}$ and not on the pulse part. $\hat{\mathcal{H}}^*$ can then be used to calculate ρ^* , the toggling frame density operator, using an equivalent expression to that in equation (3.19):

$$\hat{\rho}^*(t) = \exp(-i\hat{\mathcal{H}}^*t)\hat{\rho}^*(0)\exp(i\hat{\mathcal{H}}^*t) \quad (4.26)$$

where $\hat{\rho}^*(0)$ is the initial density operator at time $t = 0$ in the toggling frame. Calculating the average Hamiltonian within the toggling frame truncates the expression 4.32 for the average Hamiltonian to the first-order term $\hat{\mathcal{H}}^0$ only, providing that the toggling frame Hamiltonians which occur at different times in the time period considered, commute with each other in this frame. The toggling frame density operator calculated in this way is completely equivalent to the more usual rotating frame density operator, but more simply expressed with respect to a different frame.

The principle of the toggling frame can be applied to calculate $\hat{\mathcal{H}}^0$ which in the first-order approximation for WHH-4 can be written as:

$$\hat{\mathcal{H}}^0 = \frac{\hat{\mathcal{H}}_{zz}\tau + \hat{\mathcal{H}}_{yy}\tau + 2\hat{\mathcal{H}}_{xx}\tau + \hat{\mathcal{H}}_{yy}\tau + \hat{\mathcal{H}}_{zz}\tau}{6\tau} \quad (4.27)$$

where

$$\begin{aligned} & \hat{\mathcal{H}}_{xx} + \hat{\mathcal{H}}_{yy} + \hat{\mathcal{H}}_{zz} \\ &= \sum_{i>j} B_{ij} (3\hat{I}_x^i \hat{I}_x^j - \hat{\mathbf{I}}^i \cdot \hat{\mathbf{I}}^j) + (3\hat{I}_y^i \hat{I}_y^j - \hat{\mathbf{I}}^i \cdot \hat{\mathbf{I}}^j) + (3\hat{I}_z^i \hat{I}_z^j - \hat{\mathbf{I}}^i \cdot \hat{\mathbf{I}}^j) \equiv 0 \end{aligned} \quad (4.28)$$

using

$$\hat{\mathbf{I}}^i \cdot \hat{\mathbf{I}}^j = \hat{I}_x^i \hat{I}_x^j + \hat{I}_y^i \hat{I}_y^j + \hat{I}_z^i \hat{I}_z^j \quad (4.29)$$

In other words, there is no net interaction acting on the spin system at the end of the pulse sequence to first order in the dipolar coupling; the effects of the dipolar coupling have been averaged to zero to first order. Important to notice is the fact that throughout this analysis the toggling frame Hamiltonian has been expressed in terms of operators defined with respect to the usual rotating frame. This allows the summation of Hamiltonian from different toggling frames. Furthermore, the toggling frame density operator calculated from the final average Hamiltonian analyzed in this way is then expressed in terms of rotating frame operators and is therefore identical to the rotating frame density operator.

In this work chemical shift played a very important role. That is why it was also interesting to determine what happened to any chemical shift

terms under the WHH-4 pulse sequence. The Hamiltonian describing the chemical shift is the usual

$$\hat{\mathcal{H}}_{cs} = -\omega_{cs}\hat{I}_z \quad (4.30)$$

where ω_{cs} is the chemical shift and $\hat{I}_z = \sum_i \hat{I}_z^i$. The first-order average Hamiltonian for the chemical shift interaction is

$$\hat{\mathcal{H}}_{cs}^0 = -\omega_{cs} \frac{\hat{I}_z\tau + \hat{I}_y\tau + 2\hat{I}_x\tau + \hat{I}_y\tau + \hat{I}_z\tau}{6\tau} = -\frac{1}{3}\omega_{cs}(\hat{I}_x + \hat{I}_y + \hat{I}_z) \quad (4.31)$$

The last part of this equation shows that all spins are scaled by a factor of $\frac{1}{\sqrt{3}}$ while using WHH-4. The size of any interaction linear in \hat{I}_z will be scaled by the same factor, and this includes any heteronuclear dipolar couplings acting on the I -spins. All the pulse sequences are designed to average out the effects of homonuclear dipolar-coupling scale chemical shifts, though the particular scaling factor depends on the particular pulse sequence.

4.2 Field-Cycling Spectroscopy

In this section some important information about the field-cycling experiments is presented. There are basically two ways to achieve magnetic field variation in order to measure a Nuclear Magnetic Relaxation Dispersion (NMRD) profile.

The first one consists of mechanical translation of the sample between areas with different field intensities [101–103]. However, it was not used in this work; more about the design and difficulties can be found in the work of H. Stork [97].

The second way uses electronic modulation of the current flowing through the coil of an electromagnet. This technique, commonly called Fast Field Cycling (FFC) NMR relaxometry, permits very fast variations of the field induction. All the relaxation measurements have been performed on a home-built fast field cycling spectrometer [94, 95]. The FC-technique avoids sensitivity problems of NMR in low magnetic fields by splitting the experiment into three different phases [94], which are shown in figure 4.9. During the polarization period the sample is polarized in a magnetic field $B_0=1\text{T}$. The relaxation process takes place in the evolution period B_e , where the magnetic field is switched for a time t_e to the desired frequency ω_e . In the presented experiments these evolution frequencies (fields; $\omega=\gamma_{19F}B$) ranged from 20 kHz to 40 MHz (for ^1H frequency). The

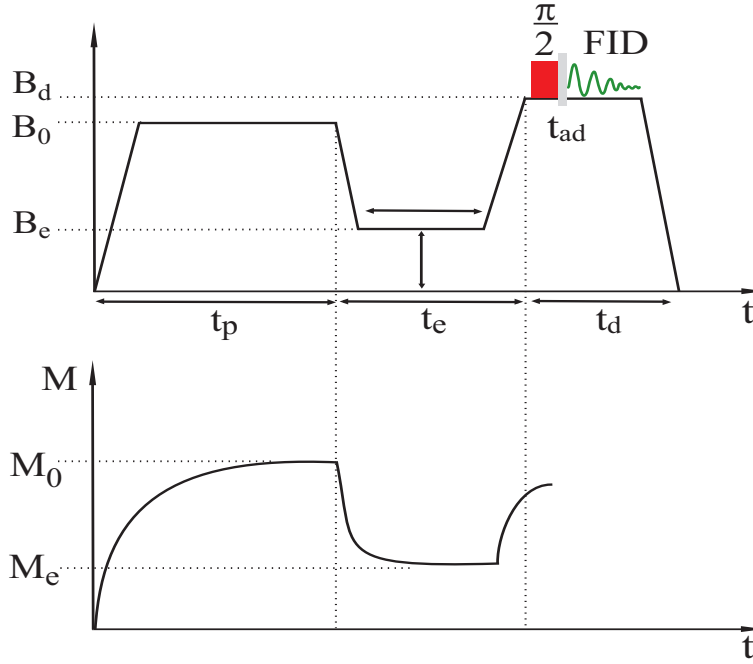


Figure 4.9: A typical field cycle. The sample is polarized in a high magnetic field B_0 and the NMR signal is recorded in detection field B_d . The relaxation process takes place during the evolution period t_e , where the evolution field B_e is switched to the desired frequencies.

detection of the remaining magnetization is performed again in a constant, high magnetic B_d by recording the free induction decay following a $\frac{\pi}{2}$ -pulse. The detection frequency has been 40 MHz. By varying the time t_{evo} spent in the evolution field B_e the corresponding spin-lattice relaxation rate $\frac{1}{T_1}(\omega_e)$ can be evaluated. For resonance frequencies above 16 MHz a variation of the described FC-scheme has been used. The experiments have been performed without a polarization period, so no decay of the magnetization during t_e has been observed, but the build-up from zero. For higher frequencies this technique offers a larger dynamical range, since the difference between the equilibrium magnetization in the polarization- and the evolution- field becomes small. In an intermediate frequency range both techniques, i.e. with and without polarization, have been applied and have shown no significant deviations. The setup is equipped with additional coils to compensate for stray fields perpendicular to the B_0 . This is important to ensure adiabatic switching conditions at low magnetic fields [94]. All temperature-dependent measurements have

been performed using a home-built high temperature probe head, which is presented in the next section [96]. A more detailed description of the used Fast Field Cycling NMR Spectrometer can be found in the work of O. Lips [8].

4.2.1 High Temperature Probe Head

For the investigation of fluorine dynamics it was essential to vary the temperature up to 1200K. Therefore a new high-temperature probe head has been designed [96].

The basic probe head (PH) parameters, i.e. the length, diameter, and the number of windings of the high-frequency coil were limited by the inner dimension of the magnet and the B_0 magnetic field generated by the "main coil". The probe head consists of an NMR Pt-coil placed at the bottom and surrounded by a shielding cap with mini-furnace and thermal insulation and water cooling. The cross section of the probe head is shown in figure 4.10. Since the sample is placed inside the high-frequency

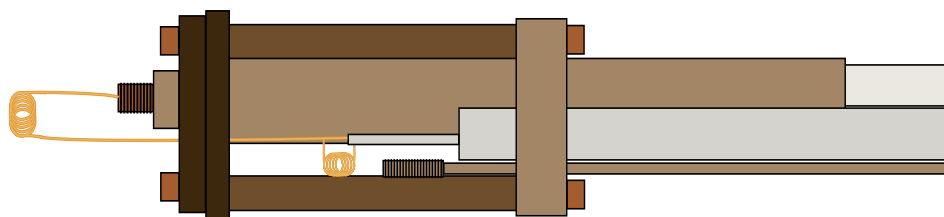


Figure 4.10: Schematic representation of the high-temperature probe head.

coil and covered by the brass cap, an additional thermocouple (Type K) was used. It is separate from the one which is on the outside wall to control the temperature of the cooling water. The heated-volume is small and contains only the NMR coil with the thermometer. The NMR coil has 7-9 windings of Pt-wire (diameter 0.6 mm). The inner diameter of the coil is 5 mm in order to enable the insertion of NMR samples which are, for example, sealed in NMR quartz tubes. The high frequency coil can easily be replaced by a different one. Thermo-insulation is achieved by a special porous ceramic material, with very low heat conductivity (KVS 161), as well as the regulation of the circulating water. A thick oxide ceramic plate which has three holes for all the necessary wires separates the sample from the tuning part. Below it a copper support is used. The home-made tuning elements, presented in figure 4.10, are standard models for single-frequency design. The coaxial tuning capacitor is of the sort in which a

dielectric is inserted from one side and can be used to adjust the required resonant frequency by varying the length of the dielectric part. The helical matching coil has 15 turns. Its inductance is tunable by a cylindrical threaded brass rod with a diameter of 0.4 mm to permit optimal matching to 50Ω over the whole temperature range. The brass cap has spiral tubing on the outside where the cooling water is running through, and the Pt-furnace is placed inside. The micro furnace is made from a thick-wall alumina (oxide ceramic) cylinder, shown in figure 4.11, and a 0.4 mm Pt heating wire. On the outer surface of the cylinder grooves were cut for

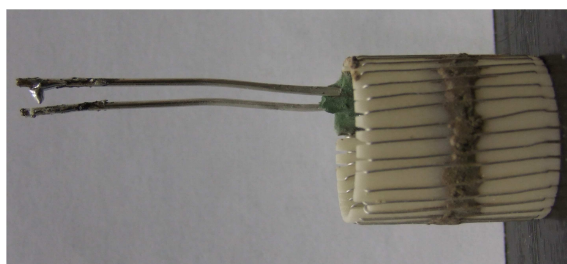


Figure 4.11: Furnace with Pt-wire and current plugs.

the winding of the Pt-wire. The wire was wound bifilar which guarantees low stray fields and a weak coupling to the B_1 -field. The current plugs were made of 1.2 mm Pt-wire and spot-welded to the ends of the heating wire. The temperature was measured with a Type-K thermocouple, and controlled with a home-made temperature controller. More details can be found in literature [96].

During acquisition the furnace was switched off to avoid any influences on the NMR signal. Since the acquisition took at most a few milliseconds this has no influence on the temperature stability.

4.3 Static Field Gradient NMR

The two NMR-methods presented until now, were using a magnetic field with good homogeneity. The Static Field Gradient NMR (SFG), on the other hand, is based on stable field gradients, which can even be found in the techniques mentioned above, although they are not as strong as specially introduced static field gradients. The main feature is the anti-Helmholtz design of split superconducting coils. The field profile and the z -dependent magnetic field gradient of such a magnet (from Magnex Scientific and Oxford Instruments) is shown in figure 4.12. In the vertical

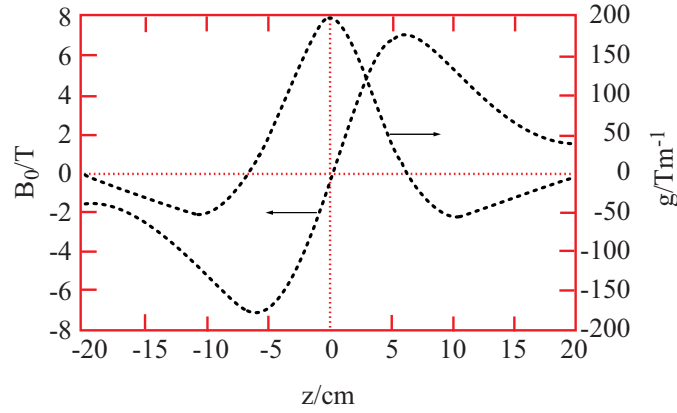


Figure 4.12: Gradient profiles of the magnetic field in a Oxford magnet.

center of the magnet the magnetic field is zero but it increases rapidly if the sample position is moved a few centimeters from the center and this is the basic principle of all field gradient NMR techniques: the Larmor frequency $\omega = \gamma r g(z)$ where g is the magnetic field-gradient vector, depends on the absolute position of the spins in the inhomogeneous field $r(t)$.

The experimental setup is very similar to the one shown in figure 4.1. The differences are mainly in the receiver-part which is home-built, and the ATM 2kW high-power transmitter was used instead of a 400W transmitter, as in the case of the lineshape spectrometer.

4.3.1 Hahn Echo

A magnetization which has decayed in the rotating $x' - y'$ plane due to external field inhomogeneity can be refocussed into an echo by an appropriate pulse. Such an echo is called a Hahn echo, figure 4.13 and was used for the static field gradient experiments. The first $\frac{\pi}{2}$ -pulse produces coherent transverse magnetization which evolves in the gradient field during a dephasing period τ . The second π -pulse, inverts the sign of the net accumulated phase of the spins. Thereafter, the magnetization is still in the transverse plane and the spins precess with their Larmor frequencies, thus reducing their accumulated phases. As long as there is no change in the positions of the nuclei, this re-phasing rate is the same as the dephasing rate, so that at a time 2τ the magnetization again reaches its coherent initial state forming a spin echo.

The measured Hahn echo height $S(\tau, t_m)$ is given by [107]:

$$S(\tau) = S_0 e^{-\frac{2}{3}\gamma^2 g^2 D \tau^3} e^{-\frac{2\tau}{T_2}} \quad (4.32)$$

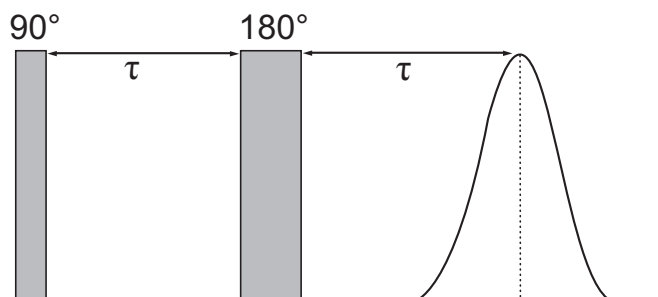


Figure 4.13: Pulse sequence for the Hahn echo in static field gradient experiments.

4.3.2 Solid Echo

In dipolar coupled solids where the local field is not static a solid echo is normally used. Broad lines, such as those arising from dipolar coupling have rapidly decaying FIDs. To overcome this problem the solid echo pulse sequence is very often used.

Considering again the Hahn echo sequence $(\pi/2)_0 - \tau - (\pi)_{90} - \tau - echo$. It should not give rise to any echoes in a dipolar system of one kind of spins in solids because the second pulse simply inverts all spins and, consequently, the local fields as well. A sequence which results in an echo, however, is the solid echo $(\pi/2)_0 - \tau - (\pi/2)_{90} - \tau - echo$, $\tau < T_2$, figure 4.14. Under the condition $\tau \ll T_2$, the trailing half of the echo is equal to the FID. Therefore, the solid echo is a good technique for overcoming the effects of the deadtime in determining the FID shape.

Fourier spectra of the second half of echo signals were recorded for "low concentration" of the admixtures for $Ba_{1-x}La_xF_{2+x}$, $x = 0, 0.0005, 0.001$.

4.3.3 Stimulated Echo

Another very useful pulse sequence is the stimulated echo which can "stop" the evolution of the magnetization under the influence of the field gradient. Figure 4.15 shows the stimulated echo pulse sequence. After the first pulse, the magnetization is in the transverse plane and the spins accumulate a z -dependent phase. The second $\frac{\pi}{2}$ -pulse turns the magnetization

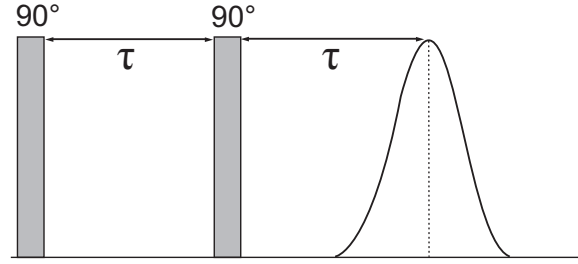


Figure 4.14: The Solid-Echo sequence.

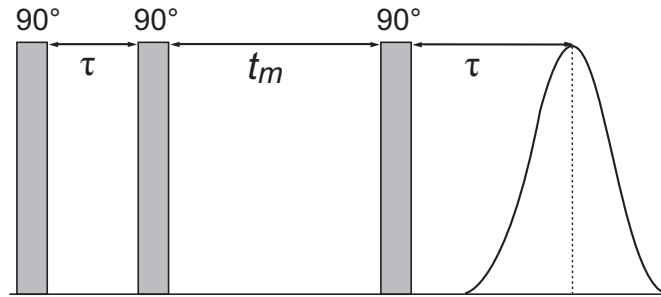


Figure 4.15: Pulse sequence for the Stimulated echo in static field gradient experiments.

back in the z -direction, parallel to the magnetic field, and stops the evolution of the individual spins under the influence of the field gradient. The third pulse, applied after a long "diffusion period" t_m , where the diffusion process can occur, turns the magnetization back into the transverse plane, where it again evolves, figure 4.16. The phases of the second and third pulse are chosen so that the overall turn angle is again π . Thus, after the third pulse, the magnetization starts to refocus and forms an echo at time τ .

The stimulated echo experiment measures the echo height $S(\tau, t_m)$, which basically correlates the phase of a tagged nuclear spin gained by dephasing during the interval of length τ before the diffusion period t_m with its phase returned by its rephasing during the interval of the same length τ (figure 4.15).

Due to T_2 -relaxation in the dephasing and rephasing periods and T_1 -relaxation in the storage period, the measured echo height $S(\tau, t_m)$ is given

by [107]:

$$S(\tau, t_m) = S_0 e^{-\gamma^2 g^2 \tau^2 D(t_m + \frac{2}{3}\tau)} e^{-\frac{2\tau}{T_2}} e^{-\frac{t_m}{T_1}} \quad (4.33)$$

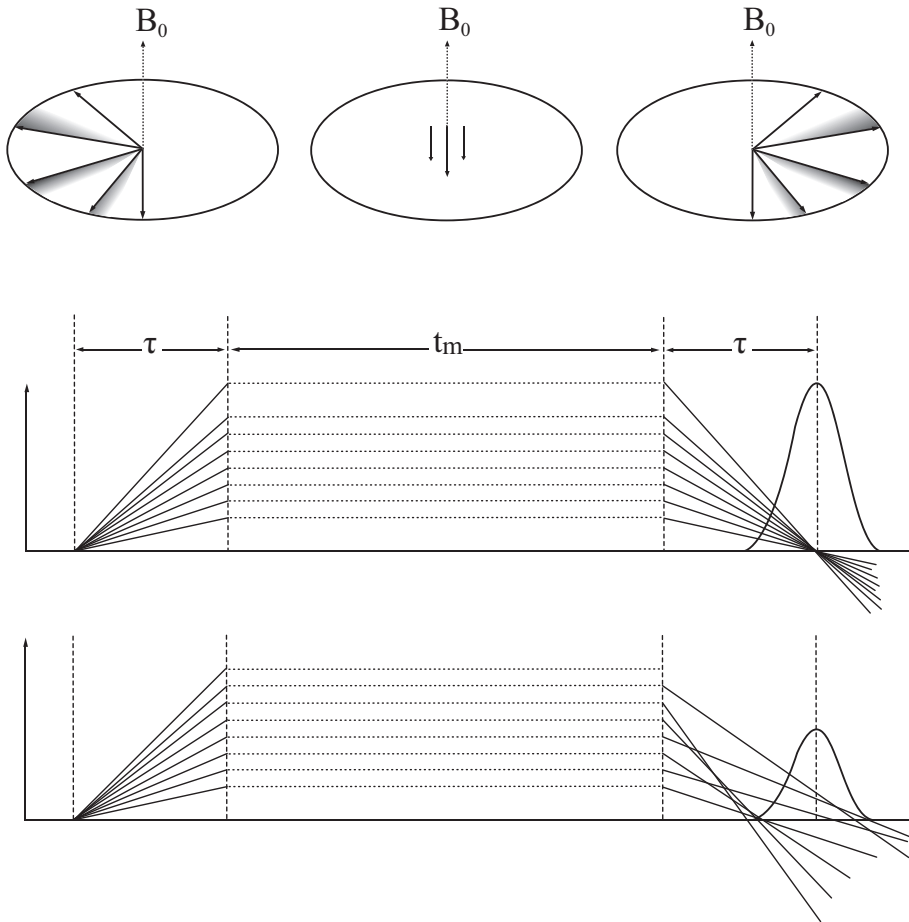


Figure 4.16: Evolution of the magnetization during the stimulated echo in a static field gradient experiments.

Chapter 5

Measurements and Analysis

In the present chapter, the experimental and theoretical results of the fluorine dynamics studies of barium fluoride are given. As already mentioned, three different NMR-methods were used to study mobility of fluorine ions. The first one, Static Field Gradient NMR, investigated the ion movement on the macroscopic scale, while the two others, lineshape analysis and field cycling relaxometry observe on the microscopic scale.

5.1 Diffusion Measurements

Static Field Gradient (SFG) NMR is a well-established method for measuring self-diffusion. Until now no systematic temperature-dependent measurements of the diffusion coefficient in BaF₂-system have been performed. It was possible to learn more about the influence of the temperature treatment on "fresh samples", identify the change of the dynamic for different concentration of the La³⁺ impurities and to calculate the activation energies.

The experiments have been carried out in a specially designed magnet (chapter 4) at two gradient values, 40 T/m and 180 T/m (¹⁹F resonance frequency was 80 MHz), using a home-built high-temperature probe head (section 4.2.1, figure 4.10). Both Hahn [104] and stimulated-echo pulse sequences [105], as was mentioned in chapter 4, have been used for estimating the diffusion coefficient in the temperature range from 300K up to 1200K.

Measured data were analyzed by fitting them using two functions presented in chapter 4 (equations 4.32 and 4.33) and the Levenberg-Marquardt algorithm. Two parameters T_2 and D were kept the same for all data, mixing time t_m for Hahn echo was equal zero and for Stimulated echo $t_m > 0$.

An example of the measurements and fitted curves is shown in figure 5.1.

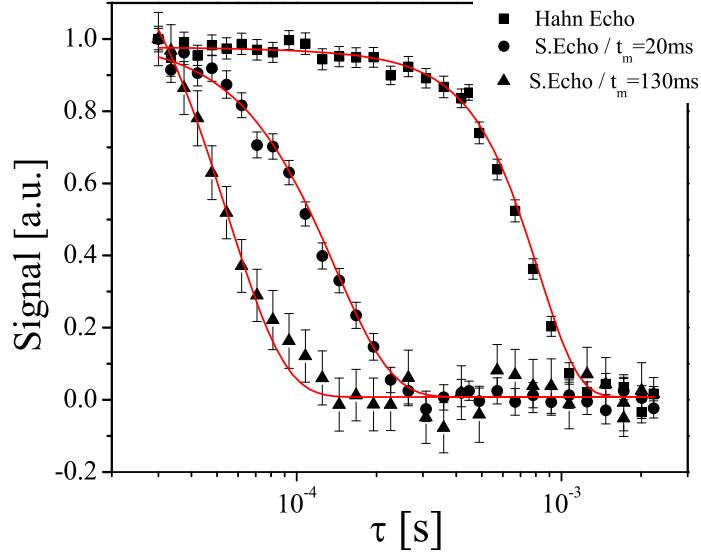


Figure 5.1: Example of the ^{19}F -diffusion measurements in $\text{Ba}_{1-x}\text{La}_x\text{F}_{2+x}$, where $x = 0.001$ at 800K. Sample was oriented parallel to the main magnetic field.

5.1.1 Aging Effect

All samples were prepared in the same way, by sealing in quartz tubes under vacuum (chapter 4). No pre-measurements were performed. This is a very important point, since it is known that treating fluorides, especially LaF_3 , at high-temperature can influence the dynamics of the F^- - ions [8].

This phenomenon has also been found in the BaF_2 -system performing the T_1 and diffusion measurements. In the measured samples high temperatures caused a change of the dynamics as expected. Figure 5.2 shows an example of the diffusion coefficient for the same sample heated to 1100K for the first time, cooled down and heated once again to 1050K. This "aging effect" may be attributed to structural changes after the heating. During the high temperature treatment, thermally activated defects are created and distributed over various sites in the sample where they stay during cooling.

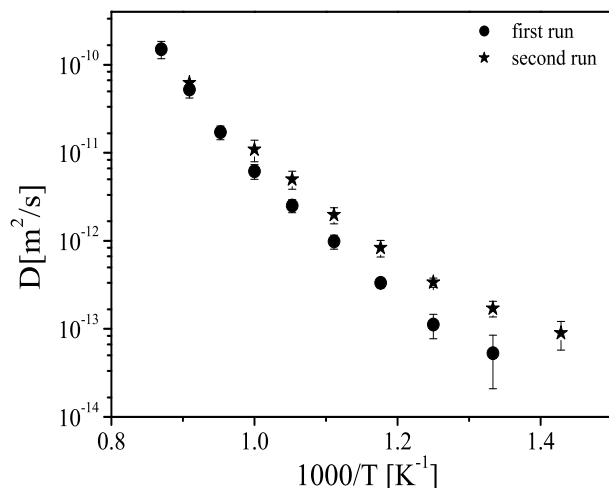


Figure 5.2: ^{19}F Diffusion measurements in $\text{Ba}_{1-x}\text{La}_x\text{F}_{2+x}$, where $x = 0.001$ in the temperature range from 300K to 1100K. Sample was oriented parallel to main magnetic field.

To obtain identical dynamic conditions for further investigation, all samples have been deliberately aged (heated to 1200K and cool down to 300K ten times).

5.1.2 Influence of Trivalent Impurities

Another objective of this work was the investigation of the change of diffusion coefficients and activation energy in a set of samples with different concentrations of trivalent impurities ($\text{Ba}_{1-x}\text{La}_x\text{F}_{2+x}$). Figures 5.3 and 5.4 show semi-logarithmic plots of the dependence of D on inverse temperature for different dopant concentrations.

At higher concentration ($\text{Ba}_{1-x}\text{La}_x\text{F}_{2+x}$, where $x = 0.03, 0.1$), the data can be divided (figure 5.4) into two distinct temperature regions having different slopes with two different activation energies: region I appears between $1.3\text{--}1.0 \times 10^{-3} \text{ K}^{-1}$ with the activation energy of about $0.85 \pm 0.1 \text{ eV}$; region II appears in the range from 1.82 to $1.4 \times 10^{-3} \text{ K}^{-1}$ with the activation energy of about $0.35 \pm 0.05 \text{ eV}$.

For $\text{Ba}_{0.99}\text{La}_{0.01}\text{F}_{2.01}$ (figure 5.3) only one region seems to exist ($(1.3\text{--}1.0) \times 10^{-3} \text{ K}^{-1}$; region I). This region is also present for other lightly doped

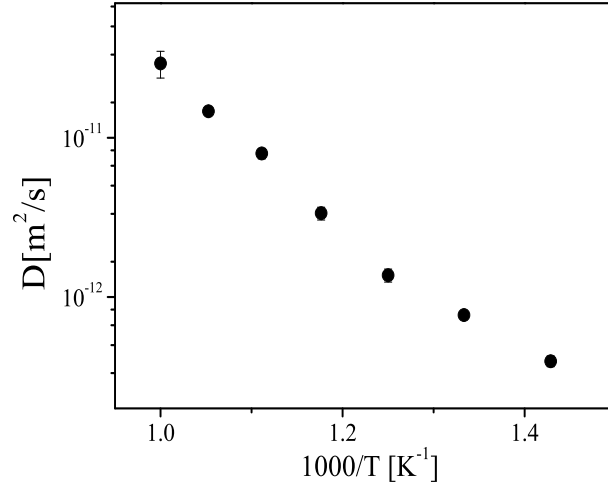


Figure 5.3: ^{19}F Diffusion measurements in $\text{Ba}_{1-x}\text{La}_x\text{F}_{2+x}$, where $x = 0.01$ in the temperature range from 650K to 1000K.

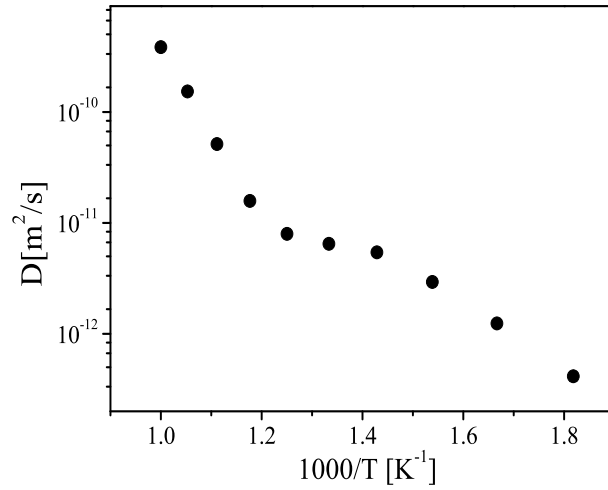


Figure 5.4: ^{19}F Diffusion measurements in $\text{Ba}_{1-x}\text{La}_x\text{F}_{2+x}$, where $x = 0.03$ in the temperature range from 550K to 1100K.

samples ($x = 0, 0.0005, 0.001$). The slopes are the same for these samples, corresponding to an activation energy of about 0.85 ± 0.1 eV.

5.1.3 Discussion

In the SFG experiments, diffusion coefficients for different concentrations have been examined. Figure 5.5 shows the final results. Two regions can be observed: the high temperature intrinsic region and the extrinsic region.

The first one is present in all samples and starts at different tempera-

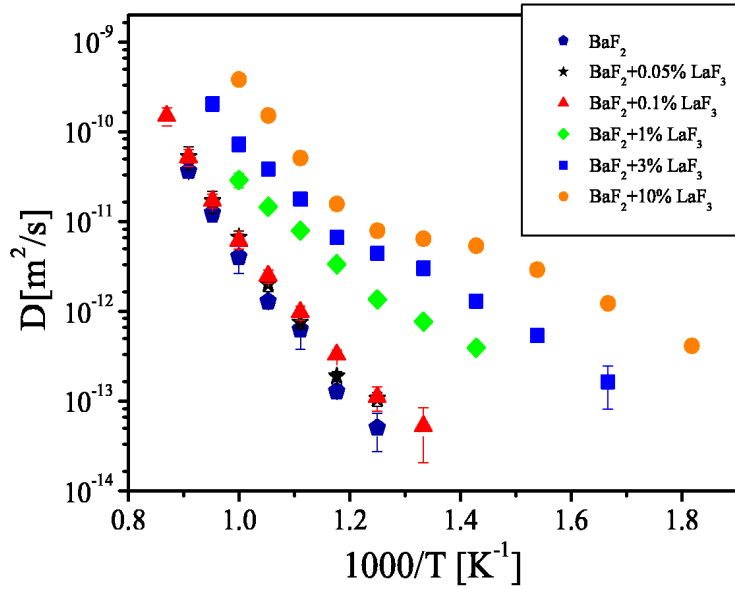


Figure 5.5: ^{19}F Diffusion measurements in $\text{Ba}_{1-x}\text{La}_x\text{F}_{2+x}$, where $x = 0, 0.0005, 0.001, 0.01, 0.03, 0.1$.

tures for different concentrations it shifts to higher temperatures with increasing concentration. The dynamical processes in this region are mainly dominated by the creation of new defects. The corresponding activation energy, very similar to that obtained by Wapenaar in ionic conductivity measurements [108], and Ailion in NMR T_1 -measurements [20], describes both, the creation and the movement of already existing defects.

For higher La^{3+} concentrations, as in (figure 5.4, a second region II (extrinsic region) appears between $(1.82-1.4) \times 10^{-3} \text{ K}^{-1}$. The slopes of the

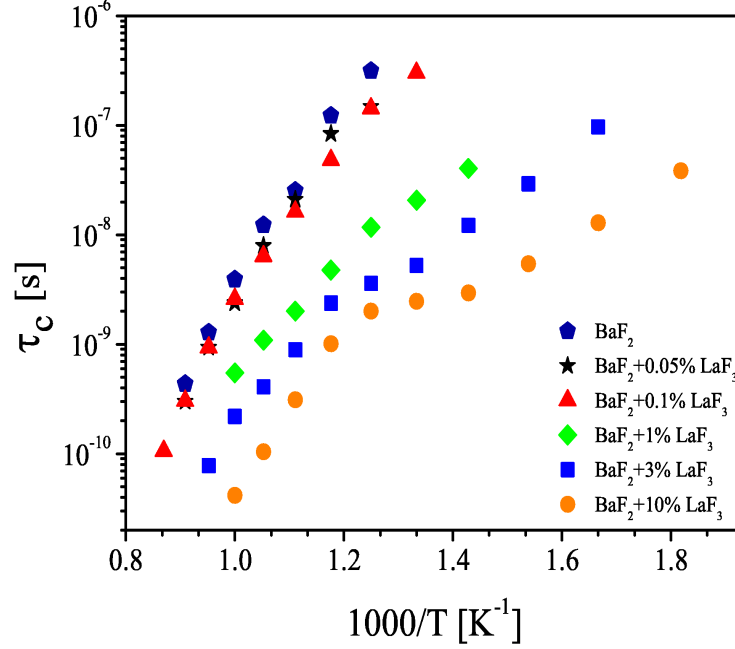


Figure 5.6: Correlation times calculated from temperature-dependent diffusion measurements.

plotted data are less steep than those in the intrinsic region, and the activation energy is about 0.35 ± 0.05 eV. The second region (II) appears between $(1.82-1.4) \times 10^{-3} \text{ K}^{-1}$ and can be characterized as an extrinsic region. The corresponding activation energy is smaller compared to the intrinsic region, and the absolute value of the diffusion coefficient is dependent on the concentration of the admixture ($\text{Ba}_{1-x}\text{La}_x\text{F}_{2+x}$, where $x = 0.03, 0.1$). Region II is associated with motion of already existing defects. Ailion et al. [20] presented an explanation based on comparison of the diffusion data with relaxation. The motion of fluorine ions bound to the La^{3+} - impurities is "partially dissociated". This means that the ions may jump to a more remote, but still bound site relative to La^{3+} .

The correlation times were also calculated according to the isotropic Random Walk model for free-diffusion, $\langle r^2 \rangle = 6D\tau$, with r equal 3.1 \AA (figure 5.6; section 2.4.2).

5.2 Lineshape Analysis

The second method used in this work was NMR lineshape analysis, for which experimental results are presented for the series of $\text{Ba}_{1-x}\text{La}_x\text{F}_{2+x}$, with $x = 0.0005, 0.001, 0.01, 0.03, 0.1$. It was possible to learn more about the mobility of fluorine ions on a local scale (nearest neighbor), as well as about the influence of trivalent impurities on lineshapes. A series of spectra measured at different temperatures and dopant concentrations is shown below. Analyzing the "stack plots" (figure 5.7 to 5.17), it is easy to recognize that the line becomes narrow at certain temperatures for the respective concentration of admixtures. For example in case of pure BaF_2 , narrowing occurs at 700K, whereas for $\text{Ba}_{0.9}\text{La}_{0.1}\text{F}_{2.1}$, this happens already at $\approx 450\text{K}$. Also the difference between the shape of the spectrum of pure

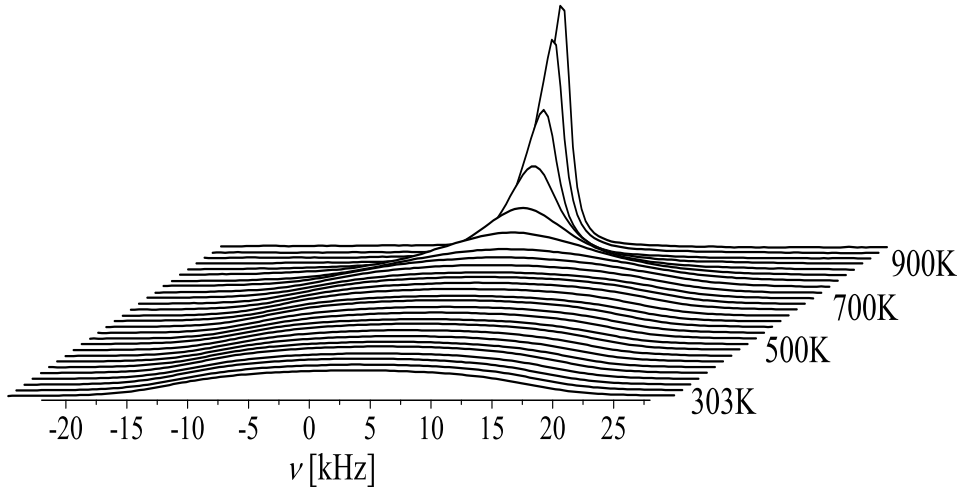


Figure 5.7: ^{19}F -Lineshape measurements of pure BaF_2 . Sample was oriented parallel to main magnetic field \vec{B}_0 .

BaF_2 and one with high-concentration, i.e. $\text{Ba}_{0.9}\text{La}_{0.1}\text{F}_{2.1}$, (figure 5.7 and 5.17) can be easily noticed. The next section provides a detailed discussion about these types of effects.

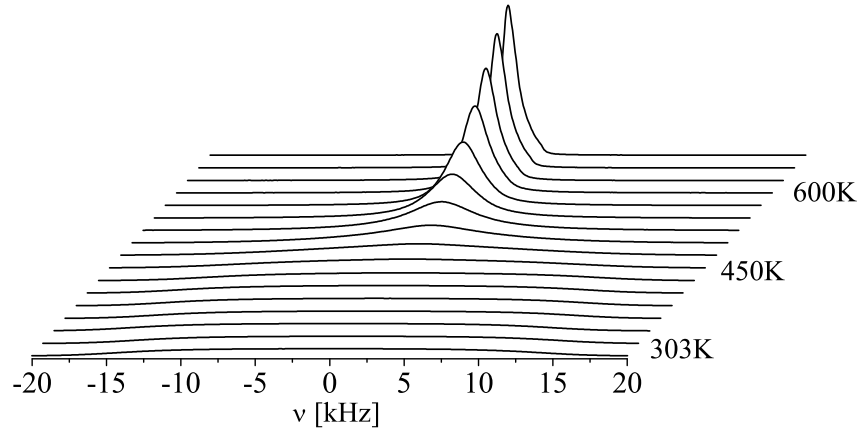


Figure 5.8: ^{19}F -Lineshape measurements of $\text{Ba}_{1-x}\text{La}_x\text{F}_{2+x}$, where $x = 0.0005$. Sample was oriented parallel to main magnetic field \vec{B}_0 .

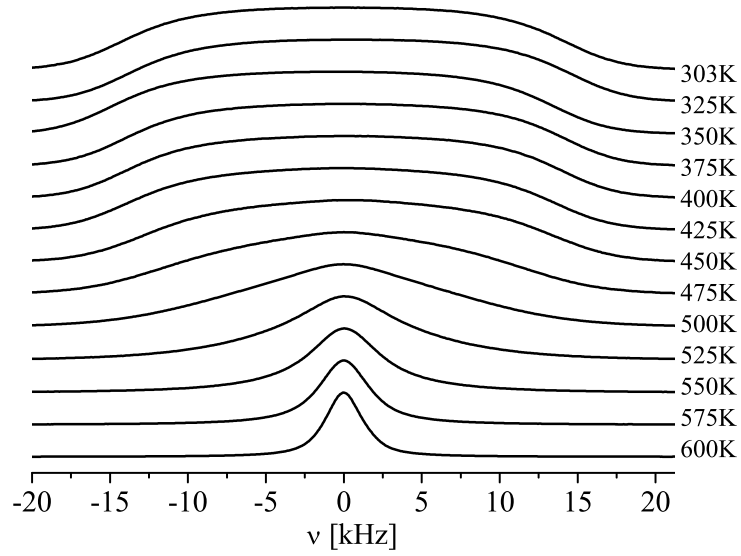


Figure 5.9: ^{19}F -Lineshape measurements of $\text{Ba}_{1-x}\text{La}_x\text{F}_{2+x}$, where $x = 0.0005$. Flat representation of the spectra in the temperature range of 303K-600K.

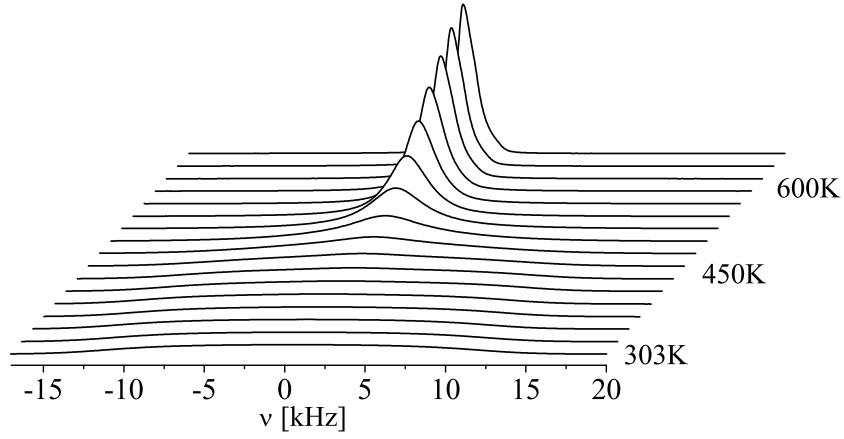


Figure 5.10: ^{19}F -Lineshape measurements of $\text{Ba}_{1-x}\text{La}_x\text{F}_{2+x}$, where $x = 0.001$. Sample was oriented parallel to the main magnetic field \vec{B}_0 .

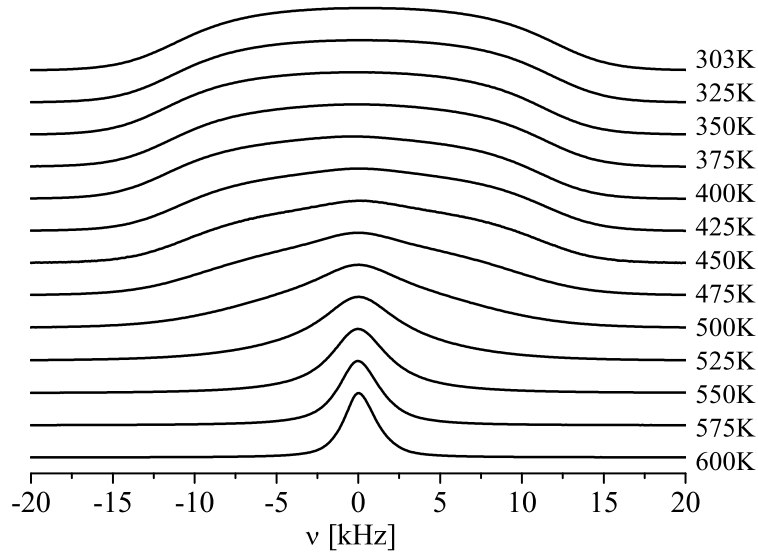


Figure 5.11: ^{19}F -Lineshape measurements of $\text{Ba}_{1-x}\text{La}_x\text{F}_{2+x}$, where $x = 0.001$. Flat representation of the spectra in the temperature range of 303K-600K.

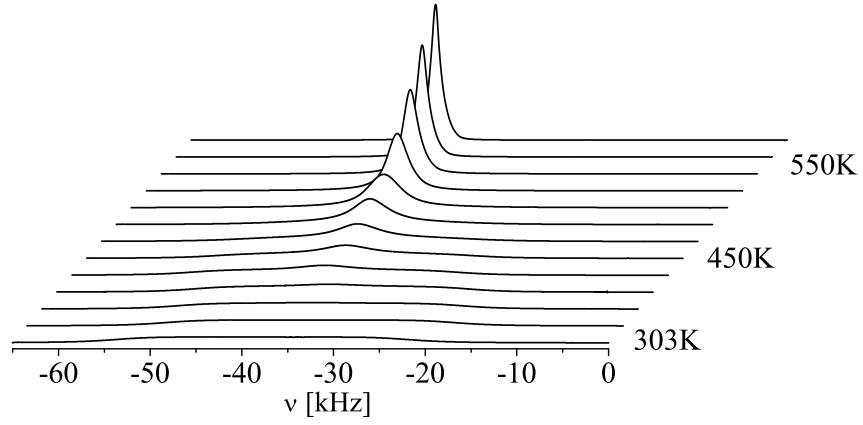


Figure 5.12: ^{19}F -Lineshape measurements of $\text{Ba}_{1-x}\text{La}_x\text{F}_{2+x}$, where $x = 0.01$. Sample was oriented parallel to the main magnetic field \vec{B}_0 .

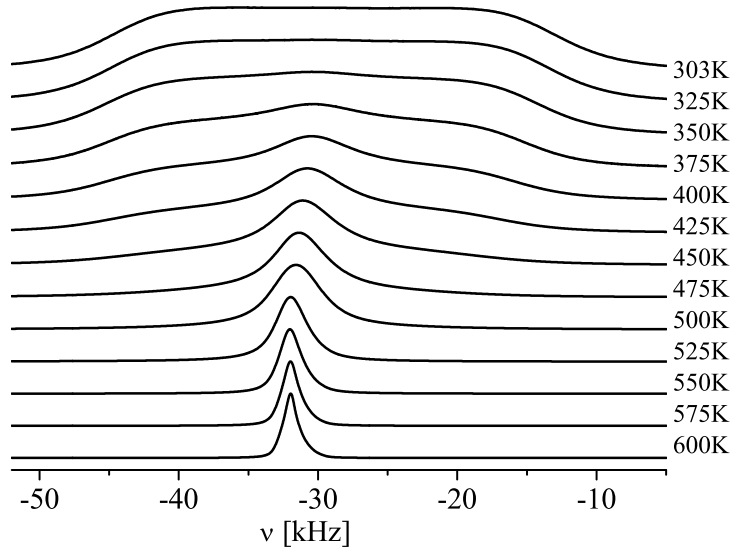


Figure 5.13: ^{19}F -Lineshape measurements of $\text{Ba}_{1-x}\text{La}_x\text{F}_{2+x}$, where $x = 0.01$. Flat representation of the spectra in the temperature range of 303K-600K.

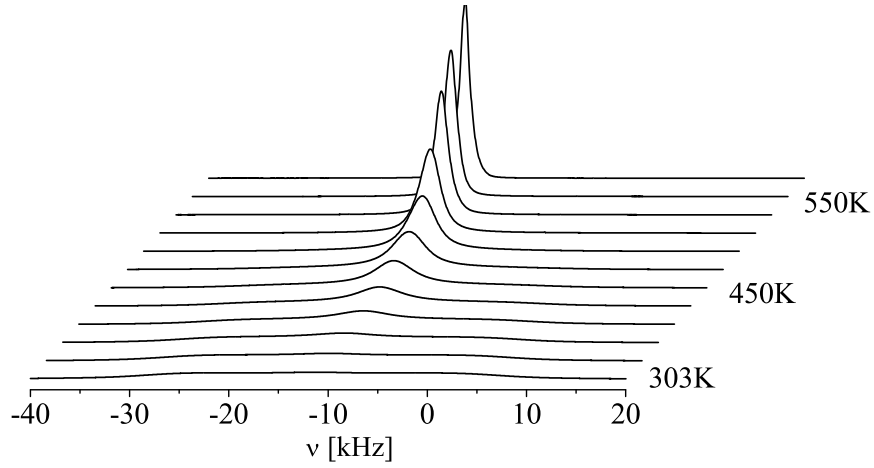


Figure 5.14: ^{19}F -Lineshape measurements of $\text{Ba}_{1-x}\text{La}_x\text{F}_{2+x}$, where $x = 0.03$. Sample was oriented parallel to the main magnetic field \vec{B}_0 .

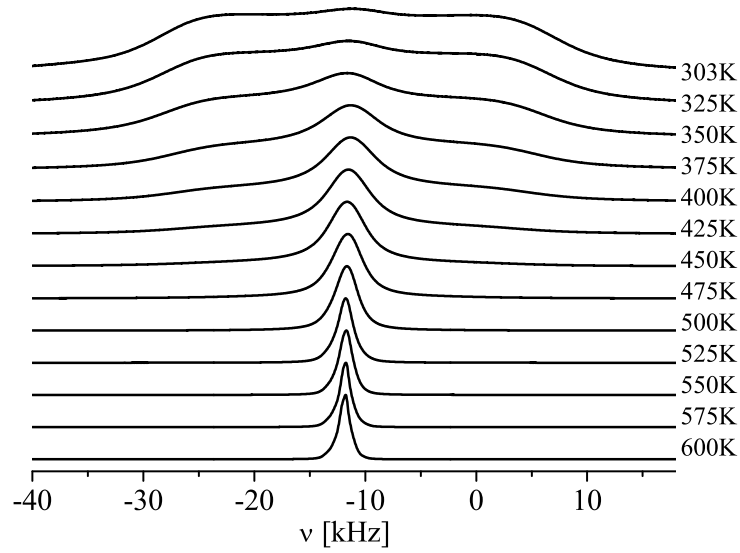


Figure 5.15: ^{19}F -Lineshape measurements of $\text{Ba}_{1-x}\text{La}_x\text{F}_{2+x}$, where $x = 0.03$. Flat representation of the spectra in the temperature range of 303K-600K.

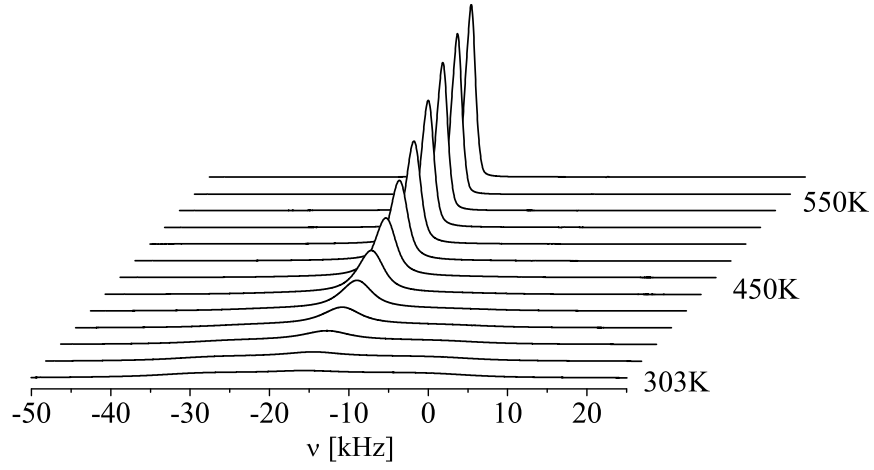


Figure 5.16: ^{19}F -Lineshape measurements of $\text{Ba}_{1-x}\text{La}_x\text{F}_{2+x}$, where $x = 0.1$. Sample was oriented parallel to the main magnetic field \vec{B}_0 .

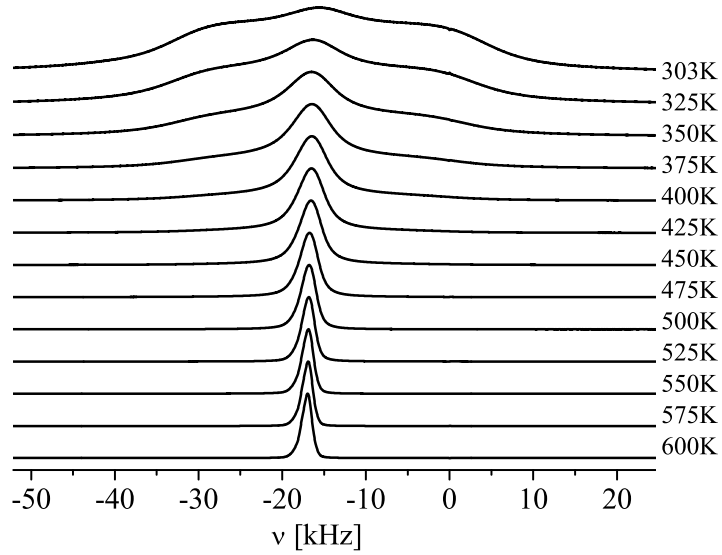


Figure 5.17: ^{19}F -Lineshape measurements of $\text{Ba}_{1-x}\text{La}_x\text{F}_{2+x}$, where $x = 0.1$. Flat representation of the spectra in the temperature range of 303K-600K.

5.2.1 Influence of Doping

The rich experimental data set presented above reflects various aspects of fluorine spin dynamics. As already mentioned, the difference between the pure system and the doped one can clearly be seen at room temperature. Due to the substitution of Ba^{2+} by La^{3+} , which does not change the cubic structure up to the concentration $x \simeq 0.5$, (figure 2.9; chapter 2, section 2.3.1.) interstitial fluorine ions were introduced into the lattice. Those charge compensating ions produce a second subsystem which influences the fluorine dynamics and the shape of the spectrum visible in figure 5.19 as a second relatively narrow line "on top" of the broad line. To ex-

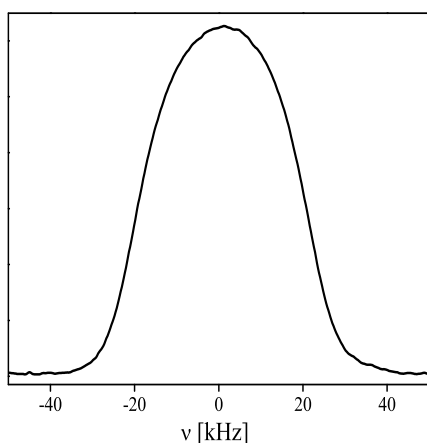


Figure 5.18: ^{19}F -static lineshape measurements of BaF_2 at 300K.

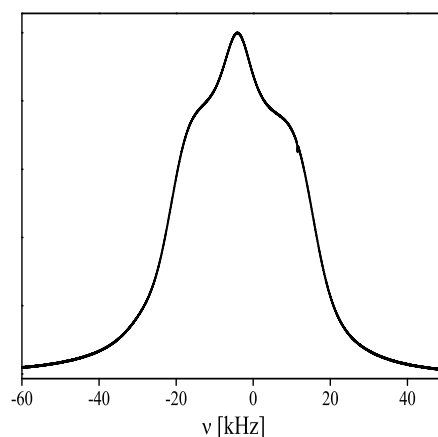


Figure 5.19: ^{19}F -static lineshape measurements of $\text{Ba}_{0.9}\text{La}_{0.1}\text{F}_{2.1}$, at 300K.

tract exact information about the position of the second line, and thus the chemical shift, the magic angle spinning method [109] and multiple-pulse sequences have been tested. The second technique was unfortunately not very successful, since it requires "single point acquisition" technology and reliable software, but the MAS data were good enough to determine the position of the "interstitial" line. More details about these measurements are presented in the following sections.

5.2.2 MAS Measurements

The MAS data were obtained by spinning a $\text{Ba}_{0.9}\text{La}_{0.1}\text{F}_{2.1}$ -powder sample at different frequencies, up to 24kHz, where the second fluorine subsystem could clearly be identified, figure 5.20. The two lines can be assigned to the different crystallographic sublattices, according to the 2:2:2-model (chapter 2, figure 2.13): F_1 denotes the "original" positions of F^- -ions, whereas F_2 describes the interstitial positions of fluorine ions (charge compensating ions). In order to get more valuable information about the dynamics

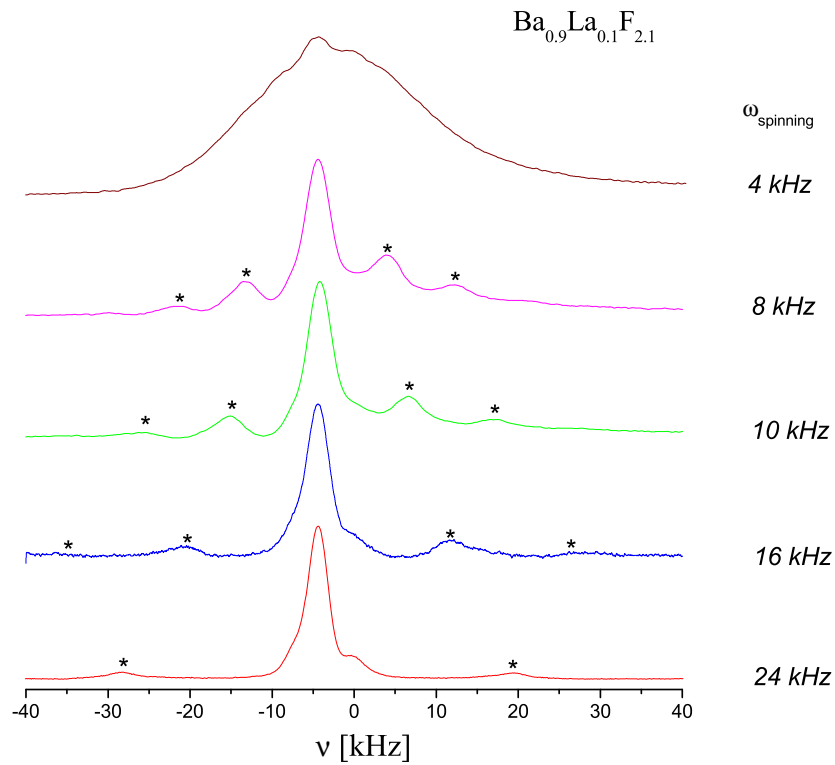


Figure 5.20: ^{19}F -MAS spectra of $\text{Ba}_{1-x}\text{La}_x\text{F}_{2+x}$ -powder sample, where $x = 0.1$. Sample was measured in $\vec{B}_0 = 8.4\text{T}$, at a temperature 300K, and spun at different spinning frequencies, shown on the right.

inside the two subsystems, detailed theoretical analysis was needed. The next paragraph describes the theoretical background.

Figure 5.19 represents a complex spectrum where a clear identification

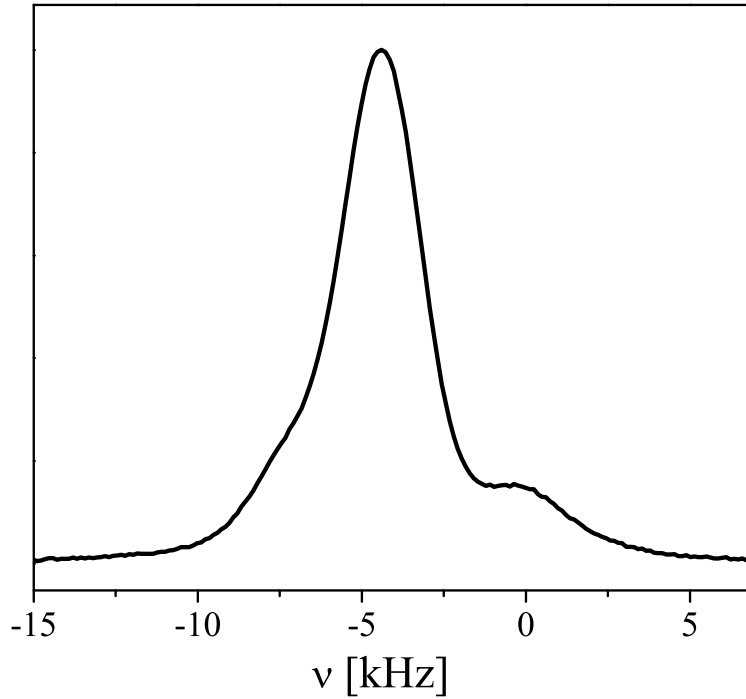


Figure 5.21: ^{19}F -MAS spectrum of a $\text{Ba}_{1-x}\text{La}_x\text{F}_{2+x}$ -powder sample, where $x = 0.1$. Sample was measured in $\vec{B}_0 = 8.4\text{T}$ and spun at 24 kHz.

of fluorine motion inside one sublattice cannot be made without taking into consideration the second subsystem. It is nevertheless very probable that the narrow component on the top of the static spectrum in figure 5.19 can be attributed to the F_1 sublattice. With increasing temperature the two lines, not really well-separated even at room temperature, overlap. This effect indicates thermally activated exchange motion between the two distinct sublattices.

5.2.3 Theoretical Analysis

On the background of the above presented experimental data and neutron scattering measurements (chapter 2, section 2.4.1; at low temperatures and high concentrations of LaF_3), the two fluorine sublattices were distinguishable. Fluorine ions belonging to each of these sublattices move among

equivalent sites within the same sublattice and also jump to nonequivalent sites of the other sublattice. Fluorine spins are coupled to neighboring fluorine as well as lanthanum spins by dipole-dipole interactions in the case of doped samples ($\text{Ba}_{1-x}\text{La}_x\text{F}_{2+x}$, $x = 0.0005, 0.001, 0.01, 0.03, 0.1$). The mutual dipole-dipole couplings affected by temperature-dependent jump dynamics of the fluorine ions determine the shape of the detected NMR spectra.

One-system model In order to calculate the NMR spectrum for the pure BaF_2 sample, which consists only of the F_1 lattice (no admixture of LaF_3 and no interstitial ions), one reference spin I_{ref} needs to be chosen (figure 5.22). Its surroundings, to which it is coupled by dipole-dipole interactions, are formed by N_1 fluorine spins. The total Hamiltonian $\hat{\mathcal{H}}_1$ for the considered ensemble of spins contains the Zeeman and the dipolar couplings for the fluorine spins:

$$\hat{\mathcal{H}}_1 = \sum_{i=1}^{N_1+1} \omega_{F_1}(I_i^1)_z + \hat{\mathcal{H}}_{DD} \quad (5.1)$$

The first term corresponds to the Zeeman coupling of the fluorine spins. The second is the dipole-dipole Hamiltonian $\hat{\mathcal{H}}_{DD}$, which contains couplings between the reference spin I_{ref} and the environment (env):

$$\begin{aligned} \hat{\mathcal{H}}_{DD}(I_{ref}, I_{env}) = & \frac{\mu_0}{4\pi} \frac{\gamma_F^2}{r_{I_{ref}I_{env}}^3} \left(\frac{3\cos^2\theta_{I_{ref}I_{env},L} - 1}{2} \right) \\ & \left[2I_{refz}I_{envz} - \frac{1}{2}(I_{ref+}I_{env-} + I_{ref-}I_{env+}) \right] \end{aligned} \quad (5.2)$$

The angle $\theta_{I_{ref}I_{env},L}$ describes the orientation of the I_{ref} - I_{env} dipole-dipole axis with respect to the laboratory frame, while $r_{I_{ref}I_{env}}$ is the inter-spin distance. The Hamiltonian $\hat{\mathcal{H}}_1$ determines the energy levels of the selected spin system. To obtain the required eigenvalues, the diagonalization of the $\hat{\mathcal{H}}_1$ in the Zeeman basis $|n\rangle = |m_1^1, \dots, m_{N_1+1}^1\rangle$ is needed. The number of the spins included in the calculations determines the number of energy levels for the system: $(2I_1 + 1)^{N_1}$ ($N_1=8$), where $I_1=\frac{1}{2}$. Single-quantum transitions of the reference fluorine spin I_{ref} , being a part of the coupled spin system, give rise to the observed spectrum. The relevant transition frequencies include the main resonance frequency ω_{F_1} , affected by the dipole-dipole couplings, and can be selected from all transition frequencies $\omega_{\alpha\alpha'}^1 = E_{\alpha}^1 - E_{\alpha'}^1$ between the energy levels, E_{α}^1 , of the considered spin system. For the sake

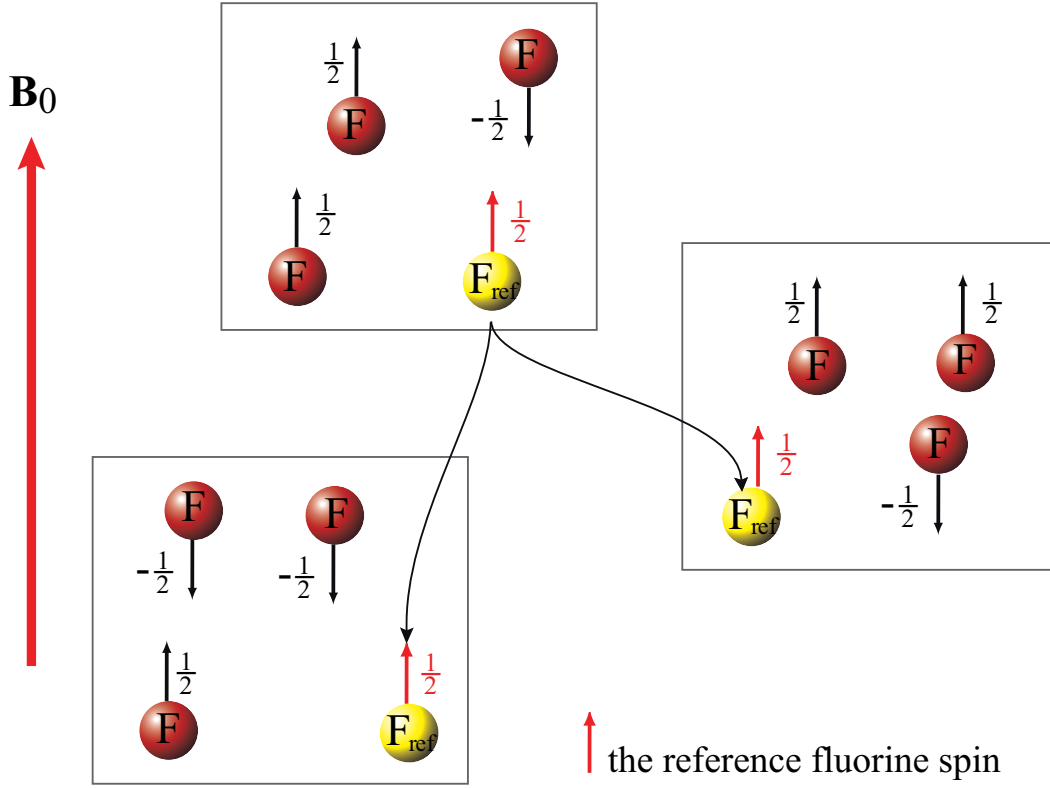


Figure 5.22: Lineshape model for pure and small concentration of x , $\text{Ba}_{1-x}\text{La}_x\text{F}_{2+x}$.

of simplicity, the particular single-quantum coherence $\omega_{\alpha\alpha'}^1$ is defined as follows: ω_{μ}^1 , and the number of relevant single-quantum transitions of the spin I_1 as N_{SQ}^1 , thus $\mu=1, \dots, N_{SQ}^1$. The effects of the jump of the fluorine spin I_1 from one site to another can be treated as a change of its frequency ω_{μ}^1 , caused by different quantum configurations of the new surroundings. Taking into account the notation mentioned above an equation of motion for the density operator $\sigma_{\mu}^1(t)$ (chapter 3), describing the selected spin system can be written as:

$$\begin{aligned} \frac{d\sigma_{\mu}^1(t)}{dt} &= -i\omega_{\mu}^1\sigma_{\mu}^1(t) + \sum_{\nu} \Gamma_{\mu\nu}^1\sigma_{\nu}^1(t) \\ &= \sum_{\nu} (-i\omega_{\nu}^1\delta_{\nu\mu} + \Gamma_{\mu\nu}^1)\sigma_{\nu}^1(t) \\ &= \sum_{\nu} A_{\mu\nu}\sigma_{\nu}^1(t) \end{aligned} \quad (5.3)$$

The summation is restricted to single-quantum coherences relevant for the F_1 fluorine spectrum.

The time domain NMR signal for a spin I is given by the trace of the product of an appropriate density operator $\sigma(t)$ and the operator I_- . Thus, the F_1 lineshape $S_{F_1}(\omega)$ can be obtained as a Fourier transform of the corresponding time domain signal from the following expression [20]:

$$\begin{aligned} S_{F_1}(\omega) &\cong \sum_0^\infty \text{Tr} \{ \sigma_1(t) I_-^1 \} e^{-i\omega t} dt \\ &\cong W(A - i\omega 1)^{-1} \bullet 1 \cong \sum_{\mu\nu} [(A - i\omega 1)^{-1}]_{\mu\nu} \end{aligned} \quad (5.4)$$

The vector W contains the initial density matrix elements $W_\nu = \sigma_\nu(0)$, proportional to probabilities of the corresponding coherence's ω_ν . Because the probabilities are equal they are omitted in the last part of equation 5.4. To complete the expression for the F_1 fluorine spectrum, the transition rates $\Gamma_{\mu\nu}^1$ need to be defined. The jump rate of the fluorine spin I^1 from one position to another is defined as the inverse correlation time τ_1^{-1} .

Performing such a jump, the spin I^1 changes its transition frequency from a value ω_μ^1 (experienced in the initial position) to one of the possible values ω_ν^1 ($\nu=1, \dots, N_{SQ}^1$) associated with the new site. A special case is when $\omega_\mu^1 = \omega_\nu^1$: the spin does not notice any difference.

According to this theoretical model, the spectra for pure BaF_2 crystals and low concentrations of LaF_3 crystals were analyzed.

Two subsystem model For higher concentrations of admixtures a modification of this model has been used. Because there is a second sublattice made of interstitial F^- -anions (chapter 2, section 2.4.1), there should also be an analogy of it in the theoretical analysis. This can easily be adapted by defining the second sublattice F_2 as was done for F_1 , taking into consideration the appropriate surroundings of a reference spin I_2 (representing the second sublattice F_2).

Assuming that its environment consists of N_2 fluorine spins from the sublattice F_2 , and N_1 spins from the sublattice F_1 , the calculation of possible frequencies ω_μ^2 for single-quantum transitions of the spin I_2 is introduced. Because the time for calculations rises rapidly with the number of included spins, a compromise was required. The number of spins was set to a value avoiding missing significant physical effects while keeping the computation time within acceptable limits.

5.2.4 Discussion

The low-concentration samples were analyzed with the model containing only the sublattice F_1 . Figures 5.23 and 5.24 show the theoretical calculation compared with experimental results. The agreement is very good in

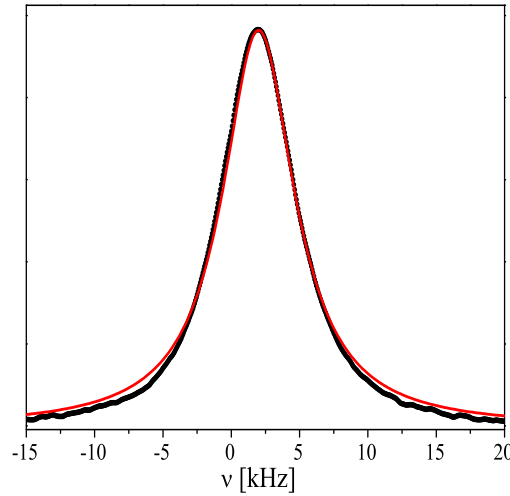


Figure 5.23: ^{19}F -Lineshape measurements (points) and analysis (line) of BaF_2 at 675K.

the temperature range 600K-750K, apart from small deviations which can be observed in the "wings" of the spectrum. This feature is caused by the data treatment. As already mentioned in section 4.1.1, "missing points" at the beginning of the FID were extrapolated using a linear prediction algorithm which predicts the points with considerable accuracy.

In the high concentrations interplay between two subsystems led to a progressing overlap of the F_1 and F_2 lines which already could not be resolved at room temperature. Therefore, the spectra take the form of one a single line which is initially very asymmetrical. A further increase of the temperature reduced the asymmetry, finally reaching the resolution limit of the spectrometer at 500K for the $\text{Ba}_{0.9}\text{La}_{0.1}\text{F}_{2.1}$ -sample.

The resulting correlation times τ_1 collected in figure 5.25 for small concentrations of the admixtures show Arrhenius behavior.

At relatively low temperatures (300K-400K), for both the high and low concentrations, the lineshapes were very broad, up to 30 kHz. The number

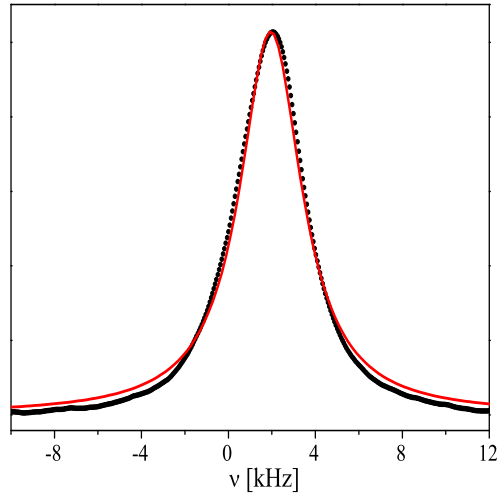


Figure 5.24: ^{19}F -Lineshape measurements (points) and analysis (line) of $\text{Ba}_{1-x}\text{La}_x\text{F}_{2+x}$, where $x = 0.0005$, at 700K.

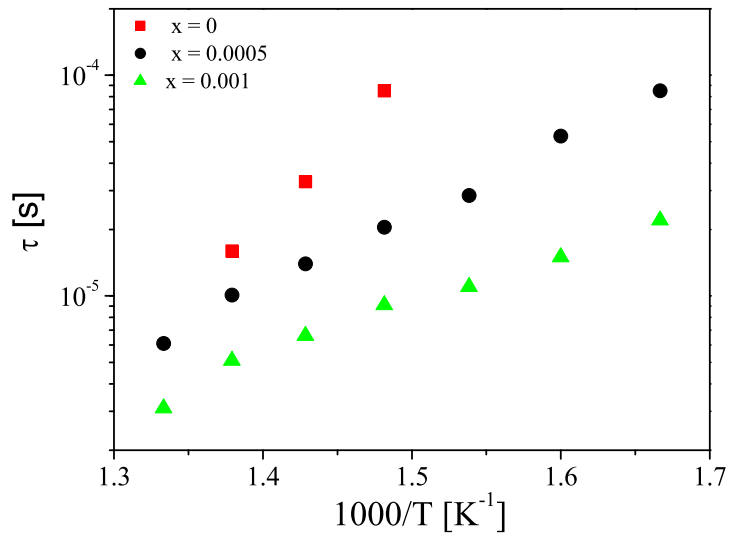


Figure 5.25: ^{19}F correlation times calculated from temperature-dependent lineshape measurements in the temperature range 600K-750K.

of the spins used in the analysis was insufficient to fit the low temperature spectra. In addition, no valuable information can be gained from correlation times calculated for the high concentrations because of the numerical error, which sometimes reached as much as 70%.

5.3 Relaxation Measurements

One of the most important aspects of this work was the investigation of the spin-lattice relaxation times T_1 in BaF_2 as a function of the evolution field \vec{B}_0 (chapter 4, [95]), temperature and concentration of La^{3+} . Two different models has been applied to analyzed the data: model of Bloembergen, Purcell, Pound (BPP) and model of two different sublattices. Information gained from that could be compare with two other methods.

Typical relaxation rate dispersions are shown in the figures below. The samples were oriented with their (100)-plane parallel to \vec{B}_0 . The data for low concentration samples look almost like a single exponential decay, but detailed analysis below will show that the situation is more complicated. As far as high concentrations are concerned, more than one dynamical process could be identified in the relaxation profiles. Moreover, starting from the $\text{Ba}_{0.99}\text{La}_{0.01}\text{F}_{2.01}$ sample, some broad structure appears at frequencies around ≈ 10 MHz (figure 5.31).

As a starting point, the analysis has been performed for pure and low concentration samples since the simple picture of the dispersion data indicated one relaxation process. The next sections which follow show the procedures which had been followed in order to analyze data presented below

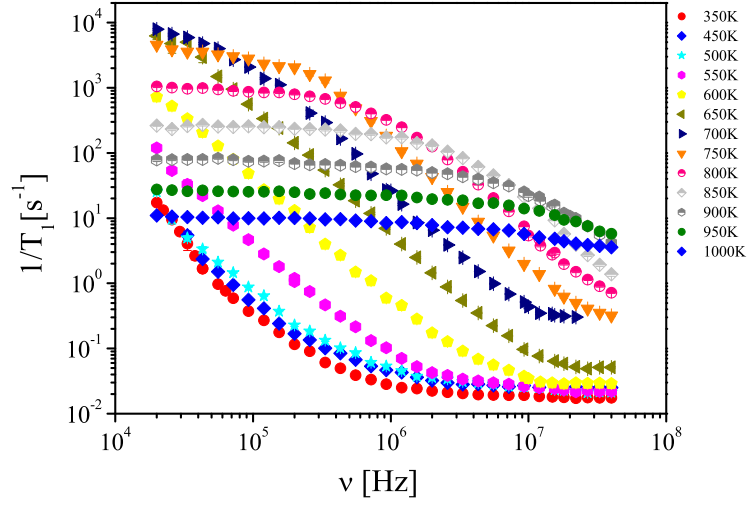


Figure 5.26: Frequency-dependent ^{19}F -relaxation measurements in pure BaF_2 in the temperature range from 300K to 1000K. Sample was oriented parallel to main magnetic field.

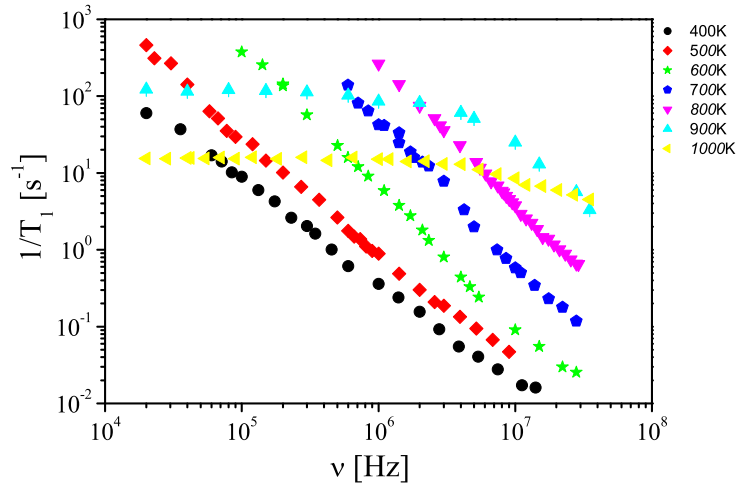


Figure 5.27: Frequency-dependent ^{19}F -relaxation measurements in $\text{Ba}_{1-x}\text{La}_x\text{F}_{2+x}$, where $x = 0.0005$ in the temperature range from 300K to 1000K. Sample was oriented parallel to main magnetic field.

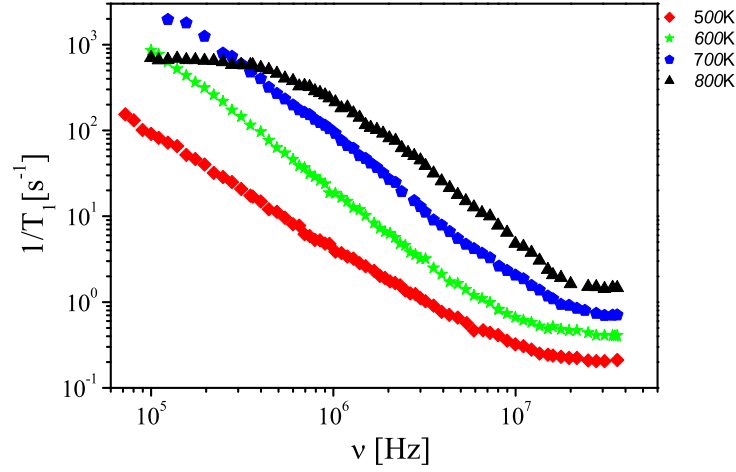


Figure 5.28: Frequency-dependent ^{19}F -relaxation measurements in $\text{Ba}_{1-x}\text{La}_x\text{F}_{2+x}$, where $x = 0.001$ in the temperature range from 300K to 1000K. Sample was oriented parallel to main magnetic field.

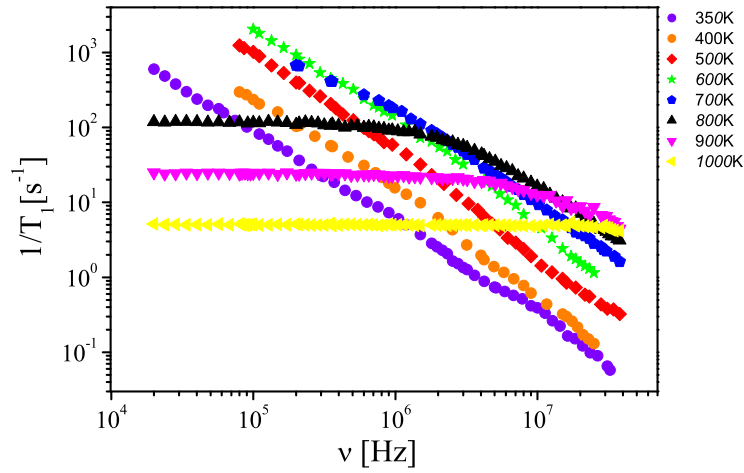


Figure 5.29: Frequency-dependent ^{19}F -relaxation measurements in $\text{Ba}_{1-x}\text{La}_x\text{F}_{2+x}$, where $x = 0.01$ in the temperature range from 300K to 1000K. Sample was oriented parallel to main magnetic field.

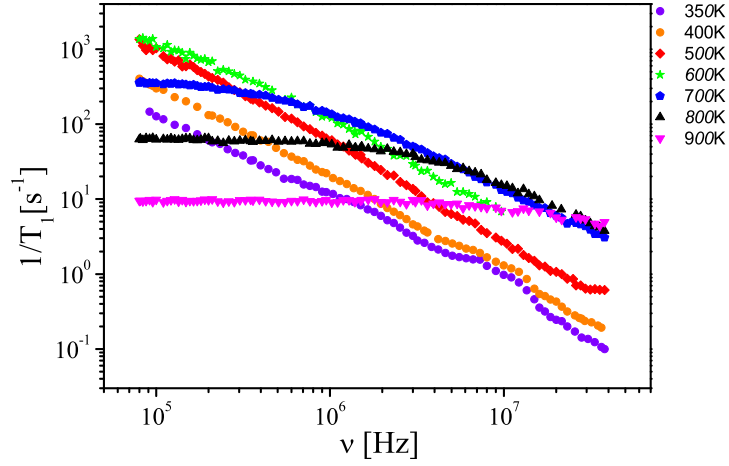


Figure 5.30: Frequency-dependent ^{19}F -relaxation measurements in $\text{Ba}_{1-x}\text{La}_x\text{F}_{2+x}$, where $x = 0.03$ in the temperature range from 300K to 1000K. Sample was oriented parallel to main magnetic field.

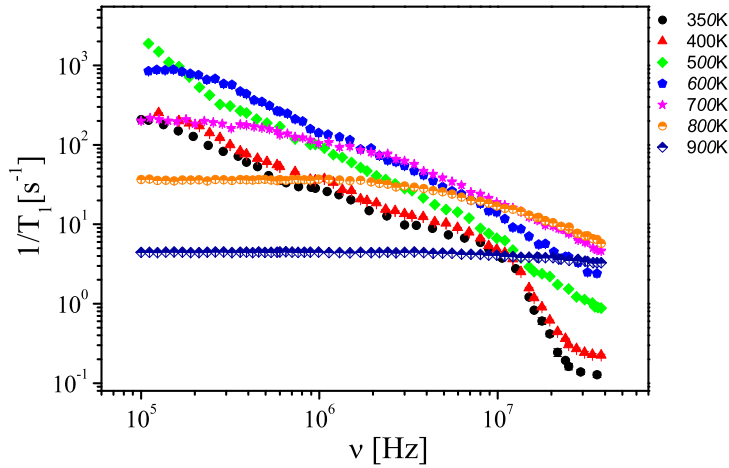


Figure 5.31: Frequency-dependent ^{19}F -relaxation measurements in $\text{Ba}_{1-x}\text{La}_x\text{F}_{2+x}$, where $x = 0.1$ in the temperature range from 300K to 1000K. Sample was oriented parallel to main magnetic field.

5.3.1 BPP Model

The simplest approach for diffusion in ordered systems is the model of Bloembergen, Purcell, and Pound, BPP-model [78], which assumes an exponential correlation function proportional to $\exp(-\frac{t}{\tau})$, where correlation time τ is the mean amount of time for one spin of a pair of interacting spins to jump. The corresponding spectral density function is then a Lorentzian function of the frequency. In the BPP-model spectral densities are connected with relaxation rates, T_1 in the following way:

$$\frac{1}{T_1} = 2 \sum_{i(J)} \left(\frac{\mu_0}{4\pi} \frac{\gamma_I^2 \hbar}{r_i^3} \right) I(I+1) [J_1(\omega_0) + 4J_2(2\omega_0)] \quad (5.5)$$

It is also assumed that τ depends on the temperature T according to the Arrhenius form $\tau = \tau_0 \exp(\frac{E}{kT})$, where E is the activation energy for the diffusive jump of a spin. The BPP model describes a situation for which the

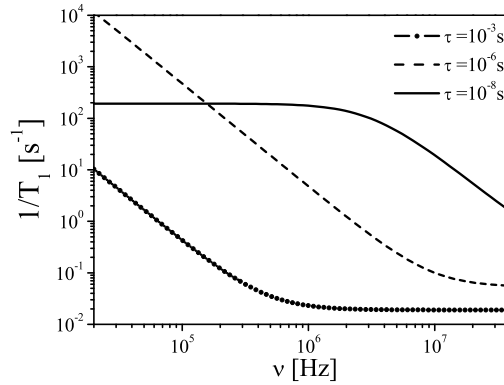


Figure 5.32: Frequency-dependent relaxation rates according to the BPP model for different τ .

correlation between a pair of the same spins (I) is completely destroyed. In other words, the motion of ions is uncorrelated. Figure 5.32 shows some theoretical curves calculated with the aid of the BPP-model for different correlation times. Using this "uncorrelated motion" model, the collected data were analyzed. In most cases, the model failed for concentrations of the admixture higher than $x=0.01$. In the case of low concentration samples, it was found that the agreement between experiment and theory is better for the temperature range 500K-800K than in the case of non-exponential correlation functions where the disagreement occurs in the

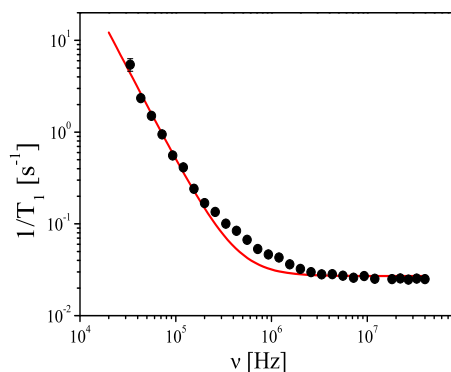


Figure 5.33: Frequency-dependent ^{19}F -relaxation measurements plus theoretical analysis in BaF_2 , at 350K.

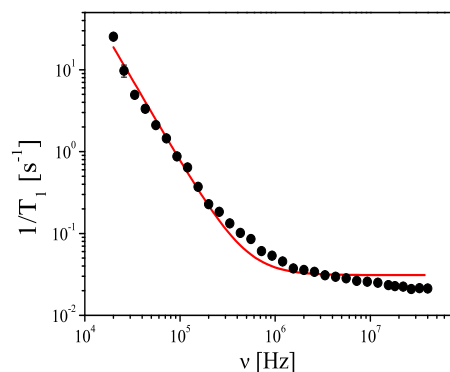


Figure 5.34: Frequency-dependent ^{19}F -relaxation measurements plus theoretical analysis in BaF_2 , at 500K.

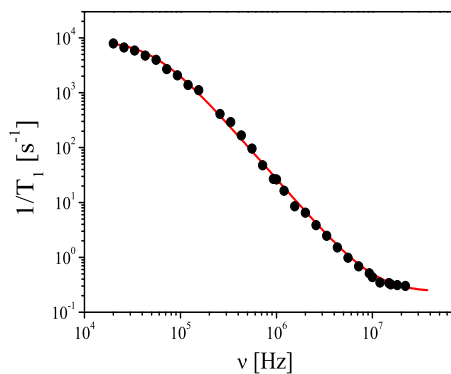


Figure 5.35: Frequency-dependent ^{19}F -relaxation measurements plus theoretical analysis in BaF_2 , at 650K.

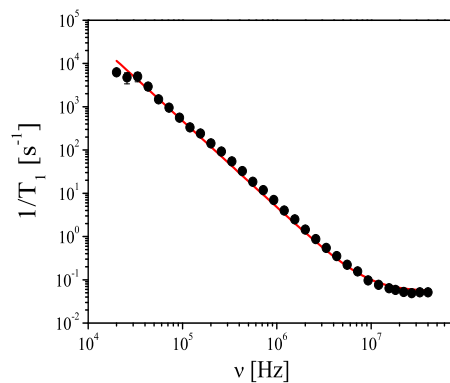


Figure 5.36: Frequency-dependent ^{19}F -relaxation measurements plus theoretical analysis in BaF_2 , at 700K.

temperature range 300-900K. Some examples are shown in figures 5.33-5.38. Three temperature ranges can be identified:

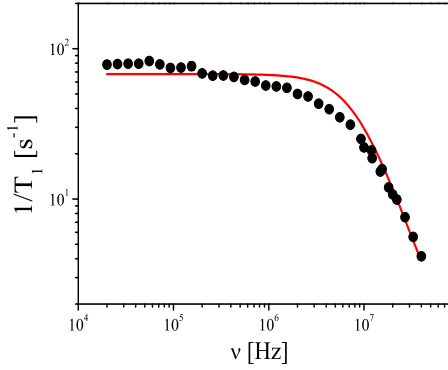


Figure 5.37: Frequency-dependent ^{19}F -relaxation measurements plus theoretical analysis in BaF_2 , at 950K.

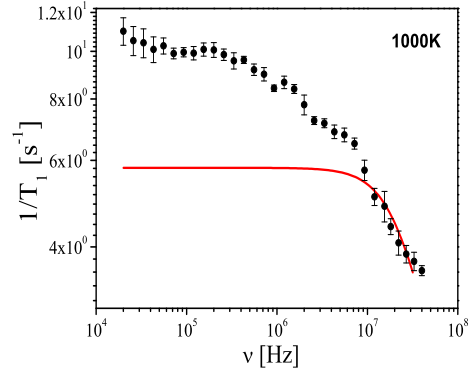


Figure 5.38: Frequency-dependent ^{19}F -relaxation measurements plus theoretical analysis in BaF_2 , at 1000K.

- Starting from room temperature up to around 500K, disagreement occurs in the frequency range 200kHz-30MHz (figure 5.33 and 5.34). The reason relies on assumptions on which the relaxation theory is based. One of them, mentioned in chapter 3, says that the dipole-dipole Hamiltonian multiplied by the correlation time τ must be smaller than one ($\hat{\mathcal{H}}_{dd}\tau > 1$). This is called the Redfield limit and is not fulfilled in this temperature range.
- The second temperature range, 500K - 800K, is in the Redfield limit [82], and the used mono-exponential function describes the experimental data very well (figure 5.43 and 5.44), which means that probably in this temperature range the motion is uncorrelated.
- Above 800K, discrepancies become more and more visible as the temperature increases (figure 5.37 and 5.38). One possible explanation concerns the phenomenological nature of the single-exponential correlation function, which in the case of translation diffusion is equal to the assumption that the dipole-dipole interaction between two spins exists only for the time τ and afterwards disappears. In other words, one spin jumps infinitely far away [21] but this is not the

case in the reality. The dipole-dipole interaction is weaker if the spin jumps further away but it still exists. This contribution, which is not considered in the BPP model, can produced similar deviations, as shown in the figure 5.38.

All obtained correlation times, along with the regions in which the relaxation theory failed (larger τ , highlighted region, top) and where the change of the dynamics (higher temperatures, highlighted region, bottom) occurs, are shown in figure 5.39.

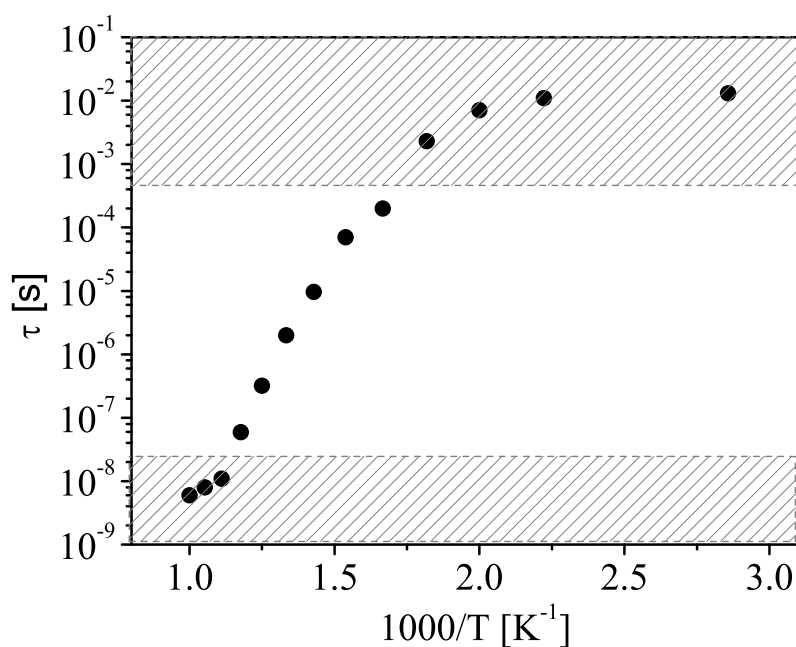


Figure 5.39: Correlation times calculated from FC NMR using the BPP-model for the BaF₂ sample (highlighted regions, see text).

5.3.2 Non-Exponential Correlation Function

The first consideration of translation diffusion described as a random walk in an isotropic diffusion model has been done by Torrey [23]. Twenty years

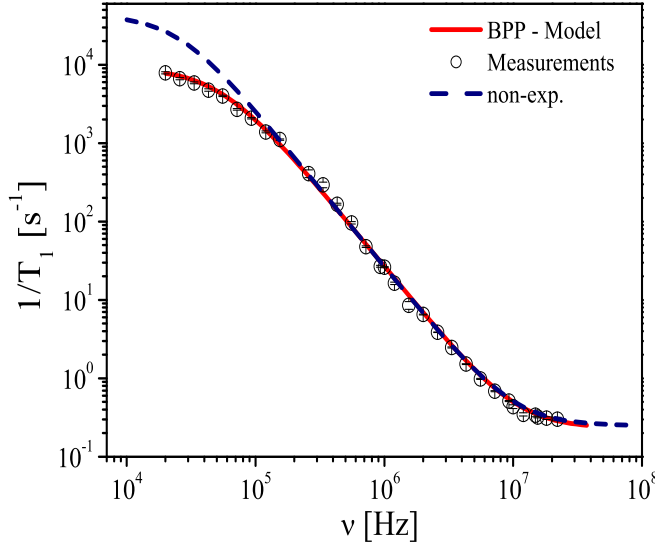


Figure 5.40: Non-exponential correlation function and relaxation profiles at 700K, BaF₂-sample.

later Wolf [24] and Sholl [25, 26] applied this model for the cubic crystal structure in which the non-exponential correlation function [27, 28] were derived:

$$\begin{aligned}
 J^p(\omega) &= \frac{2\tau}{a^6} \sum_{m=1}^x S_m^{(p)} \operatorname{Re}(u - iy)^{-m} \\
 &= \frac{2\tau}{a^6} \sum_{m=1}^x \frac{S_m^{(p)} u^m}{(u^2 + y^2)^{-m}} \sum_{j=1}^k \frac{(-1)^j m!}{(m - 2j)! (2j)!} \left(\frac{y}{u}\right)^{2j}
 \end{aligned} \tag{5.6}$$

where $u = \frac{2}{Z(0)}$, $y = \omega\tau$, k is the integer part of $\frac{m}{2}$, a is the lattice parameter and the dimensionless lattice sums $S_m^{(p)}$ are:

$$S_m^{(p)} = a^6 d_p^2 \tau^{m-1} \sum_{\alpha, \beta} \frac{Y_{2p}(\Omega_\alpha)}{r_\alpha^3} \frac{Y_{2p}^*(\Omega_\beta)}{r_\beta^3} F_m(\alpha, \beta) \tag{5.7}$$

Equation 5.6 is an exact expression for the spectral density functions in the monovacancy limit where the lattice sums $S_m^{(p)}$ are independent of $y=\omega\tau$. This result is similar to the one obtained by Torrey, e.g.,

$$J(\omega) = \frac{N}{dD} \int_0^\infty \left[J_{\frac{3}{2}}(u) \right]^2 \frac{u du}{u^4 + \frac{d^4}{4D^2} \omega^2}, \quad (5.8)$$

where D is the diffusion coefficient, d the minimal distance between the spins, N density of spins, and $J_{\frac{3}{2}}$ Bessel function rank $\frac{3}{2}$. All these models work with some assumptions for high and low frequencies. In three dimensions, the dependency of all models on low frequencies can be written:

$$J^q(\omega) = J^q(0) - A\sqrt{\omega} + \dots, \quad (5.9)$$

where A is a constant parameter depending on the model.

This behavior deviates from the BBP-Model, where $J^q(\omega) = J^q(0) - \omega^2 + \dots$. The reason is the specific form of the diffusion propagator. Mostly because of that, the non-exponential spectral density functions for cubic structure, proposed by Sholl [27, 28], have been applied and tested in combination with the experimental data.

It turned out that they do not describe the experiment very precisely. Figures 5.40 shows the deviation between theoretical non-exponential correlation functions and experimental results. One reason for this disagreement could be the monovacancy limit [27, 28], in which the relative motion of a pair of spins is controlled by the motion of a low concentration of vacancies [29].

5.3.3 Model of Two Different Sublattices

As a next step, an "expansion" of the BPP model, the model with two different species of spins derived by Solomon and Bloembergen [83], was applied to the high concentration samples. Based on this model, all relaxation data for all crystals starting from $\text{Ba}_{0.99}\text{La}_{0.01}\text{F}_{2.01}$ have been analyzed. It explicitly takes into account the different fluorine sublattices. In the complete analysis, no lanthanum spin system has been taken into account, which manifests itself as a small deviation between theoretical and experimental data, in the frequency range from 6 MHz to 12 MHz (figure 5.41).

This model consists of two coupled differential equations describing the evolution of the magnetization belonging to the F_1 and the F_2 sublattice [110]:

$$\frac{d}{dt} M_{F_1} = a_{11} M_{F_1} + a_{12} M_{F_2} \quad (5.10)$$

$$\frac{d}{dt}M_{F_2} = a_{22}M_{F_2} + a_{21}M_{F_1} \quad (5.11)$$

The coefficients depend on several spectral densities of dipolar interactions as well as the exchange lifetime τ_{12} [111]:

$$a_{11} = K \frac{3}{2} \left\{ \left[J_{11}^{(1)}(\omega_F) + 4J_{11}^{(2)}(\omega_F) \right] + \frac{1}{2} \left[J_{12}^{(0)}(\omega_F) + 3J_{12}^{(1)}(\omega_F) + 6J_{12}^{(2)}(\omega_F) \right] \right\} + \frac{1}{\tau_{12}} \frac{N_2}{N_1} \quad (5.12)$$

$$a_{12} = K \frac{N_1}{N_2} \frac{1}{2} \left[6J_{12}^{(2)}(\omega_F) - J_{12}^{(0)}(\omega_F) \right] + \frac{1}{\tau_{12}} \quad (5.13)$$

as well as two others coefficients, a_{22} and a_{21} .

The solution to these equations yields two jump rate constants, from which only the smaller one is of importance for the presented measurements. The corresponding spectral densities (chapter 3) contained in the coefficients a_{IS} with $I, S \in \{1, 2\}$ are given under the assumption of a mono-exponentially decaying correlation function by:

$$J_{I,S}^{(q)} = \sum_{i(J)} |F_i^{(q)}|^2 \frac{2\tau_{IS}}{1 + \omega^2\tau_{IS}^2} \quad (5.14)$$

with $\sum_{i(J)} |F_i^{(q)}|^2$ being the dipolar coupling strength.

The time constants τ_{IS} are derived from the jump rates of both interaction partners:

$$\frac{1}{\tau_{IS}} = \frac{1}{\tau_I} + \frac{1}{\tau_S}, \quad I, S \in \{1, 2\} \quad (5.15)$$

and in this work they will be denoted as correlation times: τ_1 , τ_2 , and τ_{12} which describe the jump rates within the F_1 -sublattice, the F_2 -sublattice and the exchange process between them, respectively.

Figures 5.41, 5.42 and 5.43 show a frequency dispersion at different temperatures over three decades and a relatively complex behavior involving several contributions to T_1 can be observed. With increasing temperature some characteristic changes occur and can be classified as following:

- From 350K to 600K, the relaxation rate decreases with increasing frequency up to 40 MHz without showing a constant level at low frequency, as expected for the slow motional limit $\omega\tau > 1$. The drop in

T_1^{-1} shifts to higher frequencies with increasing temperature, thus reflecting a thermally activated process which can be related to motion.

- At temperatures below 500K, there is an additional substructure in the T_1 -dispersion between 4 MHz-20 MHz due to polarization transfer through the ^{139}La -quadrupolar spin (chapter 3, section 3.6.2). This is perfectly reproducible and can contain valuable information about the La^{3+} local environment. Since this effect was not the main topic of this investigation, it has not been taken into account for further analysis. In an intermediate temperature regime this contribution disappears because of the faster motion of ^{19}F -ions, which are dipole-dipole coupled to La^{3+} . Nevertheless, a careful measurement of the quadrupolar dips may give more insight into the local environment of the lanthanum ions and thus possibly also into the defect structure of BaF_2 [87–91].
- Above 700K a clear plateau can be seen at low-frequencies, reflecting that the correlation times for all processes are shorter than 10^{-6}s . With the temperature increasing toward 1000K, all motional processes are in the fast limit $\omega\tau \ll 1$.

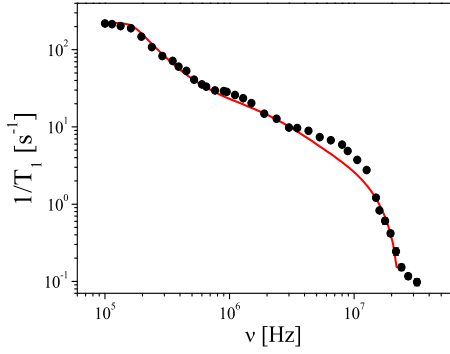


Figure 5.41: ^{19}F -Relaxation measurements plus analysis in $\text{Ba}_{0.9}\text{La}_{0.1}\text{F}_{2.1}$ at 350K.

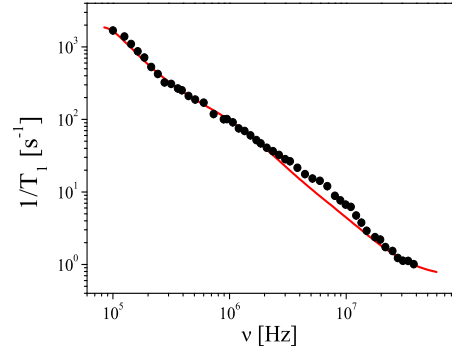


Figure 5.42: ^{19}F -Relaxation measurements plus analysis in $\text{Ba}_{0.9}\text{La}_{0.1}\text{F}_{2.1}$ at 400K.

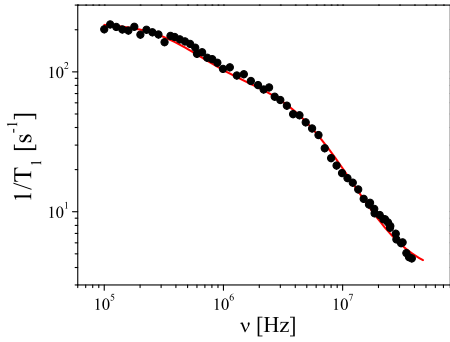


Figure 5.43: ^{19}F -Relaxation measurements plus analysis in $\text{Ba}_{0.9}\text{La}_{0.1}\text{F}_{2.1}$ at 700K.

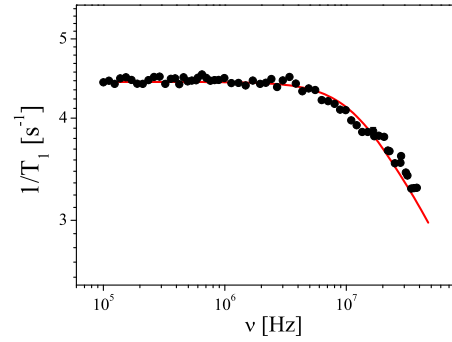


Figure 5.44: ^{19}F -Relaxation measurements plus theoretical in $\text{Ba}_{0.9}\text{La}_{0.1}\text{F}_{2.1}$ at 900K.

5.3.4 Discussion

The two models presented above, the BPP and the model of two different sublattices, describe relatively well, with some exceptions, the fluorine relaxation data for low and high concentration samples, respectively. They take into account the BaF_2 crystal structure and its defects. The results can be seen in figures 5.45 and 5.46. The relaxation behavior of $\text{Ba}_{1-x}\text{La}_x\text{F}_{2+x}$,

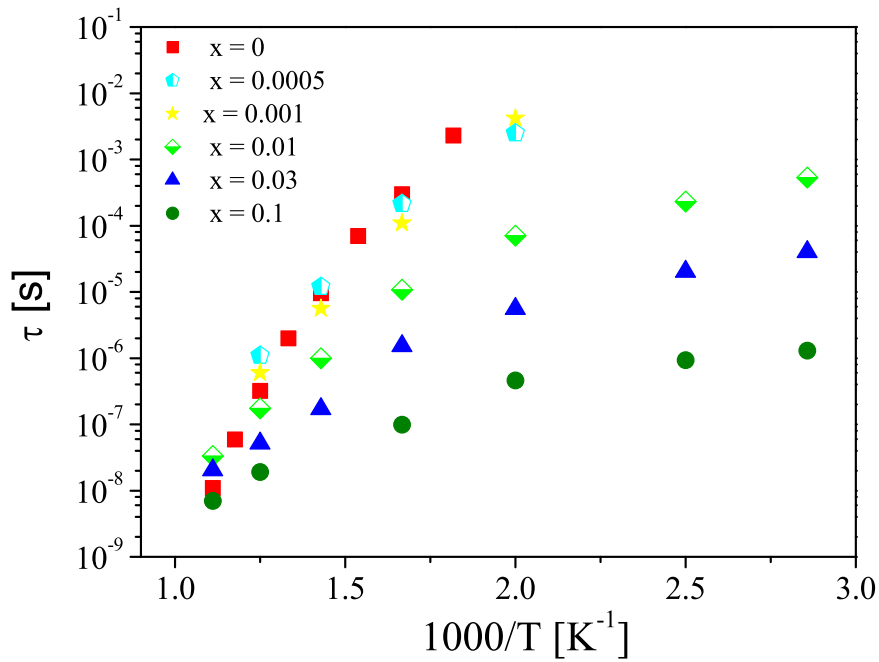


Figure 5.45: Correlation times, τ_1 calculated from FC NMR using the BPP-model and the model of two different sublattices for $\text{Ba}_{1-x}\text{La}_x\text{F}_{2+x}$, where $x = 0, 0.0005, 0.001, 0.01, 0.03, 0.1$.

where $x = 0.001, 0.003, 0.1$, can be described satisfactorily by motion within the F_1 (correlation times τ_1 , figure 5.45) and F_2 (correlation times τ_2 , figure 5.46) sublattice, except the exchange between them, where correlation times were in the order of 10 seconds which is rather doubtful. In general, the dynamic processes are at least one order of magnitude faster within the F_1 than within the F_2 , in the temperature range of 300K - 700K (figure 5.45). At higher temperatures, all correlation times are on the same slope, having the same activation energy, 0.3 eV. Furthermore, it is clear that the

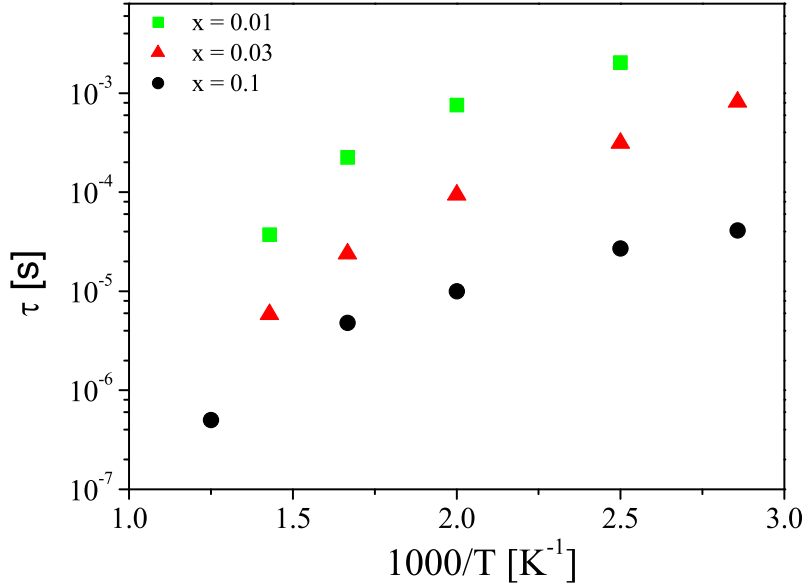


Figure 5.46: Correlation times, τ_2 calculated from FC NMR using the model of two different sublattices for $\text{Ba}_{1-x}\text{La}_x\text{F}_{2+x}$, where $x = 0.01, 0.03, 0.1$.

motion for the highly doped samples is faster than for crystals with only low doping.

As was mentioned before at temperatures below 500K and in the frequency range of 4MHz-20MHz (for ^1H frequency), an additional relaxation process occurs. It is known as a polarization transfer through the ^{139}La -quadrupolar spin system and was also found in LaF_3 [8]. A detailed analysis of this phenomenon was not the aim of this study but it should be pointed out that the static quadrupole interaction could have influenced the results for the corresponding correlation times.

5.4 Results and Discussion

This section summarizes all information about the fluorine dynamics in $\text{Ba}_{1-x}\text{La}_x\text{F}_{2+x}$ obtained by different NMR methods: magic-angle spinning, lineshape analysis, field cycling relaxometry and static field gradient measurements.

All measurements were intended to explore the macro- and micro-scale of the dynamical processes and to give some insight in the influence of La^{3+} admixtures on the BaF_2 -system.

Based on the magic angle spinning and X-ray structural results two different theoretical models have been adopted in order to obtain the correlation times from the relaxation measurement and the lineshape analysis data. In the case of the static field gradient measurements the correlation times were calculated from the isotropic Random Walk model for free-diffusion.

It should also be mentioned that the lineshape analysis data have shown strong changes of the lineshape with rising concentration of admixtures. Also, analysis of these data for low concentrations of La^{3+} was possible only in the narrow temperature range 600K-750K. The reason for was insufficient number of spins used in calculations of the broad spectra (300K-400K). With increasing concentration of La^{3+} this method reached the limits of its applicability.

The comparison of all used methods can be done by plotting, on the same graph, calculated correlation times for different temperatures and concentrations of La^{3+} . In general, this combination has allowed "looking" at dynamical processes over a wide time (eight decades) and temperature window. Results can be seen in figures 5.47-5.52.

The data for pure and low concentration ($x = 0.0005, 0.001$) of the La^{3+} (figures 5.47-5.49) measured with all techniques are on the same slope which means that dynamics of fluorine ions can be described satisfactorily by motion within the F_1 sublattice. In the case of highly doped $\text{Ba}_{1-x}\text{La}_x\text{F}_{2+x}$ samples ($x = 0.01, 0.03, 0.1$; figures 5.50-5.52) the dynamic processes are at least one order of magnitude faster within the F_1 than within the F_2 , in the temperature range: 300K - 700K. Furthermore, τ_1 correlation times from field cycling measurements are in good accordance with correlation times obtained from the static field gradient measurements which means that the motion occurring within the F_1 sublattice is responsible for the long range diffusion

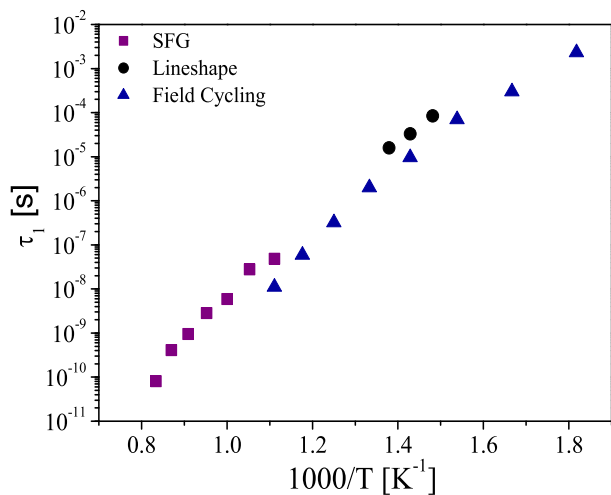


Figure 5.47: Correlation times calculated from three different NMR-methods: FC NMR, Lineshape NMR, SFG NMR, for pure BaF₂.

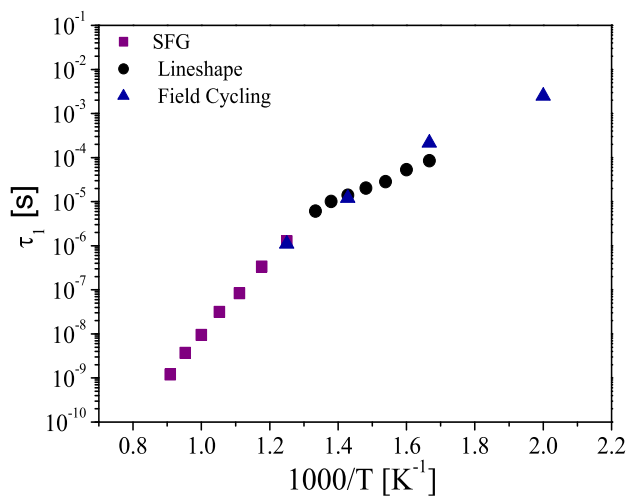


Figure 5.48: Correlation times calculated from three different NMR-methods: FC NMR, Lineshape NMR, SFG NMR, for Ba_{1-x}La_xF_{2+x} where x = 0.0005.

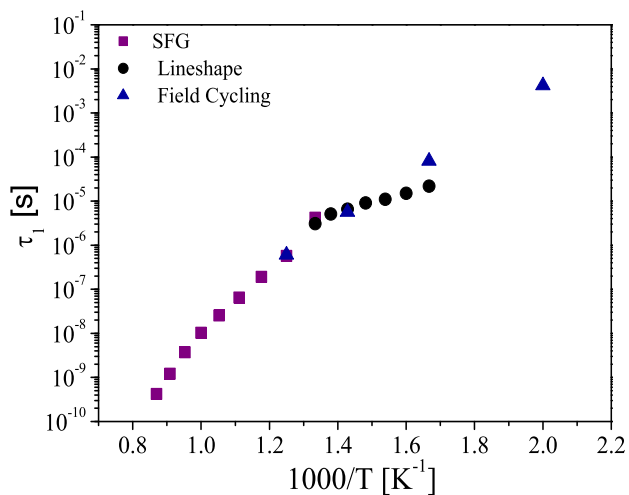


Figure 5.49: Correlation times calculated from three different NMR-methods: FC NMR, Lineshape NMR, SFG NMR, for $\text{Ba}_{1-x}\text{La}_x\text{F}_{2+x}$ where $x = 0.001$.

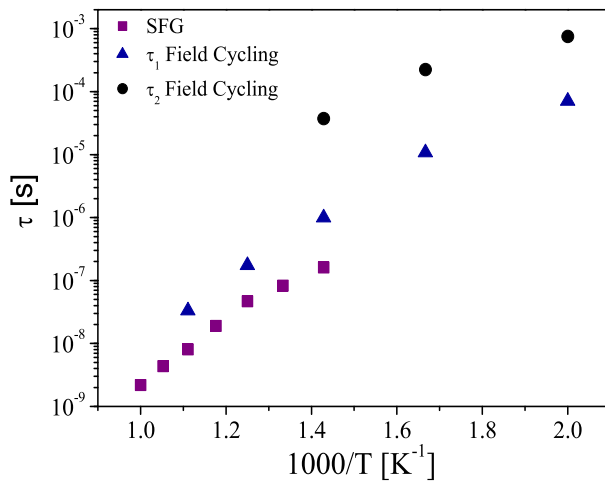


Figure 5.50: Correlation times calculated from two different NMR-methods: FC NMR, SFG NMR, for $\text{Ba}_{1-x}\text{La}_x\text{F}_{2+x}$ where $x = 0.01$.

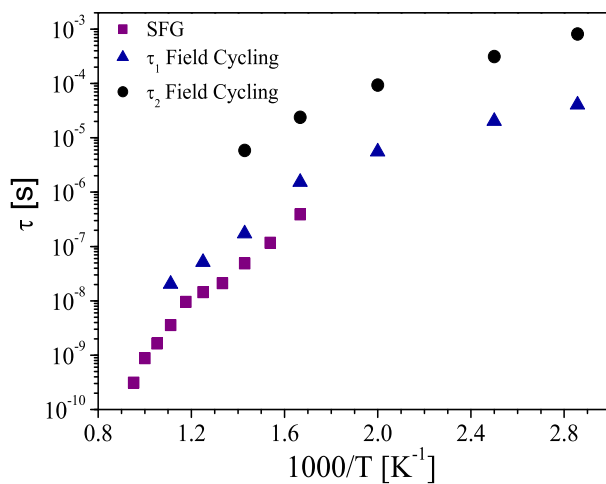


Figure 5.51: Correlation times calculated from two different NMR-methods: FC NMR, SFG NMR, for $\text{Ba}_{1-x}\text{La}_x\text{F}_{2+x}$ where $x = 0.03$.

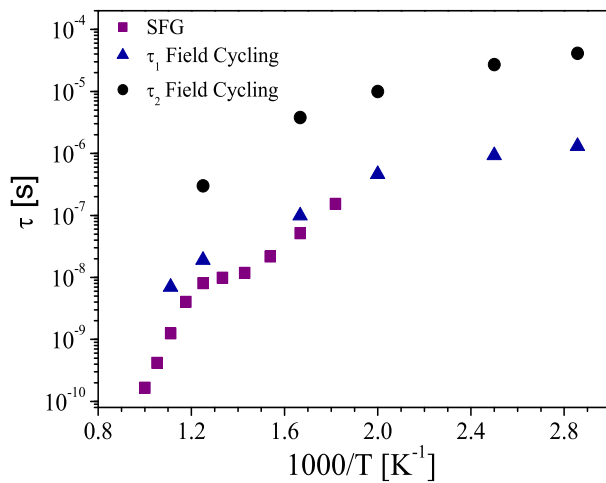


Figure 5.52: Correlation times calculated from two different NMR-methods: FC NMR, SFG NMR, for $\text{Ba}_{1-x}\text{La}_x\text{F}_{2+x}$ where $x = 0.1$.

Chapter 6

Summary

In this work the dynamics of fluorine in solid-state electrolytes having BaF_2 -structure was investigated using three different NMR-methods: field cycling relaxometry, lineshape analysis, and static field gradient NMR. For this purpose a pure BaF_2 crystal, as well as crystals doped with trivalent impurities (LaF_3), were studied as a function of temperature. The main goal of this investigation was to utilize the structure information provided by neutron scattering and MAS NMR data in order to study dynamic properties on different time and length scales with the techniques mentioned above.

Investigations of macroscopic dynamical processes performed by diffusion measurements reveal two different temperature regions, labeled I and II, with different activation energies depending on the concentration of LaF_3 . Region I, at high-temperature, contains thermally activated defects. The dynamics in this region can be described by diffusion of both, these activated and already existing defects. The low-temperature region (II), only appears at increasing admixture concentrations. It is most likely dominated by the motions of already existing defects. Another important result was observed during the high-temperature treatment of the pure and lightly doped BaF_2 samples, which influenced the dynamics. This aging effect manifests itself as a small change of the diffusion coefficient and can be explained as creation of new defects in the sample.

Information about the microscopic dynamic were obtained by the lineshape analysis. Acquired data have shown strong changes of the lineshape with rising concentration of admixtures. Using MAS NMR it was possible to identify two lines in $\text{Ba}_{0.9}\text{La}_{0.1}\text{F}_{2.1}$ having different chemical shift, and to refer them to the modified crystal structure. On this basis a model for the fluorine lineshape has been developed, taking into account three motional processes characterized by their correlation times. It includes jump

diffusion of the fluorine ions among equivalent sites within two crystallographically distinct sublattices, and inter-lattice exchange processes. The theoretical description has been based on a detailed treatment of fluorine-fluorine dipole-dipole interactions relevant for the shape of the fluorine spectra. Analysis of the lineshape data for low concentrations of admixtures revealed that motion occurs in the F_1 lattice, but with increasing concentration of La^{3+} this method reaches the limits of its applicability. Thus, it was of great interest to introduce a third technique, field cycling relaxometry.

By measuring frequency and temperature-dependent spin lattice relaxation times, it was possible to gain information about fluorine dynamics on microscopic length scales. As was done in the case of the lineshape analysis, two models were used to interpret the data, taking into account the different fluorine subsystems. The differences between the approaches consist of several modifications: on the one hand, a BPP-model for relaxation for pure and low concentration of La^{3+} was incorporated; on the other hand an "extension" to the BPP theory was used, explicitly taking into account the two different subsystems F_1 and F_2 . An attempt was also made to analyze the data for pure BaF_2 and low admixture concentration samples with a non-exponential correlation function. It turned out, at least in the temperature range of 500K-800K, that the uncorrelated motion model (BBP) is more useful to describe the data. In the case of increasing dopant concentration, two different regions could be observed for the temperature-dependent correlation times. These results were in good accordance with measurements of the self diffusion coefficient. It should also be mentioned that a second-order effect, the static quadrupole interaction, could have influenced the results for the corresponding correlation times.

Finally, it is important to emphasize the experience gained during this investigation by using different NMR methodologies. Good, fast ionic conductors inevitably exhibit large numbers of structural defects, and many dynamical processes, especially at elevated temperatures.

In the early days many different systems of known structures were studied and reported in literature. In this work, a further extension of these studies has been presented through the application of new technical developments (FC NMR). Although the information provided by NMR on the BaF_2 -system is limited, this study demonstrates the feasibility of elucidating important features of this system by exploiting element specific information concerning dynamics on different time and length scales, relative to a reference temperature or composition.

Kapitel 7

Zusammenfassung

In dieser Arbeit wurde die Fluordynamik in Festelektrolyten der BaF_2 -Struktur mittels dreier unterschiedlicher NMR-Methoden untersucht: Field Cycling Relaxometrie, Linienformanalysen und Statische Feldgradienten-NMR. Für dieses Ziel wurden sowohl reines BaF_2 als auch mit den dreiwertigen Fremdstoff La^{3+} dotierte Kristalle, als Funktion der Temperatur studiert. Das Hauptziel dieser Untersuchung war die durch Neutronenstreuung und MAS-NMR-Daten gewonnenen Strukturinformationen zu nutzen, um das dynamische Verhalten auf unterschiedlichen Zeit- und Längenskalen mittels oben genannter Techniken zu betrachten.

Aus den Diffusionsmessungen zum Studium makroskopischer Dynamik ergaben sich —in Abhängigkeit vom Dotierungsgrad mit LaF_3 — zwei Temperaturbereiche I und II mit unterschiedlichen Aktivierungsenergien. Die Diffusion mit größerer Aktivierungsenergie wurde bei allen Proben im Bereich hoher Temperaturen beobachtet, dies lässt auf das Vorhandensein thermisch aktivierter Defekte schließen. Die Dynamik kann hier als Bewegung dieser aktivierten und bereits bestehender Defekte beschrieben werden.

Der Bereich II (tiefe Temperaturen) tritt erst dann auf, wenn der Dotierungsgrad erhöht wird. Die Dynamik wird höchstwahrscheinlich von der Bewegung bereits bestehender Defekte dominiert. Eine weitere wichtige Beobachtung wurde während der Hochtemperatur-Behandlung der reinen und schwach dotierten BaF_2 -Proben gemacht: Die hohen Temperaturen riefen Änderungen in der Dynamik hervor. Dieser Alterungseffekt zeigt sich durch kleine Änderungen des Diffusionskoeffizienten und kann dadurch erklärt werden, dass bei erhöhten Temperaturen neue Defekte erzeugt werden.

Die Linienform-Analyse erfasst mikroskopische Bewegung. Die zugehörigen Messdaten zeigen starke Änderungen der Linienform mit zuneh-

mendem Dotierungsgrad. Durch die MAS NMR-Messungen war es möglich, in $\text{Ba}_{0.9}\text{La}_{0.1}\text{F}_{2.1}$ zwei Linien mit unterschiedlicher chemischer Verschiebung zu identifizieren und diese mit der modifizierten Kristallstruktur zu korrelieren. Basierend auf dieser Grundlage wurde ein Modell für die Fluor-Linienform entwickelt, das auf den drei durch ihre Korrelationszeiten charakterisierten Arten von Bewegungsprozessen beruht. Es beinhaltet die Sprungdiffusion der Fluor-Ionen zwischen äquivalenten Gitterplätzen innerhalb der beiden kristallographischen Untergitter, sowie Austauschprozesse zwischen den beiden Gittern. Die theoretische Auswertung basiert auf einer detaillierten Betrachtung der Fluor-Fluor Dipol-Dipol-Wechselwirkungen, die für die Linienform der Fluor-Spektren verantwortlich sind. Analysen der Linienform-Messergebnisse für niedrige Dotierungsgrade haben gezeigt, dass im F_1 -Gitter Bewegung auftritt. Allerdings stößt diese Methode mit zunehmender Konzentration von La^{3+} an die Grenzen ihrer Anwendbarkeit, daher war es von großem Interesse, eine dritte Messmethode, nämlich die Fieldcycling-Relaxometrie, einzubeziehen.

Durch die Messung frequenz- und temperaturabhängiger Spin-Gitter-Relaxationszeiten war es möglich, die Fluor-Dynamik auf mikroskopischer Skala aufzuklären. Analog zur Linienformanalyse wurden zur Interpretation der Daten zwei Modelle herangezogen, die die unterschiedlichen Fluor-Subsysteme in Betracht ziehen. Für reines BaF_2 und bei niedrigen Konzentrationen von La^{3+} wurde das BPP-Relaxationsmodell angewendet, bei hohen Konzentrationen empfiehlt sich hingegen eine Erweiterung der BPP-Theorie, die die beiden Subsysteme F_1 und F_2 explizit berücksichtigt. Diese Modelle unkorrelierter Bewegung zeigen insbesondere im Temperaturbereich von 500K-800K eine sehr gute Übereinstimmung mit den Daten. Weiterhin wurde der Versuch unternommen, die Daten für reines BaF_2 und niedrige La^{3+} -Dotierungsgrade anhand einer nichtexponentiellen Korrelationsfunktion zu analysieren. Dieser Ansatz erwies sich im gesamten Temperaturbereich als ungeeignet zur Beschreibung der Messdaten. Bei den nach der BPP-Theorie berechneten Korrelationszeiten konnten mit zunehmendem Dotierungsgrad zwei unterschiedliche Temperaturbereiche beobachtet werden. Dieses aus den Fieldcycling-Messungen gewonnene Resultat zeigt eine gute Übereinstimmung mit den Ergebnissen zum Selbstdiffusionskoeffizienten. Weiterhin soll hier erwähnt werden, dass ein Effekt zweiter Ordnung, die statische Quadrupol-Wechselwirkung, die Werte der Fieldcycling-Korrelationszeiten nicht unerheblich beeinflussen haben könnte.

In den Anfängen der NMR-Untersuchungen wurden verschiedene Systeme bekannter Strukturen untersucht und die Resultate in der Literatur

festgehalten. In dieser Arbeit werden solche Studien durch das Einbeziehen neuer technischer Entwicklungen (Fieldcycling-NMR) erweitert. Obwohl der aus NMR-Messungen erhältliche Informationsgehalt über das BaF₂-System begrenzt ist, hat diese Studie gezeigt, dass die Aufklärung wichtiger Merkmale dieses Systems durch die Nutzung elementspezifischer Informationen bezüglich der Dynamik auf unterschiedlichen Zeit- und Längenskalen möglich wird.

Bibliography

- [1] M. Faraday, Experimental Researches in Electricity, *Philosophical Transactions of the Royal Society of London*, **128**, 79-168 (1838).
- [2] M. Faraday, Experimental Untersuchungen über Elektrizität (Springer Verlag, Berlin, 1889).
- [3] C.E. Derrington, M. O'Keeffe, Anion conductivity and disorder in lead fluoride, *Nature (Physical Science)*, **246**, 44 (1973).
- [4] R. Benz, Electrical conductivity of lead(II) fluoride, *Zeitschrift fuer Physikalische Chemie*, **95**, 25 (1975).
- [5] J.B. Goodenough, Fast ionic conduction in solids, *Proc. R. Soc. Lond. A*, **393**, 215 (1984).
- [6] L.X. Zhou, J.R. Hardy, H.Z. Cao, Dynamical simulations of superion-icity in alkaline-earth halides, *Solid State Comm.*, **98**, 341 (1996).
- [7] S. Hull, Superionics: crystal structures and conduction processes, *Re-ports on Progress in Physics*, **67**, 1233 (2004).
- [8] O. Lips, *NMR-Untersuchungen an schnellen Ionenleitern vom LaF_3 -Typ*, Shaker Verlag (2004).
- [9] K.E.D. Wapenaar, J.L. van Koesveld, J. Schoonman, Conductivity en-hancement in fluorite-structured $\text{Ba}_{1-x}\text{La}_x\text{F}_{2+x}$ solid solutions, *Solid State Ionics*, **2**, 145 (1981).
- [10] R.A. Panhuyzen, A.F.M. Arts, K.E.D. Wapenaar, J. Schoonman, ^{19}F NMR and conductivity of $\text{Ba}_{1-x}\text{La}_x\text{F}_{2+x}$ solid solutions, *Solid State Ionics*, **5**, 641 (1981).
- [11] F. Kadlec, F. Moussa, P. Simon, G. Gruener, B.P. Sobolev, Defects and lattice distortions in the superionic conductor $\text{Ba}_{0.84}\text{La}_{0.16}\text{F}_{2.16}$, *Mater. Sci. and Engineering*, **B57**, 234 (1999).

BIBLIOGRAPHY

- [12] M.M. Sinha, Phonons in mixed superionic fluorites $\text{Ba}_{1-x}\text{La}_x\text{F}_{2+x}$, *Bull. Mater. Sci.*, **25**, 459, (2002).
- [13] J.B. Boyce, B.A. Huberman, Superionic conductors: Transitions, structures, dynamics, *Physics Reports*, **51**, 189 (1979).
- [14] S. Chandra, Superionic Solids, *Amsterdam: North-Holland* (1981).
- [15] A.R. West, Solid Electrolytes and Mixed Ionic-Electronic Conductors: An Applications Overview, *J. Mater. Chem.*, **1**, 157 (1991).
- [16] C.R.A. Catlow, J.D. Comins, F.A. Germano, R.T. Harley, W. Hayes, I.B. Owen, Studies of effects of trivalent impurity ions on the transition to the superionic state of fluorites, *J.Phys.C: Solid State Phys.*, **14**, 329 (1981).
- [17] W.H. Flygare, R.A. Huggins, Theory of ionic transport in crystallographic tunnels, *J.Phys.Chem. Solids*, **34**, 1199 (1973).
- [18] A.R. West, Basic Solid State Chemistry and Its Applications, John Wiley, Chichester, 80 (1991) and references therein.
- [19] A. Rahman, Particle motions in superionic conductors, *J.Chem. Phys.*, **65**, 4845 (1976).
- [20] S.H.N. Wei, D.C Ailion, Nuclear magnetic resonance study of the diffusion of bound and free fluorine interstitials in alkaline-earth fluorides doped with trivalent impurities, *Phys. Rev. B*, **19**, 4470 (1979).
- [21] C.A. Sholl, Nuclear spin relaxation by translational diffusion in solids: IX. Orientation dependence of single crystal relaxation rates, *J.Phys.C: Solid State Phys.*, **19**, 2547 (1986).
- [22] C.A. Sholl, Nuclear spin relaxation by translational diffusion in liquids and solids: high- and low-frequency limits, *J.Phys.C: Solid State Phys.*, **14**, 447, (1981).
- [23] H.C. Torrey, Nuclear spin relaxation by translational diffusion, *Phys Rev.*, **92**, 962 (1953).
- [24] D. Wolf, High-field nuclear spin relaxation by a random-walk diffusion mechanism in single crystal, *J. of Mag. Res.*, **17**, 1 (1975).
- [25] C.A. Sholl, Nuclear spin relaxation by translational diffusion in solids, *J.Phys.C: Solid State Phys.*, **7**, 3378 (1974).

-
- [26] C.A. Sholl, Nuclear spin relaxation by translational diffusion in solids: II. Diffusion in BCC and SC lattices, *J.Phys.C: Solid State Phys.*, **8**, 1737 (1975).
- [27] C.A. Sholl, Nuclear spin relaxation by translational diffusion in solids: VI. Monovacancy limit, *J.Phys.C: Solid State Phys.*, **14**, 1479 (1981).
- [28] I.R. MacGillivray, C.A. Sholl, Nuclear spin relaxation by translational diffusion in solids: XI. Evaluation of the spectral density functions in the monovacancy limit, *J.Phys.C: Solid State Phys.*, **19**, 4771 (1986).
- [29] C.A. Sholl, Relative displacements of a pair of atoms for the vacancy mechanism from random walk theory, *J.Phys.C: Solid State Phys.*, **15**, 1177 (1982).
- [30] W.K. Rhim, A. Pines, J.S. Waugh, Time-Reversal Experiments in Dipolar-Coupled Spin Systems, *Phys. Rev. B*, **3**, 684 (1971).
- [31] M. Aniya, A chemical approach for the microscopic mechanisms of fast ion transport in solids, *Solid State Ionics*, **50**, 125 (1992).
- [32] A. Collin, G. Denes, D. Le Roux, M.C. Madamba, J.M. Parris, A. Salaun, Understanding the phase transitions and texture in superionic PbSnF₄. The key to reproducible properties, *The International Journal of Inorganic Materials*, **1**, 289 (1999).
- [33] V. Murin, O.V. Glumov, W. Gunßer, High pressure studies of superionic conductors with predominant anionic conductivity, *Ionics*, **1**, 274 (1995).
- [34] O.K. Nikolskaya, L.N. Demianets, N.I. Sorokin, Fluoride single crystals: Hydrothermal synthesis and electric conductivity of α -PbF₂, α -PbSnF₄, CdF₂, *High Pressure Research*, **20**, 195 (2001).
- [35] B.A. Huberman, Cooperative Phenomena in Solid Electrolytes, *Phys Rev. Lett.*, **32**, 1000 (1974).
- [36] A. Jost, K. Funke, Measurements of the ionic conductivity of a-silver iodide crystals in the frequency from 10¹⁰ to 10¹³ Hz using microwave techniques and Fourier spectrophotometry, *Ber. Bunsenges. Phys. Chem.*, **75**, 436 (1971).
- [37] D.S. Robertson, Crystal growth from aqueous solution by the Bridgman method, *J.Phys. D: Appl.Phys.*, **5**, 604 (1972).

BIBLIOGRAPHY

- [38] B.P. Sobolev, N.L. Tkachenko, Phase diagrams of $\text{BaF}_2\text{-(Y,Ln)F}_3$ systems, *J.of the Less-Common Metals*, **85**, 155 (1982).
- [39] B.P. Sobolev, P.P. Fedorov, Phase diagrams of $\text{CaF}_2\text{-(Y,Ln)F}_3$ systems, *J.of the Less-Common Metals*, **60**, 33 (1978).
- [40] V.B. Alexandrov, L.S. Garashina, *Dokl. Akad. Nauk S.S.S.R.*, **89**, 307 (1969).
- [41] Y. Mita, E. Nagasawa, K. Shiroki, Y. Ohno, T. Matsubara, Efficient infrared-to-visible conversion in BaY_2F_8 : Yb, Er crystal by confinement of excitation energy *Appl. Phys. Lett.*, **23**, 173 (1973).
- [42] S.N. Valkovsky, E.M. Nadgornyi, E.A. Simun, V.K. Karpovich, *Fiz. Tverd. Tela.*, **15**, 570 (1973).
- [43] T. Takahashi, H. Iwahara, T. Ishikawa, Ionic Conductivity of Doped Cerium Trifluoride, *J. Electrochem. Soc.*, **124**, 280 (1977).
- [44] V.N. Morozov, L.N. Tretyakova, P.P. Fedorov, B.P. Sobolev, *Izv. Akad. Nauk S.S.S.R. Neorg. Mater.*, **15**, 2238 (1979).
- [45] T.S. Bessonova, Sh.A. Vachidov, B.P. Sobolev, G.A. Tavshunsky, Ya. Rustamov, Abstracts 4th All-Union Conf. on Radiation Physics and Chemistry of Ionic Crystals, Riga, **Part II**, 247 (1978).
- [46] B.P. Sobolev, N.L. Tkachenko, V.S. Sidorov, P.P. Fedorov, D.D. Ikrami, Abstracts 5th All-Union Conf. on Crystal Growth, Tbilisi, **Part II**, 25 (1977).
- [47] A.K. Cheetham, B.E.F. Fender, D. Steele, R.I. Taylor, B.T.M. Willis, Defect structure of fluorite compounds containing excess anions, *Solid State Commun.*, **8**, 171 (1970).
- [48] V.C. Ovsyankin, P.P. Feofilov, *Opt. Spektrosk.*, **31**, 944 (1971).
- [49] B.P. Sobolev, V.B. Alexandrov, P.P. Fedorov, K.B. Seiranian, N.L. Tkachenko, *Kristallografiya*, **21**, 96 (1976).
- [50] H. Hahn, W. Seeman, H.L. Kohn, Zur Mischkristallbildung in den Systemen CaF_2/YF_3 , $\text{CaF}_2/\text{LaF}_3$, $\text{SrF}_2/\text{LaF}_3$ und $\text{BaF}_2/\text{LaF}_3$ *Z. Anorg. Chem.*, **369**, 48 (1969).
- [51] N.G. Gogadze, I.G. Ippolitov, B.M. Zhigarnovskii, *Zh. Neorg. Khim.*, **17**, 2588 (1972).

- [52] W. Bollmann, Ionic Conductivity of pure and doped BaF₂ crystals, *Phys. Stat. Sol.*, **18**, 313 (1973).
- [53] D. Klimm, R. Uecker, P. Reiche, Melting behavior and growth of colquiriite laser crystals, *Cryst. Res. Technol.*, **40**, 352 (2005).
- [54] A.K. Cheetham, B.E.F. Fender, M.J. Cooper, Defect structure of calcium fluoride containing excess anions: I. Bragg scattering, *J. Phys. C: Solid State Phys.*, **4**, 3107 (1971).
- [55] J.K. Kjems, N.H. Andersen, J. Schoonman, Structure and dynamics of disordered solids: a neutron scattering study of Ba_{1-x}La_xF_{2+x}, *Phys. B*, **120**, 357 (1983).
- [56] S. Hull, C.C. Wilson, The defect structure of anion-excess (Ca_{1-x}Y_x)F_{2+x} with x = 0.06, *J. Solid Stat Chem.*, **100**, 101 (1992).
- [57] J.P. Laval, B. Frit, Defect structure of anion-excess fluorite-related (Ca_{1-x}Y_x)F_{2+x} solid solution, *J. Solid Stat Chem.*, **49**, 237 (1983).
- [58] J.P. Laval, A. Abaouz, B. Frit, Short-range order in the (Ca_{1-x}Y_x)F_{2+x} solid solution: 1:0:3 or 1:0:4 clusters, *J. Solid Stat Chem.*, **81**, 271 (1989).
- [59] J.P. Laval, A. Abaouz, B. Frit, Short-range order in the anion-excess fluorite-related (Ca_{0.68}Ln_{0.32})F_{2.32} solid solution: EXAFS study of the Ln³⁺ environment, *J. Solid Stat Chem.*, **85**, 133 (1990).
- [60] J. Vogt, J. Henning, H. Weiss, The structure of CaF₂(111) and BaF₂(111) single crystal surfaces: A tensor low energy electron diffraction study, *Surface Science*, **578**, 57 (2005).
- [61] C.R.A. Catlow, W. Hayes, The nature of disorder in the superionic state of fluorites, *J. Phys. C: Solid State Phys.*, **15**, L9 (1982).
- [62] N.H. Andersen, K.N. Clausen, J.K. Kjems, J. Schoonman, A Study of the disorder in heavily doped Ba_{1-x}La_xF_{2+x} by neutron scattering, ionic conductivity and specific heat measurements, *J. Phys. C: Solid State Phys.*, **19**, 2377 (1986).
- [63] D.A. Keen, S. Hull, W. Hayes, N.J.G. Gardner, Structural Evidence for a Fast-Ion Transition in the High-Pressure Rocksalt Phase of Silver Iodide, *Phys. Rev. Lett.*, **77**, 4914 (1996).

BIBLIOGRAPHY

- [64] S. Hull, D.A. Keen, Effect of hydrostatic pressure on the crystal structure and superionic behavior of lead (II) fluoride, *Phys. Rev. B*, **58**, 14837, (1998).
- [65] D.A. Keen, S. Hull, A.C. Barnes, P. Berastegui, W.A. Crichton, P.A. Madden, M.G. Tucker, and M. Wilson, Nature of the superionic transition in Ag^+ and Cu^+ halides, *Phys. Rev. B*, **68**, 014117 (2003).
- [66] D.R. Figueroa, A.V. Chadwick, J.H. Strange, NMR relaxation, ionic conductivity and the self-diffusion process in barium fluoride, *J. Phys. C: Solid State Phys.*, **11**, 55, (1978).
- [67] L. Filder, NASA reports TN D-3346 (1968).
- [68] E. Barsis, A. Taylor, F^- Vacancy Conductivity in BaF_2 Crystals, *J. Chem. Phys.*, **48**, 4357 (1968).
- [69] C.R.A. Catlow, M.J. Norgett, T.A. Ross, Ion transport and interatomic potentials in the alkaline-earth fluoride crystals, *J. Phys. C: Solid State Phys.*, **10**, 1627 (1977).
- [70] G.E. Murch, The Haven ratio in fast ionic conductors, *Solid State Ionics*, **7**, 177 (1982).
- [71] A. Abragam, Principles of Nuclear Magnetism, Oxford University Press, Oxford (1961).
- [72] C.P. Slichter, Principles of Magnetic Resonance, Springer Verlag, Berlin (1992).
- [73] J. McConnell, The theory of nuclear magnetic relaxation in liquids, Cambridge University Press, Cambridge (1987).
- [74] R.R. Ernst, G. Bodenhausen, A. Wokaun, Principles of nuclear magnetic resonance in one and two dimensions, Clarendon Press, Oxford (1994).
- [75] R. Kimmich, NMR-Tomography, Diffusometry, Relaxometry, Springer Verlag Berlin (1997).
- [76] M. H. Levitt, Spin Dynamics, Chichester, Wiley (2001).
- [77] M. Mehring, High resolution NMR in solids, Springer, Berlin-Heidelberg (1983).

-
- [78] N. Bloembergen, E.M. Purcell, R.V. Pound, Relaxation effects in nuclear magnetic resonance absorption, *Phys. Rev.*, **73**, 679 (1948).
- [79] M. Goldman, Formal theory of spin-lattice relaxation, *J. Magn. Reson.*, **149**, 160 (2001).
- [80] K. Blum, Density matrix theory and applications, Plenum Press, New York (1989).
- [81] A.G. Redfield, On the theory of relaxation processes, *IBM J. Res. Dev.* **1**, 19 (1957).
- [82] A.G. Redfield, The theory of relaxation processes, *Adv. Magn. Reson.*, **1**, 1 (1965).
- [83] I. Solomon, N. Bloembergen, Nuclear magnetic interactions in the HF molecule, *J. Chem. Phys.*, **25**, 261 (1956).
- [84] N. Bloembergen, L.O. Morgan, Proton relaxation times in paramagnetic solutions: Effects of electron spin relaxation, *J. Chem. Phys.* **34**, 842 (1961).
- [85] R.K. Wangsness, F. Bloch, The dynamic theory of nuclear induction, *Phys. Rev.*, **89**, 728 (1953).
- [86] R. Kubo, Stochastic Liouville equations, *J. Math. Phys.*, **4**, 174 (1963).
- [87] D. Kruk, O. Lips, Field dependent nuclear relaxation of spins $\frac{1}{2}$ induced by dipole-dipole couplings to quadrupole spins: LaF_3 crystals as an example, *J. Magn. Reson.*, **179**, 250 (2006).
- [88] D. Kruk, O. Lips, Evolution of solid state system containing mutually coupled dipolar and quadrupole spins: Perturbation treatment *Solid State Nuclear Magnetic Resonance*, **28**, 180 (2005).
- [89] D. Kruk, T. Nilsson, J. Kowalewski, Nuclear spin relaxation in paramagnetic systems with zero-field splitting and arbitrary electron spin *Phys. Chem. Chem. Phys.*, **3**, 4907 (2001).
- [90] D. Kruk, J. Kowalewski, Nuclear spin relaxation in paramagnetic systems $S \geq 1$ under fast rotation conditions *J. Magn. Reson.*, **162**, 229 (2003).
- [91] J. Kowalewski, D. Kruk, G. Parigi, NMR Relaxation in Solution of Paramagnetic Complexes: Recent Theoretical Progress for $S \geq 1$, *Adv. Inorg. Chem.*, **41** (2005).

BIBLIOGRAPHY

- [92] D. Kruk, *Theory of Evolution and Relaxation in Multi-Spin Systems* *Theory of Evolution and Relaxation in Multi-Spin Systems*, Arima Publishing (2007).
- [93] A.F. Privalov, O. Lips, F. Fujara, Dynamic processes in the superionic conductor LaF_3 at high temperatures as studied by spin-lattice relaxation dispersion, *J. Phys.: Condens. Matter* **14**, 4515 (2002).
- [94] O. Lips, A.F. Privalov, S.V. Dvinskikh, F. Fujara, Magnet design with high B_0 homogeneity for fast-field-cycling NMR applications, *J. Mag. Res.*, **149**, 22 (2001).
- [95] F. Noack, NMR-Field Cycling Spectroscopy: Principles and Applications, *Progress in NMR Spectroscopy*, **18**, 171 (1986).
- [96] A.F. Privalov, O. Lips, Low-cost high-temperature NMR probe head *Appl. Magn. Reson.*, **22**, 597 (2002).
- [97] H. Stork, Aufbau und Erprobung eines mechanischen Feldzyklus-NMR-Spektrometers, Diplomarbeit, TU Darmstadt (2002).
- [98] L. Chen, Z. Weng, L. Goh, M. Garland, An efficient algorithm for automatic phase correction of NMR spectra based on entropy minimization, *J. Mag. Res.*, **158**, 164 (2002).
- [99] P. Koehl, Linear prediction spectral analysis of NMR data, *Progress in NMR Spectroscopy*, **34**, 257 (1999).
- [100] J.S. Waugh, L.M. Huber, U. Haeberlen, Approach to high-resolution nmr in solids, *Phys. Rev. Lett.*, **20**, 180 (1968).
- [101] N.F. Ramsey, R.V. Pound, Nuclear Audiofrequency Spectroscopy by Resonant Heating of the Nuclear Spin System, *Phys. Rev.*, **81**, 278 (1950).
- [102] R.V. Pound, Nuclear Spin Relaxation Times in Single Crystals of LiF, *Phys. Rev.*, **81**, 156 (1951).
- [103] R. Hauser, F.Z. Noack, Kernmagnetische Relaxation und Korrelation in Zwei-Spin-Systemen *Z.Phys.*, **182**, 93 (1964).
- [104] E.L. Hahn, Spin Echoes, *Phys. Rev.*, **80**, 580 (1950).
- [105] D.W. McCall, D.C. Douglass, E.W. Anderson, Self-diffusion studies by means of NMR spin-echo techniques, *Ber. Bunsenges. Physik Chem.*, **67**, 336 (1963).

- [106] G. Fleischer, F. Fujara, NMR as a generalized incoherent scattering experiment, *NMR Basics Principles Progress*, **30**, 159 (1994).
- [107] B. Geil, Measurement of translational molecular diffusion using ultrahigh magnetic field gradient NMR, *Concepts in Magnetic Resonance*, **10**, 299 (1998).
- [108] K.E.D. Wapenaar, H.G. Koekkoek, Low-temperature ionic conductivity and dielectric relaxation phenomena in fluorite-type solid solutions, *Solid State Ionics*, **7**, 225 (1982).
- [109] F. Wang, C.P. Grey, Probing the defect structure of anion-excess $\text{Ca}_{1-x}\text{Y}_x\text{F}_{2+x}$ ($x = 0.03, 0.32$) with high-resolution ^{19}F Magic-Angle-Spinning NMR Spectroscopy, *Chem. Matter.*, **10**, 3081 (1998).
- [110] G.A. Jaroszkiewicz, J.H. Strange, Motion on inequivalent lattice sites: NMR theory and application to LaF_3 , *J.Phys.C: Solid State Phys.*, **18**, 2331 (1985).
- [111] A.F. Aalders, A.F.M. Arts, H.V. de Wijn, Vacancy distribution and ionic motion in LaF_3 studied by ^{19}F NMR, *Phys. Rev. B*, **32**, 5412 (1985).
- [112] J. Maier, Festkörper - Fehler und Funktion. Prinzipien der Physikalischen Festkörperchemie, B.G. Teubner, Stuttgart (2000).
- [113] A.B. Lidiard, Encyclopedia of Physics, edited by S. Flügge, Springer, Berlin (1957).
- [114] J. Corish, P.W.M. Jacobs, S. Radhakrishna, Surface and Defect Properties of Solids vol 6, London: Chemical Society (1977).
- [115] J. Crank, The Mathematics of Diffusion, Clarendon Press, Oxford (1975).
- [116] J.B. Boyce, B.A. Huberman, Superionic Conductors: Transitions, Structures, Dynamics, *Phys. Rep.*, **51**, 189 (1979).
- [117] F. Bloch, Nuclear Introduction, *Phys. Rev.*, **70**, 460 (1946).

BIBLIOGRAPHY

List of Figures

2.1	Arrhenius plot of conductivity	5
2.2	Diffusion coefficients for PbSnF_4	7
2.3	A schematic representation of different dynamical processes	11
2.4	Equilibrium activities a at 800°	14
2.5	Surface of the $\text{Ba}_{0.55}\text{La}_{0.45}\text{F}_{2.45}$	15
2.6	Twin crystal, $\text{Ba}_{0.55}\text{La}_{0.45}\text{F}_{2.45}$	15
2.7	Magic angle spinning data for $\text{Ba}_{0.7}\text{La}_{0.3}\text{F}_{2.3}$	16
2.8	Neutron Tomography of $\text{Ba}_{0.7}\text{La}_{0.3}\text{F}_{2.3}$	17
2.9	Phase diagram for $\text{BaF}_2+\text{LaF}_3$ -system.	18
2.10	Cubic structure	20
2.11	Cubic structure, different view.	20
2.12	Contour map of the diffuse elastic scattering	21
2.13	Extrinsic defect clusters	22
3.1	Energy levels of spin I	30
3.2	Energy levels and spin flipping	37
3.3	The distribution of charge	38
3.4	Magnetization against frequency	42
3.5	Fluorine T_1 relaxation profiles	43
3.6	Fluorine T_1 relaxation profiles	44
3.7	Fluorine T_1 relaxation profiles	45
3.8	Fluorine T_1 relaxation profiles	46
4.1	A schematic of the Lineshape spectrometer	48
4.2	A schematic of the RF transmitter	49
4.3	A schematic of the receiver section	50
4.4	The one-pulse sequence	51
4.5	A schematic of the MAS experiment	53
4.6	The effect of slow speed magic-angle spinning	54
4.7	The formation of rotor echoes	55
4.8	Multiple pulse sequence	56

LIST OF FIGURES

4.9	FC-NMR relaxometry: cycle of the main magnetic field B_0	63
4.10	Schematic of high-temperature probe head.	64
4.11	Furnace with Pt-wire and current plugs	65
4.12	Gradient profiles of the magnetic field in a Oxford magnet.	66
4.13	Pulse sequence for the Hahn echo	67
4.14	The Solid-Echo sequence	68
4.15	Pulse sequence for the Stimulated echo	68
4.16	Evolution of the magnetization	69
5.1	An example of the diffusion measurements	72
5.2	^{19}F Diffusion measurements in $\text{Ba}_{0.999}\text{La}_{0.001}\text{F}_{2.001}$	73
5.3	^{19}F Diffusion measurements in $\text{Ba}_{0.99}\text{La}_{0.01}\text{F}_{2.01}$	74
5.4	^{19}F Diffusion measurements in $\text{Ba}_{0.97}\text{La}_{0.03}\text{F}_{2.03}$	74
5.5	^{19}F Diffusion measurements for all samples	75
5.6	Correlation times from diffusion data for all samples	76
5.7	^{19}F -Lineshape measurements of pure BaF_2	77
5.8	^{19}F -Lineshape measurements of $\text{Ba}_{0.9995}\text{La}_{0.0005}\text{F}_{2.0005}$	78
5.9	^{19}F -Lineshape measurements of $\text{Ba}_{0.9995}\text{La}_{0.0005}\text{F}_{2.0005}$	78
5.10	^{19}F -Lineshape measurements of $\text{Ba}_{0.999}\text{La}_{0.001}\text{F}_{2.001}$	79
5.11	^{19}F -Lineshape measurements of $\text{Ba}_{0.999}\text{La}_{0.001}\text{F}_{2.001}$	79
5.12	^{19}F -Lineshape measurements of $\text{Ba}_{0.99}\text{La}_{0.01}\text{F}_{2.01}$	80
5.13	^{19}F -Lineshape measurements of $\text{Ba}_{0.99}\text{La}_{0.01}\text{F}_{2.01}$	80
5.14	^{19}F -Lineshape measurements of $\text{Ba}_{0.97}\text{La}_{0.03}\text{F}_{2.03}$	81
5.15	^{19}F -Lineshape measurements of $\text{Ba}_{0.97}\text{La}_{0.03}\text{F}_{2.03}$	81
5.16	^{19}F -Lineshape measurements of $\text{Ba}_{0.9}\text{La}_{0.1}\text{F}_{2.1}$	82
5.17	^{19}F -Lineshape measurements of $\text{Ba}_{0.9}\text{La}_{0.1}\text{F}_{2.1}$	82
5.18	^{19}F -Static Lineshape measurements of BaF_2	83
5.19	^{19}F -Static Lineshape measurements of $\text{Ba}_{0.9}\text{La}_{0.1}\text{F}_{2.1}$	83
5.20	^{19}F -MAS spectra of $\text{Ba}_{0.9}\text{La}_{0.1}\text{F}_{2.1}$ -powder sample	84
5.21	^{19}F -MAS spectrum of $\text{Ba}_{0.9}\text{La}_{0.1}\text{F}_{2.1}$ -powder sample	85
5.22	Lineshape model for BaF_2 -system	87
5.23	Lineshape analysis of BaF_2	89
5.24	Lineshape analysis of BaF_2	90
5.25	^{19}F Correlation times from lineshapes data for all samples	90
5.26	^{19}F -relaxation measurements in pure BaF_2	92
5.27	^{19}F -relaxation measurements in pure $\text{Ba}_{0.9995}\text{La}_{0.0005}\text{F}_{2.0005}$	92
5.28	^{19}F -relaxation measurements in pure $\text{Ba}_{0.999}\text{La}_{0.001}\text{F}_{2.001}$	93
5.29	^{19}F -relaxation measurements in pure $\text{Ba}_{0.99}\text{La}_{0.01}\text{F}_{2.01}$	93
5.30	^{19}F -relaxation measurements in pure $\text{Ba}_{0.97}\text{La}_{0.03}\text{F}_{2.03}$	94
5.31	^{19}F -relaxation measurements in pure $\text{Ba}_{0.9}\text{La}_{0.1}\text{F}_{2.1}$	94
5.32	Relaxation rates according to BPP-model	95

LIST OF FIGURES

5.33	Relaxation measurements plus theoretical analysis, 350K . .	96
5.34	Relaxation measurements plus theoretical analysis, 500K . .	96
5.35	Relaxation measurements plus theoretical analysis, 650K . .	96
5.36	Relaxation measurements plus theoretical analysis, 700K . .	96
5.37	Relaxation measurements plus theoretical analysis, 950K . .	97
5.38	Relaxation measurements plus theoretical analysis, 1000K .	97
5.39	Correlation times calculated with BPP-model	98
5.40	Non-exponential correlation function	99
5.41	Relaxation measurements plus theoretical analysis at 350K .	103
5.42	Relaxation measurements plus theoretical analysis at 400K .	103
5.43	Relaxation measurements plus theoretical analysis, 700K . .	103
5.44	Relaxation measurements plus theoretical analysis, 900K . .	103
5.45	Correlation times calculated for the F_1 subsystem.	104
5.46	Correlation times calculated for the F_2 subsystem.	105
5.47	All correlation times for BaF_2	107
5.48	All correlation times for BaF_2	107
5.49	All correlation times for BaF_2	108
5.50	All correlation times for BaF_2	108
5.51	All correlation times for BaF_2	109
5.52	All correlation times for BaF_2	109

Acknowledgements

I would like to express my gratitude to the many people who helped me make this work possible:

Franz Fujara, the most busy Professor I have ever met in my life. He has made my graduate school experience interesting by inviting me to work in his group. He was always very helpful.

Alexei Privalov has contributed much to experiments and pointing out a much easier way to do some matters.

Oliver Lips has always given me good advice. I have enjoyed many refreshing discussions about various aspects of our project, quantum mechanics, German grammar and issues concerning everyday life.

Danuta Kruk has contributed to the theoretical side of this work, always coming up with new ideas.

Marco Scheuermann has done a lot! I have enjoyed many refreshing discussions about science, L^AT_EX, and life.

Daniel Schäfer did the lineshape measurements and was always ready to help.

Harald Plößer was caring about our lab and it was always a great pleasure to work with him on technical aspects of the lab work.

Klaus Weber and the whole team of the electronics workshop were repairing everything that went "kaputt".

Prof. Dr. Clare Grey and Dr. Sylvio Indris have helped me with the MAS NMR measurements.

Prof. Dr. hab. Alicja Ratuszna and mgr Jerzy Kubacki have helped me with the XPS measurements.

Dr. Nikolay Kardilov have measured neutron tomography data.

Dr. Detlef Klimm have helped me understand problems concerning crystal growth.

Robert Mueller helped me by reading and correcting these "few" pages. I really appreciated everything he has done to get me through all the problems. I am grateful for our friendship.

Markus Rosenstihl, my room mate, who has supported me a lot in the

last year.

Achim Gädke was always ready to solve any computer problem and has corrected part of this thesis with me.

My parents who gave me a chance to "...contribute a verse"

Elzbieta Manjurka has helped me solving some problems with pictures.

Our secretary, Natasha Kalugina, who has done some of the "scanning work".

With Ingrid and Gerhard Ihnken, Arkadiusz Manjurka, my brother Marcin I have enjoyed many refreshing discussions about life.

Stephen Boyd helped me by reading and correcting this work.

And finally my best friend Arsenik, "he" deserves the most credit for helping me deal with the stress, giving lots of useful advice, reading and correcting this work and being the best teacher I have ever had.

Curriculum Vitae

Patryk Gumann
Barkhausstraße 45
64289 Darmstadt
Germany

1979/09/27	born in Skarzysko-Kamienn, Poland
1986–1994	elementary school (Skarzysko-Kamienna)
1994–1998	high school II L.O. im. A. Mickiewicza (Skarzysko-Kamienna)
1998/06/03	high school graduation (matura)
1998–2001	study of Physics at University of Silesia, Katowice, Poland
2001–2002	study of Physics at University of Wroclaw, Wroclaw, Poland
2002/06/26	Master of Science with a specialization in solid state physics at University of Silesia in Katowice, Poland
01/2003–07/2007	research assistant at the Institute of Solid State Physics Darmstadt University of Technology, Germany

Hiermit erkläre ich an Eides statt, dass ich die vorliegende Dissertation selbstständig und nur mit den angegebenen Hilfsmitteln angefertigt habe.

Bisher habe ich noch keinen Promotionsversuch unternommen.

Darmstadt, den 15. Oktober 2007

(Patrik Gumann)